INFLUENCE OF SYNRIFT SALT ON RIFT-BASIN DEVELOPMENT: APPLICATION TO THE ORPHEUS BASIN, OFFSHORE EASTERN CANADA

by

MICHAEL A. DURCANIN

A thesis submitted to the

Graduate School-New Brunswick

Rutgers, The State University of New Jersey

in partial fulfillment of the requirements

for the degree of

Masters of Science

Graduate Program in Geological Sciences

written under the direction of

Dr. Roy Schlische

Dr. Martha Oliver Withjack

and approved by

____

____

____

New Brunswick, New Jersey

October, 2009

ABSTRACT OF THE THESIS

Influence of Synrift Salt on Rift-basin Development: Application to the Orpheus Basin, offshore Eastern Canada

By MICHAEL A. DURCANIN

Thesis Director:

Dr. Roy Schlische & Dr. Martha Withjack

I present a new interpretation of the tectonic evolution of Orpheus basin, a narrow Mesozoic rift basin on the passive margin of offshore eastern Canada. This work incorporates insights gained from a scaled experimental modeling study that simulates multiphase deformation on a basin with a synrift ductile unit, to show that the structural deformation observed within this basin cannot completely be attributed to salt-related buoyancy-driven processes. Seismic data show that the Orpheus and overlying Scotian basins experienced at least four stages of development: Triassic-Early Jurassic rifting, shortening during the rift/drift transition in the mid-Early Jurassic, regional uplift and erosion during the earliest Cretaceous, and a fourth event that had, at least locally on the North Step, a compressional component during the Oligocene.

The presence of the synrift Argo salt profoundly affected the style of deformation during both the formation of the basin, and the subsequent tectonic events. The synrift salt decoupled the cover deformation from basement deformation. Forced folds and salt ridges developed in the cover above the salt, whereas, faulting accommodated basement extension below the salt. During subsequent tectonic events, deformation was mainly

accommodated above the basement faults by: 1) reactivating preexisting extensional structures such as passive salt diapirs and salt ridges, and 2) further amplifying preexisting forced folds that formed during the rifting phase. The presence of multiple unconformities, disharmonic sets of synclines and salt-cored anticlines (which developed from preexisting extensional forced folds), vertical salt welds, and detached thrusts indicate that this basin underwent multiple episodes of shortening, uplift, and erosion after rifting ended in the Early Jurassic.

TABLE OF CONTENTS

ACKNOWLEDGEMENTS

My sincerest thanks and gratitude go to Martha Withjack and Roy Schlische for their advice and support. They believed in my ability even when I began to question it myself. Thanks to my third committee member, Don Monteverde.

A special thanks John Adamick from TGS/Nopec Geophysical Company, and Dr. Peter Hennings from ConocoPhillips, for generously providing the seismic datasets that I used to complete this work. Also, a special thanks to all at the Nova Scotia Offshore Petroleum Board for providing access to their Data Management Center, and the Canadian Department of Natural Resources for providing the reprocessed Laurentian Basin Survey. Without all of their generosity much of this thesis would still be an idea.

I would also like to thank my colleagues in the structure group and all of the graduate students and faculty at Rutgers for their support and guidance. Lastly, I would like to thank my family and friends for their unconditional love and support.

This thesis was funded in part by a grant from the Geological Society of America, and generous support from Husky Energy and Petrobras.

LIST OF ILLUSTRATIONS

SECTION 1 - INTRODUCTION

Hydrocarbon exploration has revealed the presence of inverted basins and their associated structures in a variety of tectonic settings. Basin inversion occurs when basin-controlling extensional faults reverse their movement during subsequent compressional tectonics (e.g., Williams et al., 1989). Although a number of factors control deformation in such basins, the final structural style of inverted basins is strongly influenced by: 1) the composition of the synextensional basin infill, 2) the basement fault-zone geometry at the end of the extensional phase, and 3) the presence of preexisting structures within the sedimentary cover above the basement fault zone (Brun and Nalpas, 1996; Withjack and Callaway, 2000; Panien et al., 2005; Baum, 2006; Roca et al., 2006). The resulting styles of deformation fall into two general categories related to the linkage between the basement and cover.

In the first category, no ductile layer separates the basement from the sedimentary cover. In this “hard-linked” scenario, basement faults propagate directly into the sedimentary cover. In the second category, consider that a very ductile layer (e.g., salt) separates the basement from the sedimentary cover. In this “soft-linked” scenario, the ductile layer decouples basement deformation from cover deformation (e.g., Jackson et al., 1994; Stewart et al., 1996a; Withjack and Callaway, 2000; Richardson et al., 2005; Koyi and Sans, 2006). The second scenario is more complex because the thickness and extent of the ductile layer can change through time. Also, in some cases, basement involvement is commonly hidden by detached deformation (e.g., Stewart et al., 1996a; Richardson et al., 2005). Many basins of latter category exist in the North Sea (e.g., Coward and Steward, 1995; Stewart et al., 1996b), offshore Brazil (e.g., Lowell, 1995), offshore Portugal (Alves et al., 2003; Roca et al., 2006), and offshore eastern Canada (section three of this study; Sinclair, 1995). Because the role of salt in the evolution of a fault system changes through time, an understanding of the spatial and temporal relationship between structures above and below the salt layer is necessary to interpret these complex tectonic systems. Therefore, this thesis examines how: 1) basement-involved structures influence detached structures associated with a highly ductile layer during the initial rifting phase, and 2) how the presence of these detached structures influence structural geometries during subsequent phases of deformation (i.e., inversion).

The thesis has two main areas of investigation. Section 2 presents the results of an experimental modeling study. The study focuses on how deposition of a thick ductile layer (i.e., putty) affects patterns of deformation in the cover above the ductile layer both during rifting and subsequent basin inversion. In the models, putty structures that formed during the extensional phase are preferentially reactivated during shortening because they are mechanically weak (Hudec and Jackson, 2007). They accommodate much of the initial shortening by producing folds and thrust faults in the overlying cover. Putty flow during shortening, amplifies preexisting structures (e.g., putty columns and ridges) and also forms new putty structures such as pillows (a precursor to a putty-cored anticline), and detached normal and reverse faults.

Section 3 of this thesis provides additional information about the development of the passive margin of eastern North America by documenting the tectonic evolution of the Orpheus rift basin and the overlying northern Scotian basin of offshore eastern Canada. Seismic analysis provides evidence of multiple phases of deformation from the early Mesozoic to the early Cenozoic. Restorations indicate two general phases: a rifting phase related to the formation of the Orpheus basin during the Middle Triassic to Early Jurassic, and a “passive margin” phase related to the formation of the Scotian basin beginning with the onset of seafloor spreading during the late Early Jurassic to early Middle Jurassic. This research suggests that the postrift development of the Scotian basin was not “passive” as thought by most previous workers (e.g., MacLean and Wade, 1992).

The fourth and final section of this thesis compares the insights gained from the experimental modeling with seismic interpretation from the Scotian shelf. The modeling results compare well with the structural geometries present within the Orpheus basin and overlying Scotian basin. As in the models, deformation above the salt layer was decoupled from deformation below the salt layer during both the extensional and the shortening phases. During shortening, deformation was mainly accommodated above the basement fault zone by reactivating preexisting extensional structures such as passive salt diapirs and salt ridges. The presence of vertical welds, salt-cored anticlines and detached thrusts indicate that this basin underwent at least one episode of shortening after rifting ended.

SECTION 2 - Experimental Modeling of Salt Tectonics During Rifting and Inversion

2.1. INTRODUCTION

The use of physical models to simulate basement-involved extension and inversion (e.g., Cloos, 1968; McClay and White, 1995; Eisenstadt and Withjack, 1995; Mart and Dauteuil, 2000; Panien et al., 2005), and salt tectonics (e.g., Vendeville and Jackson, 1992a; Vendeville and Jackson, 1992b; Koyi et al., 1993; Jackson and Vendeville, 1994; Vendeville and Nielsen, 1995; Schultz-Ela and Jackson, 1996) have been the focus of many studies over the last 50 years. These studies provide insight into how geologic structures develop through time.

Previous workers have examined the effects of multiple phases of deformation, for example, extension followed by subsequent shortening, without a ductile layer (e.g., Buchanan and McClay, 1991; Mitra and Islam, 1994; Eisenstadt and Withjack, 1995; Baum, 2006). Few studies (e.g., Gartrell et al., 2005; Del Ventisette et al., 2006), however, investigate how the presence of a ductile layer (e.g., salt) within the synrift sequence affects the style of deformation during extension and subsequent basin inversion. Also, many workers in the field of salt tectonics have examined the role of basement-involved extension on the initiation and growth of salt structures (e.g., Vendeville and Jackson, 1992a; Vendeville and Jackson, 1992b; Koyi et al., 1993; Jackson and Vendeville, 1994) and the subsequent deformation patterns that develop within the sedimentary cover (Withjack and Callaway, 2000). Again, few studies (Vendeville and Nilsen, 1995; Del Ventisette et al., 2005; Roca et al., 2006; Dooley et al., 2009), have addressed how preexisting salt structures created during basement-involved extension influence deformation patterns during subsequent shortening.

Because the role of salt in the evolution of a fault system changes through time, an understanding of the spatial and temporal relationship between structures above and below a salt layer is necessary to interpret these complex structural styles. This work provides additional insight into how the deposition of a salt within a basin affects deformation during extension and subsequent basin inversion. Specifically, this section explores the following questions using scaled experimental modeling:

(1) How does salt move during synrift deformation?

(2) How does the overlying sedimentary cover respond to this movement?

(3) How do the structures created during rifting influence deformation patterns during inversion?

(4) How do the results of this study compare with those of previously published studies?

2.2. EXPERIMENTAL PROCEDURES

Apparatus

The modeling apparatus has three fixed walls, a movable wall, and two overlapping basal metal plates (one fixed, the other attached to the movable wall) (Fig. 2.1a). A basal discontinuity, created at the edge of the fixed plate, forms a preexisting zone of weakness at the base of the model. For all models, a single layer of wet clay, 8-cm thick, initially covers the two overlapping metal plates (Fig 2.1a, b). During the experiments, an electric motor pulls the moving lower plate outward at a constant velocity (3 cm hr^{-1}).

Modeling Medium

Although both dry sand and wet clay are suitable modeling materials to simulate natural deformation, the choice of modeling material affects the style and distribution of deformation in the models (Eisenstadt and Sims, 2005; Withjack et al., 2007). Most modeling studies simulating salt tectonics use dry sand to represent the brittle cover above salt (e.g., Vendeville and Jackson, 1992a; Jackson and Vendeville, 1994; Vendeville et al., 1995; Withjack and Callaway, 2000; Del Ventisette et al., 2005, 2006; Roca et al., 2006). I use wet clay rather than dry sand as the modeling material to better study the development of faults and folds because: (1) it is difficult to study the development and linkage of faults in sand models because faults propagate very quickly, (2) major faults accommodate the majority of the deformation in sand models, whereas wet clay distributes deformation on major and many minor faults, and (3) the low cohesion of sand inhibits significant folding (e.g., relay ramps, fault-displacement folding, and fault-propagation folding), as faulting accommodates the majority of strain (Eisenstadt and Withjack, 1995; Eisenstadt and Sims, 2005; Withjack and Schlische, 2006; Withjack et al., 2007). To achieve dynamic similarity when simulating the ductile behavior of salt (viscosity ~10^{16} – 10^{20} Pa s), a viscous silicone polymer whose effective viscosity is about 10^3 Pa s is used (see Appendix 1 for a discussion on scaling and Appendix 2 for properties of the silicone polymer).

Model Design

The experiments have three phases of deformation (Fig. 2.2a). During the initial extensional phase, the mobile plate moves outward in a direction oriented 90° from the edge of the overlapping plates at a rate of 3 cm hr^{-1} for 5 cm, forming an asymmetric basin in the clay layer above the displacement discontinuity. During the second phase of deformation, the mobile plate again moves outward in a direction oriented 90° from the edge of the overlapping plates at a rate of 3 cm hr^{-1} for an additional 5 cm (Fig. 2.2b). The third phase of deformation simulates rift-basin inversion. During this phase, the mobile plate moves inward in a direction oriented 90° from the edge of the overlapping plate at a rate of 10 cm hr^{-1} for a total displacement of 10 cm (Fig. 2.2c). The increased rate of displacement during shortening is related more towards convenience rather than to simulate a natural displacement rates. The rate of displacement during shortening is still within the same order of magnitude as the displacement rate during extension, and will not have any adverse effects on the development of structures. All phases of deformation are identical in all models with respect to the displacement rate, magnitude, and direction.

Model 1 – Inversion Following Orthogonal Extension (standard; no salt analog)- Fig. 2.2b (left)

In the Model 1, wet clay fills the basin created during the first phase (Figs. 2.2a, 2.3a), simulating synrift deposition of brittle sedimentary rocks. The clay is then covered with an additional 1 cm of wet clay simulating sediment aggradation during a period of tectonic quiescence before a renewed pulse of extension (Fig. 2.4a).

Models 2A-B – Inversion Following Orthogonal Extension (with salt analog)- Fig. 2.2b,c (right)

In Models 2A and 2B, silicone polymer fills the basin created during the first phase, simulating deposition of synrift salt (Figs. 2.2b-c, 2.3b-c). In both models an additional 1 cm of wet clay covers the entire model surface, simulating aggradation during a period of tectonic quiescence before a renewed pulse of extension (Fig. 2.4b- c).

In Model 2A, the aggradation layer is added in two increments. Because putty diapirs formed after the first increment, deposition of the second increment was not uniform (i.e., a thinner cover over the rising diapirs). In Model 2B, the 1-cm aggradation layer was added uniformly, suppressing the early formation of diapirs.

2.3. MAP-VIEW DEFORMATION RESULTS

Phase 1 – All Models

All models have the same first phase of extension. During this phase, a major fault zone, parallel to the displacement discontinuity, bounds the basin on the fixed-plate side, whereas a wider series of normal faults bounds the basin on the moving-plate side (Fig. 2.3a-c). These secondary faults also strike parallel to the displacement discontinuity, and dip both toward and away from the main fault zone. The displacement on the main border-fault zone (BFZ) increases throughout the first phase of deformation, and the fault remains anchored to the edge of the fixed plate. The secondary zone of normal faults (SFZ) in the hanging-wall of the main BFZ, however, moves with the mobile plate. As such, deformation within this zone becomes older farther from the edge of the fixed plate. At the end of phase 1, the central basin between the main BFZ and the secondary fault zone is relatively flat and unfaulted (Fig. 2.3a-c).

Model 1 (no salt analog) - Phase 2 & 3

Phase 2 – Deposition/Extension

During phase 2, the mobile plate continues to move outward, in a direction orthogonal to the edge of the fixed plate. In the early stages, both the main BFZ and the SFZ propagate upward, producing fault-propagation folds in the overburden (Fig. 2.5a). With increasing displacement, both fault zones cut the clay surface (Figs. 2.5c-e). A wide asymmetric basin forms between the two zones. The strike of the BFZ parallels the edge of the fixed plate, as does the secondary fault zone (Fig. 2.5a-e). At the end of phase 2, the overall width of the deformed zone increases on both the main BFZ and the secondary fault zone (Fig. 2.6). Because the secondary zone of normal faults moves with the mobile plate, deformation within this zone becomes older farther from the edge of the fixed plate.

Phase 3 – Inversion

During phase 3, the mobile plate moves inward, in a direction orthogonal to the edge of the fixed plate (Fig. 2.7a-b). Many of the pre-existing normal faults are reactivated with reverse displacement. After 5 cm of displacement, many faults still have normal separation (Fig. 2.7c). As shortening progresses, the central basin rises, and new reverse faults and folds develop (Fig. 2.7d-e). At the end of phase 3, topographic highs and lows accentuate the central basin. Some of the normal faults created during the second phase of extension are completely inverted, whereas others maintain normal separation (Fig. 2.8). The strike of both the reactivated normal faults and the newly formed thrust faults trend parallel to the edge of the fixed plate. The overall pattern of deformation in this experiment resembles that in experiments by Eisenstadt and Withjack (1995) and Eisenstadt and Sims (2005).

Inversion with salt analog - Phases 2 & 3

For ease of description, faults that formed during the first phase are defined as subputty faults. Both the main BFZ and the SFZ are subputty fault zones. Faults that form within the cover above the putty, defined as supraputty faults, may or may not link with the subputty faults.

Model 2A – Non-uniform Sedimentation

Phase 2 – Deposition/Extension

During phase 2, the mobile plate continues to move outward, in a direction orthogonal to the edge of the fixed plate (Fig. 2.9a-e). In the very early stages of the second phase, putty diapirs actively pierce the thin clay cover, and wide fault-propagation folds form above both pre-existing fault zones (Fig. 2.9a). Putty begins to extrude onto the clay surface from the putty diapirs, denoting the change from active to passive diapirism (in the sense of Vendeville and Jackson, 1992a,b) (Fig. 2.9b).

With increasing displacement, the major subputty faults continue to develop. Two zones accommodate extension in the cover above the putty: 1) a fault zone linked to the main BFZ, and 2) a detached fault zone above the SFZ, but decoupled from the SFZ (Figs. 2.10, 2.11c). New putty extrusions develop around zones of detached normal faulting in the cover, marking the onset of reactive diapirism (Fig. 2.11c,d; in the sense of Vendeville and Jackson, 1992a,b). Large detached normal faults above the SFZ accommodate the majority of extension in the cover. Some detached normal faults, although covered by allochthonous putty sheets, continue to accumulate displacement and propagate laterally. In some cases, these detached faults nucleate at the edges of the putty conduits and propagate outward (Fig. 2.10). Broad, shallow depressions form in areas subject to putty withdrawal.

Phase 3 - Inversion

During phase 3, the mobile plate moves inward, in a direction orthogonal to the edge of the fixed plate (Fig. 2.11a-e). In the early stages of phase 3, existing diapirs, rejuvenated by shortening, continue to extrude putty onto the clay surface. With increasing displacement, the shallow depressions formed during phase 2 evolve into asymmetric synclines in areas of increased putty withdrawal (Figs. 2.11b-c, 2.12a). Reactivation of the main BFZ with reverse movement, coupled with reactive putty diapirism, accentuates topographic highs and lows in the cover. Some openings where putty is exposed along faults in the cover begin to close (Fig. 2.12b), reducing the available conduits that link the source layer to the surface (Fig. 2.11c-d). As shortening continues, small-scale asymmetric synclines and anticlines that formed during phase 2 increase in size both laterally and vertically. Increased shortening amplifies preexisting folds both near and far from the putty extrusions, and at the end of phase 3, cover topography develops into deep depressions and localized highs (Fig. 2.12, 2.13). Also at the end of phase 3, some faults in the cover show reverse separation, whereas other faults show normal separation. The main BFZ, although reactivated with reverse movement, still maintains normal separation at the end of the third phase (Fig. 2.13).

Model 2B – Uniform Sedimentation

Phase 2 – Deposition/Extension

During phase 2, the mobile plate continues to move outward, in a direction orthogonal to the edge of the fixed plate (Fig. 2.14a-e). In the early stages of phase 2, large fault-propagation folds form within the cover above both the BFZ and SFZ (Fig. 2.14a-b). In the early stages of the phase 2, two zones accommodate extension in the cover: 1) a fault zone above and linked to the main BFZ and 2) a zone of detached normal faults near the SFZ (Fig. 2.14c-d). Putty extrusions develop around zones of detached normal faulting above the central basin in the cover, marking the initiation of reactive diapirism. With increasing displacement of the moving plate, extension is accommodated in the cover on several large faults above the SFZ, and by the further opening of existing putty conduits within the central basin. By the end of phase 2, cover deformation is localized in three zones: 1) above the main BFZ, 2) within the central basin in open putty conduits, and 3) above the SFZ below the putty layer (Fig. 2.15). As in the previous model, the strike of the cover faults is generally parallel to the edge of the fixed plate.

Phase 3 – Inversion

During phase 3, the mobile plate moves inward, in a direction orthogonal to the edge of the fixed plate (Fig. 2.16a-e). Putty extrusions rejuvenate during the early stages of shortening (Fig. 2.16b-e). As displacement of the moving plate increases, the shallow depressions formed during phase 2, begin to evolve into asymmetric synclines where putty is evacuating and anticlines where putty fills the cores of growing folds (Fig 2.16b-c). Small-scale asymmetric folds above regions of putty flow increase in size both laterally and vertically. Increased shortening amplifies preexisting folds and creates new folds both near and far from the putty extrusions (Figs. 2.16c-e, 2.17a). Normal faults, which form above amplified putty-cored folds, are likely associated with bending of the supraputty cover (Fig. 2.17a-c). The width of some putty conduits decreases, whereas the width of others remains unchanged. The continued closure of some putty conduits, especially those along faults, isolates the allochthonous putty from the source layer. At the end of phase 3, cover topography develops into deep depressions and localized highs that are well above regional level (Fig. 2.18). Some detached faults above the SFZ now have reverse separation, whereas other faults, such as those above putty-cored anticlines, still maintain normal separation. The main BFZ, although reactivated with reverse movement, still maintains normal separation. Also, the once linked zone of putty diapirs becomes a detached thrust zone that is decoupled from the basement (Fig. 2.18b).

2.4. DISCUSSION

Summary of Map-View Deformation

Extension - Figure 2.19 top

The presence of synrift putty (simulating salt) significantly influences rift-basin development by decoupling deep and shallow deformation during extension. Without synrift putty (i.e., model 1), most deep-seated normal faults propagate upward to the surface. These normal faults strike parallel to the rift-basin axis and accommodate most of the extension (Fig. 2.19a). With synrift putty (i.e., models 2A & 2B), deformation patterns vary substantially with depth (Fig. 2.20a). Fault-propagation folds develop above some deep-seated faults (i.e. the main BFZ in all models). Subputty faults eventually propagate up to the surface where putty is thin or not present. The subputty faults that form the SFZ, however, do not propagate upward to the surface. Instead, they terminate within the overlying putty layer. Above the putty, detached normal faults (e.g., model 2A; Fig. 2.19b) and widening putty diapirs (e.g., model 2B; Fig. 2.19c) accommodate the majority of extension at shallow levels. Coeval, deep-seated and detached normal faults, although decoupled by the layer of silicone polymer, have identical strikes that reflect the extension direction.

The processes leading to diapir formation affect deformation patterns throughout the remainder of phase 2 and phase 3. Commonly, diapirs develop where the putty layer is thickest (i.e., in the deepest part of the rift basin) and can form allochthonous sheets if depositional rates are low (Fig. 2.20). If putty structures appear early (e.g., model 2A; Fig. 2.9a), and form because of uneven sedimentation above the putty layer, detached faults above the SFZ are more likely to accommodate most of the extension in the cover. These early diapirs tend to keep their cylindrical shape throughout the remainder of the experiment, unless they link with either a putty ridge or a laterally propagating normal fault. If putty structures form late (e.g., model 2B and center of model 2A; Figs. 2.9d, 2.14a-c), they are likely reactive structures (in the sense of Vendeville and Jackson, 1992a,b), and their locations depend on: 1) the thickness of the putty layer, and 2) the amount of extensional thinning of the cover above the putty layer. Initially, the reactive diapirs emerge at the surface in the hanging walls of detached faults. As these diapirs link, their width increases causing the putty extrusions (or salt walls) to grow larger. When the salt wall becomes passive (i.e., breaks the surface and begins to flow outward) the segments of the clay cover between the extrusions extend almost entirely by widening the conduit itself. Because the putty conduits accommodate much of the extension, fewer faults form in the supraputty cover.

Inversion – Figure 2.19 bottom

The deformation patterns of inverted basins are strongly influenced by: 1) the composition of the basin infill (i.e. with or without a ductile layer), and 2) the presence and geometry of preexisting putty structures that formed during the extensional phase. Because these structures are weaker than other parts of a basin, the cover above and around these structures tends to deform much more than adjacent areas. Without synrift putty (i.e., Model 1), deep-seated normal faults undergo reverse displacement (Fig. 2.19a). The basin center rises and new reverse faults and folds develop. With synrift putty (i.e. models 2A & 2B), subputty faults, visible through open putty conduits, and detached normal faults undergo reverse displacement. Detached folds and reverse faults form in the central basins in both putty models (Fig. 2.20b).

In both models, putty flow amplifies preexisting structures, forms new structures such as putty-cored anticlines and welds where putty conduits close completely (Fig. 2.20b). Anticlines can form above previously undeformed putty (i.e., center of model 2A (Fig. 2.10); right side of Model 2B (Fig. 2.18)), but are more common above preexisting putty structures. In cases where diapir feeder conduits are more cylindrical (i.e., model 2A (Figs. 2.8, 2.10); middle of model 2B (Figs. 2.14, 2.18)), amplification of putty-cored anticlines is accompanied by additional slip on preexisting normal faults at the crests of the diapirs. Structures with this geometry also tend to remain open, and continue to feed allochthonous putty sheets until the source layer is exhausted and/or blocked by subputty deformation. In cases where diapirs are located in the hanging walls of detached normal faults, or are linked (i.e., model 2B; center of model 2A), fold amplification happens only after the closure of conduits that feed the allochthonous sheets. During closure of the putty walls, the intruding viscous material can be squeezed upward and extruded onto the surface. If open diapirs close completely, but are still subjected to shortening, a detached thrust zone can form between the previously open walls of the putty diapir. Again, most of the basement shortening is accommodated in the cover by reactivating preexisting putty structures and forming detached thrusts in areas where putty is thin or absent (Fig. 2.20b).

Comparisons to Previous Work

Previously published studies (e.g., Vendeville and Nilsen, 1995; Del Ventisette et al., 2005; Roca et al., 2006; Dooley et al., 2009) have involved a series of multi-layer sand and silicone polymer models to understand the effects of shortening on preexisting salt structures. The results of these models compare well with my results. The boundary conditions (e.g., multi-phase extension and shortening) in models by Del Ventisette et al. (2005) and Roca et al. (2006), however, are more similar with those of this study. Del Ventisette et al. (2005, 2006) used similar initial boundary conditions as those in this study, but varied the shortening direction from purely dip-slip movement (perpendicular to the displacement discontinuity) to purely strike-slip movement (parallel to the displacement discontinuity). They subjected their models to the same episodes of deformation: an initial phase of extension that formed a basin, deposition of a salt analog within the basin, and a second phase of extension preceding a final phase of shortening. A major difference between their models and this study is the addition of deposition both during the second extensional phase and the inversion phase, which likely affected deformational styles and geometries. The multi-layer dry sand models of Roca et al. (2006), however, compare very well with this study. Their models had only two layers, a lower layer of silicone polymer and an upper layer of dry sand, and did not incorporate syntectonic sedimentation.

During the modeling in both studies (i.e., Del Ventisette et al., 2005, 2006; Roca et al., 2006), most of the deformation during inversion was accommodated along preexisting putty structures that had formed during the first phase of extension. During different tectonic phases, the putty migrated from areas with higher loading to areas where the overburden was thinned. Similar to the putty models in this study, areas subject to putty withdrawal and accumulation during the extensional phase were further accentuated during the shortening phase, forming deep withdrawal basins that became primary welds, or localized highs created as putty migrated into the cores of growing anticlines.

Again, direct comparison of the results of these published models with these models are difficult because of the significant differences in modeling parameters, procedures, and more importantly, the focus on cross-section analysis versus map-view analysis. Nevertheless, the published deformation patterns are similar to deformation patterns in my models when the boundary conditions are similar. To summarize, all of these previous works highlight how the presence of salt within a basin greatly affects deformation patterns in the cover above the salt layer during regional tectonic events.

2.5. CONCLUSIONS

- Scaled experimental models show that the presence of synrift salt strongly affects deformation patterns during rifting and subsequent basin inversion. During rifting, two fault zones develop: 1) the main border-fault zone, and 2) secondary hanging-wall faults. In models without putty, all faults are basement-involved. In models with putty, cover deformation is decoupled from basement deformation in areas with putty, but is linked to basement deformation in areas without putty. Putty diapirs form during extension, and putty withdrawal produces broad, shallow depressions.

- The formation of diapirs is related to the uniformity of cover deposition and amount of extension. When aggradation is slow and not uniform, diapir formation is buoyancy driven. In these cases, diapirs appear early and remain at the surface. These structures form as the thin overburden above the rising diapirs is lifted and shouldered aside as the diapir forcibly breaks through by active diapirism. When aggradation is rapid and uniform, diapir formation is driven by regional extension. In these cases, diapirs form late, and are likely reactive diapirs. During this process, the ductile layer rises by filling in the space created by the extending cover and/or separation of fault blocks by reactive diapirism. In either case, the active and reactive diapirs quickly become passive diapirs when they reach the surface and extrude putty sheets. When diapirs form early, detached faults are more likely to accommodate most of the basement extension. When diapirs form late, cover extension is accommodated, first by linking the emerged diapirs, and then by widening the conduit that separates the two cover segments.
- The overall expression of shortening at the surface depends on the locations and geometries of preexisting putty structures because these structures are weaker than other parts of a basin. As such, the cover above and around these structures tends to deform much more than adjacent areas of thicker overburden. During inversion, shortening amplifies putty-cored anticlines and synclines into localized highs and deep asymmetric depressions, respectively. Some detached normal faults in the cover reactivate as reverse faults, whereas other faults (e.g., those near putty conduits) continue to have normal slip during shortening. Some putty

conduits rejuvenated by shortening continue to extrude putty, whereas other putty conduits close forming vertical welds or thrusts.

SECTION 3 – The Orpheus Rift Basin and Overlying Post-rift Scotian Basin, Offshore Maritime Canada

3.1. INTRODUCTION

Withjack et al. (1998) have shown that the tectonic evolution of the passive margin of eastern North America (Fig. 3.1) consists of a series of events involving rifting, igneous activity, and post-rift deformation. In this thesis, I provide additional information about the development of the passive margin of eastern North America by documenting the tectonic evolution of the Orpheus rift basin and the overlying northern Scotian basin of offshore Maritime Canada. A consensus regarding the tectonic evolution of these basins is lacking among previous workers. For example, some workers (e.g., Wade and MacLean, 1990; MacLean and Wade, 1992; MacLean and Wade, 1993) suggest that postrift salt tectonics controlled patterns of deformation. Alternatively, other workers (e.g., Pe-Piper and Piper, 2004; Weir-Murphy et al., 2004) suggest that postrift deformation in the Orpheus and Scotian basins resulted from periodic strike-slip reactivation of the main basin-bounding fault system. This ongoing debate continues because: (1) very few seismic reflection surveys existed over the study area until recently, and (2) the presence of thick salt and igneous intrusions (as documented by this study) obscures the deeper deformation within the basin.

This work presents a tectonostratigraphic analysis of the Orpheus basin and overlying Scotian basin, using newly acquired 2-D seismic surveys. Specifically, this study focuses on the northern margin of the Orpheus and Scotian basin where the data quality is best, and addresses the following questions:

(1) Do structural geometries on the northern margin of the Orpheus and Scotian basins indicate that more than one episode of postrift deformation occurred? If so, when did they occur?

(2) How does the presence of salt affect deformation patterns during and after rifting?

(3) How do the results of this study compare with previously published studies?

(4) Does the Orpheus rift basin share a similar tectonic history with the neighboring Fundy basin? If so, does the Mesozoic-Cenozoic evolution of the Orpheus and Scotian basins help constrain the timing of deformation in the neighboring Fundy basin?

3.2. BACKGROUND

Regional Geologic Setting

The Fundy rift basin of New Brunswick and Nova Scotia, Canada, and the Orpheus rift basin of Nova Scotia and Newfoundland, Canada, formed during the breakup of Pangea beginning in Middle to Late Triassic time and continuing into Early Jurassic time (Figs. 3.1-3) (e.g., Tankard and Welsink, 1989; MacLean and Wade, 1992; Withjack et al., 1995). A well-defined, E- to ENE- trending zone, known as the

Cobequid-Chedabucto fault system, marks the northern faulted margins of both the Fundy and Orpheus basins (Figs. 3.2, 3.3; Tankard and Welsink, 1989; Wade and MacLean, 1990). The zone likely is a Paleozoic compressional structure that was reactivated during rifting (Olsen and Schlische, 1990; Withjack et al., 1995; Wade et al., 1996). During Mesozoic rifting, the Fundy basin filled with several kilometers of nonmarine sedimentary rocks and basalt flows (e.g., Olsen et al., 1989; Olsen and Schlische, 1990), whereas synrift deposits in the offshore Orpheus basin consist of thick evaporites interfingered with both clastic marine and non-marine sedimentary rocks (e.g., Wade and MacLean, 1990; MacLean and Wade, 1992; Pe-Piper et al., 1992). After rifting, thermal subsidence produced a widespread depression known as the Scotian basin, which is comprised of thick wedges of Middle Jurassic to Cenozoic clastic and carbonate sedimentary rocks.

Field and seismic data show that the Fundy basin underwent two separate episodes of deformation during the Mesozoic (e.g., Withjack et al., 1995; Baum, 2003; Baum et al., 2008; Withjack et al., 2009). During the Late Triassic to Early Jurassic the basin underwent NW-SE extension. During a subsequent phase of deformation after rifting, shortening affected all faulted margins of the Fundy basin (Fig. 3.2b-d). Because only Quaternary strata overlie the synrift beds in the Fundy basin, the timing of this shortening event is poorly constrained. Withjack et al. (1995) suggested that, because the E-striking Cobequid-Chedabucto fault system (CCFS) is the northern boundary of both the onshore Fundy basin and offshore Orpheus basin, it is likely that both basins have similar tectonic histories. Thus, understanding the timing of deformation in the Orpheus basin provides information about the timing of deformation in the Fundy rift basin.

Orpheus basin and Scotian basin

The Orpheus basin is an E-trending, narrow synrift basin underlying a wide postrift depression known as the Scotian basin (Figs. 3.3-5). As mentioned previously, the Cobequid-Chedabucto fault system (CCFS) forms the northern boundary of the basin (Tankard and Welsink, 1989; Wade and MacLean, 1990; MacLean and Wade, 1992). Regionally, the top of basement consists of a series of tilted fault blocks bounded by numerous E-striking faults that comprise the CCFS (Figs. 3.3, 3.4). The North Step, defined by MacLean and Wade (1992), is the main focus of this study and is located in the central segment of the Orpheus basin (Fig. 3.3, 3.4). The multiple E-striking, S-stepping, basement-involved faults that comprise the North Step are also part of the Cobequid-Chedabucto fault system (CCFS).

3.3. DATA AND INTERPRETATIONS

The database for this study includes over 12,500 km of public and proprietary 2D seismic-reflection profiles from offshore Nova Scotia, southern Newfoundland, and the French territory of St. Pierre and Miquelon (Fig. 3.4; see Appendix 3 and 4 for a table of seismic lines and detailed processing parameters). TGS/Nopec Geophysical Company, L.P. and ConocoPhillips acquired these datasets from 1998 to 2002 using airgun sources. The record sampling interval was 2 ms, and the processing sampling interval was 4 ms. Processing parameters included standard and predictive deconvolution, normal move-out stacking, migration and residual velocity analysis, and Kirchhoff pre-stack time migration. Also, the Geological Survey of Canada provided a recently reprocessed dataset, known as the Laurentian Basin Survey. Western Geophysical, Inc. shot the survey for the Geological Survey of Canada in 1984 and 1985. This dataset consists of

29 lines, representing 3,100 km of 2D multi-channel seismic data. Of the 11 exploratory wells drilled in both the Orpheus basin and overlying Scotian basin, five tie directly to the seismic datasets within the study area (Fig. 3.4) and will be discussed in detail later in this section.

Observations/Description of Data

Based on preliminary regional mapping of the entire dataset, four tectonostratigraphic packages (A-D), bounded by major angular unconformities, are identified within the study area (Figs. 3.4-7). The deepest visible package overlying basement and prerift strata, Package A, is further subdivided into three units (A_1-A_3). The shallowest and youngest unit, A_3, consists of moderate- to high-amplitude, parallel, continuous reflections that are tightly folded. Below unit A_3, unit A_2 overlies major basement faults. Although unit A_2 lacks coherent internal reflections, the top of A_2 is conformable with the folded strata above it (i.e., A_3), whereas the base of A_2 is relatively flat lying and offset by major basement faults in some instances (Fig. 3.6, 3.7). These basement-involved faults cut the deeper reflections below unit A_2 (i.e., A_1), but not the folded reflections in unit A_3. The decoupling of the shallow and deep deformation suggests that A_2 is a ductile unit. On the northern portion of seismic line 1124A-105, shallow reflections, unit A_3, converge near major basement faults (Fig. 3.6). A major angular unconformity bounds the top of Package A both on and south of the North Step.

Package B overlies the unconformity south of the North Step in the deeper parts of the Orpheus basin (Fig. 3.6). It consists of moderate-amplitude, subparallel reflections that dip toward the south. Package B represents a very thick (>1.5 seconds TWTT) succession of basin infill that thins significantly toward the North Step where it is truncated by a moderate-amplitude angular unconformity.

The seismic character of Package C varies depending on proximity to the North Step. South of the North Step, Package C overlies Package B and consists of moderate-amplitude, continuous, parallel reflections that dip to the south (Fig. 3.6). On the North Step, above the Cobequid-Chedabucto fault system, Package C overlies Package A, and consists of high-amplitude, widely spaced reflectors that dip in several directions (Figs. 3.6, 3.7). The top of Package C is truncated by a high-amplitude angular unconformity.

Package D unconformably overlies Package C throughout the study area. Package D is further subdivided into a lower unit (D_1) and an upper unit (D_2). Reflections in unit D_1 are generally moderate amplitude, closely spaced, continuous, subparallel, and gently folded. Unit D_2 is similar in character and geometry to D_1, but is truncated at the top by a prominent, flat-lying angular unconformity.

Interestingly, the geometries of the folded beds in Packages A, C, and D are disharmonic, most noticeable in the center part of the North Step (Fig. 3.6). Seismic reflections in unit A_3 of Package A are convex-upward, whereas the bounding unconformity at the top of unit A_3, and Packages C and D are convex-downward. This suggests that the deformation observed on seismic lines over the North Step is not related to a single episode, further indicating that additional tectonic events occurred after the deposition of Package A.

Igneous Intrusions

The seismic expression of igneous intrusions is characterized by very high-amplitude reflections that are typically subparallel to bedding (Hansen et al., 2004). Locally, intrusions can cut across bedding, and climb to a higher stratigraphic level. Generally, sills are saucer-shaped, but in many cases bifurcate or splay (Hansen et al., 2004). On the North Step, Package A contains very high amplitude reflections that are generally parallel to subparallel with the reflections above and below it (Figs. 3.6-8a). An angular unconformity at the base of Package C (top of Package A) truncates these reflections both on and south of the North Step. Although this high amplitude reflection is parallel with other reflections in Package A on seismic line 1124A-105 (Fig. 3.6), it is clear on the tie line, 98G10-52 (Fig. 3.7), that these reflections change stratigraphic levels. This suggests that these high amplitude reflections are likely igneous intrusions emplaced after deposition of strata in Package A, but before deposition of Package C.

South of the North Step, Package C also contains very high-amplitude reflections that both parallel and cut across reflections above and below it (Fig. 3.8b). Interestingly, the angular unconformity above Package C is folded above this high amplitude event, and reflections in Package D, unit D_1, thin over this topographic high. Although this reflection is present in Package C, the converging reflections in unit D_1 over this high suggest that a second igneous event occurred during the early deposition of Package D.

3.4. SEISMIC STRATIGRAPHY

Five industry wells that surround the study area are used to: 1) tie the interpreted seismic packages with regional lithostratigraphic units, and 2) provide information about the absolute ages of seismic horizons (Figs. 3.5, 3.8, 3.9). The absolute ages for seismic horizons are based on biostratigraphic data from well cuttings (see Appendix 5 for detailed lists of picks for each well). Well information, recorded in depth, is displayed onto the time-migrated seismic section (Fig. 3.5), using time-to-depth tables calculated from velocity surveys provided by the Nova Scotia Offshore Petroleum Board (http://ww1.cnsopbdmc.ca/) for each well (Appendix 6).

Although two exploratory wells used in this study (i.e., Hesper P-52/Sachem D-76) penetrate below Bathonian/Callovian aged strata, the structural complexity surrounding the immediate study area prevents correlation of seismic horizons to well markers older than late Bathonian (Fig. 3.5). In these instances, relative ages and lithologies are based on 1) regional stratigraphic information from other wells, and 2) the known expression of these units on seismic datasets surrounding the study area (e.g., Wade and MacLean, 1990; MacLean and Wade, 1993).

Package A – Middle Triassic (Anisian) to Early Jurassic (Sinemurian)

Without well control the absolute ages of Package A are unknown. However, the seismic characteristics of Package A indicate that it is equivalent to synrift material in the western Orpheus basin. Based on well data from the westernmost Orpheus basin, the synrift section consists of the clastic sedimentary rocks of the Eurydice Formation (unit A_1 & A_3), and underlies and interfingers with the Argo Formation (unit A_2) on the basin margins (Jansa and Wade, 1975). The Argo Formation consists primarily of thick evaporites, predominantly of coarsely crystalline halite interbedded with dolomitic shale and some anhydrite (Wade and MacLean, 1990; MacLean and Wade, 1992; Tanner and Brown, 2003). Within the Orpheus basin, the Argo Formation ranges from Carnian-Sinemurian, and represents multiple coeval terrestrial-to-marine transitions on the basin margins (Wade and MacLean, 1990), and is likely the unit that decouples unit A_3 from the faulted unit A_1 below (Fig. 3.10, 3.11). The Early Jurassic Breakup Unconformity, which formed due to thermal uplift at the onset of seafloor spreading, and/or shortening during basin inversion, bounds the top of Package A (Fig. 3.10, 3.11).

Widespread igneous activity, know as the Central Atlantic Magmatic Province, occurred during the latest Triassic/earliest Jurassic and is part of the synrift succession in many Mesozoic rift basins in eastern North America. Although not present in wells in the immediate study area, the presence of flows and intrusive sills and dikes exist both in industry wells west of the study area (e.g., Jansa and Pe-Piper, 1988) and onshore in the Fundy rift basin (e.g., Olsen et al., 1996; Olsen, 1999; Schlische et al, 2003). Because intrusions within Package A are truncated by the Breakup Unconformity, they were present before breakup occurred, which suggests they are older than late Early Jurassic (Fig 3.9-12).

Again, Package A appears to be part of the synrift sequences because it shares characteristics with the synrift sequences in wells west of the study area such as a ductile unit and igneous intrusions (e.g., sills and dikes). It is important to note that Package A does not resemble the typical geometry of a synrift sequence where reflections diverge and thicken towards major faults. Instead it resembles the synrift putty models in Section 2 where thickness variations are controlled by the locations of major salt structures as opposed to major basement faults.

Packages B and C – late-Early (Sinemurian/Pliensbachian) to latest Jurassic

Above both the synrift sedimentary sequences in the Orpheus basin and the Breakup Unconformity (BU), Packages B through D represent the succession of sedimentary rocks that were deposited both during and after the onset of sea-floor spreading in the postrift Scotian basin (Figs. 3.5, 3.9, 3.10). Regional stratigraphic information suggests that Package B comprises late Early (Sinemurian/Pliensbachian) to early Middle Jurassic strata that overly the BU (Wade and MacLean, 1990). It is restricted to the deeper parts of the Scotian basin, and is bounded at the top by a Middle Jurassic unconformity (JmU). The Mic Mac Formation, a very thick (>2.5 seconds TWTT), predominantly clastic post-rift sequence, comprises Package C, the remaining Jurassic strata in the Orpheus basin (Wade and MacLean, 1990; MacLean and Wade, 1992). The Mic Mac Formation exists predominantly in the three western wells (i.e., Hesper P-52/ Sachem D-76/ Dauntless D-35) within the study area. It lies between the JmU and the prominent angular base Cretaceous Avalon Unconformity (AU).

Package D – Cretaceous to Cenozoic

As previously mentioned, Package D is subdivided into two units, a lower unit D_1 and an upper unit D_2. The lower boundary of Package D is the base Cretaceous Avalon Unconformity. The top of the lower unit D_1 is a prominent high-amplitude seismic horizon. Well correlation indicates that this high-amplitude event is the boundary between Cretaceous strata below and Cenozoic strata above (Figs. 3.5, 3.9-11). The Cretaceous strata in unit D_1 are characterized by the seaward-thickening sequences of the Missisauga, Logan Canyon, Dawson Canyon and Wyandot formations (Wade and MacLean, 1990). In some areas, the AU is slightly folded above intrusive sills in Package C (Figs. 3.8b, 3.13). The presence of growth beds over this localized high suggests that igneous activity occurred shortly after the formation of the AU. Cenozoic strata, unit D_2, consist of the Banquereau Formation and are bounded at the base by the

Cretaceous/Tertiary unconformity and several prominent middle Cenozoic unconformities (Figs. 3.5, 3.10, 3.11; MacLean and Wade, 1992).

3.5. TECTONIC DEVELOPMENT OF THE ORPHEUS BASIN

Seismic data from the central part of the Orpheus basin and the overlying Scotian basin provide evidence of multiple phases of deformation from the early Mesozoic to the early Cenozoic. The development of this area has two general phases: a rifting phase related to the formation of the Orpheus basin during the Middle Triassic to Early Jurassic, and a "passive margin" phase related to the formation of the Scotian basin beginning with the onset of seafloor spreading during the late Early Jurassic to early Middle Jurassic (Fig. 3.5; Withjack et al., 1998). Figure 3.14 is a schematic restoration of the northern margin of the study area from early Middle Triassic to present.

3.5.1. Rifting Phase

Middle Triassic to earliest Early Jurassic Evolution (Fig. 3.14a-d)

The first episode of deformation from the Middle Triassic to Early Jurassic was extensional. Based on field data from the onshore Fundy basin, NW-SE extension (i.e. Schlische and Ackermann, 1995; Withjack et al., 2009) associated with rifting, reactivated E-striking Paleozoic compressional structures forming an oblique-slip fault zone with normal and left-lateral components of displacement (Fig. 3.14a; Tankard and Welsink, 1989; Olsen and Schlische, 1990; MacLean and Wade, 1992; Withjack et al., 1995; Withjack et al., 2009). In the Orpheus basin, synrift sedimentation included the deposition of both clastic sedimentary rocks and evaporites (Fig. 3.14b; Wade and MacLean, 1990). The presence of thick evaporites decoupled shallow deformation from deep deformation during rifting. Continued regional extension allowed salt to rise to the surface causing suprasalt strata to thin over the growing salt structures (Fig. 3.14c). Restoration to Late Triassic time indicates that much of the basement-involved extension occurred during the latter parts of the rifting phase (Fig. 3.14c).

During the later stages of rifting, widespread igneous activity affected the eastern margin of North America (Fig. 3.14d). The Central Atlantic Magmatic Province (CAMP) includes flood basalts, diabase dikes, and intrusive sheets that are dated to about 200 Ma (e.g., Olsen et al., 1996; Olsen, 1999; Schlische et al., 2003). In the Orpheus basin, early Jurassic (~200 Ma) magmatic activity is expressed as the intrusion of sills into Package A. As previously mentioned, the Early Jurassic Breakup Unconformity (BU) truncates these intrusions, which is further evidence that these intrusions are related to CAMP (Figs. 3.8a, 3.9-12). Also during this time, extensional forced folds (e.g., Withjack et al., 1990; Withjack and Callaway, 2000) developed over major basement fault blocks in the synrift strata above the salt (Fig 3.14d), whereas below the salt, faulting accommodated basement extension.

3.5.2. "Passive-Margin" Phase

Early Jurassic – Middle Jurassic Evolution (Fig 3.14e)

Additional episodes of deformation occurred after deposition of the youngest synrift strata (Package A) in the Orpheus basin during the transition from rifting to sea-floor spreading. During this time, synrift strata above the salt layer deformed into a series of tight, asymmetric synclines and salt-cored anticlines that further amplified preexisting extensional forced folds created during the rifting stage (Fig. 3.14d, e). Salt evacuation, coupled with further warping of unit A_3, formed vertical welds and detached thrust faults in areas above basement fault blocks where salt structures were present during rifting. At the same time, below the salt layer, the faults within the CCFS reactivated with at least a component of reverse slip. As during rifting, the Argo Formation (unit A_2) effectively decoupled deeper subsalt deformation from shallower suprasalt deformation. Below the salt, basement deformation was localized within the fault zones, whereas above the salt layer, deformation (i.e., folding) was more widely distributed in areas where thicker salt was present, and more localized in areas where salt was thin or no longer present (i.e., detached faulting) (Fig. 3.14e).

The presence of buckle folds, subvertical welds, and thrust faults suggests that this second episode of deformation was compressional (Vendeville and Nilsen, 1995; Bonini, 2003; Roca et al., 2006). Furthermore, because the Breakup Unconformity is relatively undeformed (Fig. 3.14e), whereas the synrift strata below it are intensely deformed, this compressional event likely occurred during the final stages of the rift-drift transition (3.14d; also see Withjack et al., 1998).

Also, the fact that Package B is absent above the CCFS, but present south of this zone (Figs. 3.6, 3.10, 3.14e), suggests that the North Step remained uplifted and subaerially exposed from the time of breakup in the mid/late Early Jurassic to the early Middle Jurassic when the entire margin began to subside. In the deeper parts of the Orpheus basin south of the North Step, however, salt-related subsidence continued forming the early Scotian basin above the Breakup Unconformity (Fig. 3.5, 3.6, 3.10).

Middle Jurassic to Cretaceous Evolution (Fig. 3.14f-h)

By the late Middle Jurassic, seafloor spreading was well underway (Withjack and Schlische, 2005). The preservation of the Middle Jurassic strata on the North Step is likely related to salt withdrawal during periods of tectonic quiescence after Early Jurassic inversion. South of the North Step, deposition of thick sediment wedges above the synrift infill prevented the further growth of salt structures; however, withdrawal-related subsidence likely continued in both areas until all the salt was displaced beneath the sediment pods, or subsequent phases of deformation again rejuvenated salt movement by removing the thick overburden above the salt layer (Figs. 3.5, 3.6, 3.10; MacLean and Wade, 1992; Vendeville and Nilsen, 1995).

A third episode of deformation occurred during the early Early Cretaceous when, according to previous workers (e.g., Wade and MacLean, 1990; Sinclair, 1995), the eastern margin of Canada in the Grand Banks region underwent a breakup episode. Currently, it is unclear if this event caused the widespread uplift and erosion that formed the base Cretaceous Avalon Unconformity (Fig. 3.14g). Also at this time, intrusive sills and possibly flows represent Early Cretaceous igneous activity. These rocks are both sampled in several wells (e.g., Jansa and Pe-Piper, 1985, 1988; Pe-Piper and Jansa, 1987) and are present on seismic lines in the study area. Locally above the intrusions, both Package C and the Avalon Unconformity are uplifted. Growth strata in Package D that thin over this high are also further evidence that this igneous event occurred during Early Cretaceous time (Figs. 3.8b, 3.13).

The Cretaceous in the Orpheus basin represents a second period of tectonic quiescence dominated by localized salt tectonics and regional subsidence (Fig. 3.14h). Pe-Piper et al. (2004) noted that another igneous event occurred during the late Early Cretaceous. Although these rocks have been sampled in several wells, both within the most western extent of the Orpheus basin and on the Grand Banks (Pe-Piper et al., 1994), these rocks do not produce distinctive reflections like those associated with previous magmatic activity.

Early Cenozoic to Recent Evolution (Fig. 3.14i)

Like the Cretaceous, the early part of the Cenozoic was dominated by regional subsidence (Package D_2). Today, however, the Cretaceous and Cenozoic sequences are deformed into synclines and salt-cored anticlines, and some basement faults show increased normal separation on the North Step, representing a fourth regional tectonic event affecting both the Orpheus basin and overlying Scotian basin (Figs. 3.5-7, 3.10-12, Fig. 3.14i). South of the North Step, rejuvenation of diapirism mainly in the western parts of the basin caused salt to pierce both the later Cretaceous and younger strata. The lack of growth beds within both the Cretaceous and early Cenozoic packages suggest that deformation occurred after their deposition. Uplift during or shortly after the formation of these structures is expressed by a very prominent horizontal seaward-dipping unconformity dated by MacLean and Wade (1992) as Oligocene. The simplest interpretation for these post-depositional structures is that they are at least partly related to compression before or during the Oligocene. Studies by Pe-Piper and Piper (2004) suggested that regional uplift during the Oligocene is related to yet another reactivation of the CCFS; however, this event is poorly understood and needs further investigation.

3.6. DISCUSSION

The presence of salt in the Orpheus basin greatly affected the style of deformation from the Late Triassic onward (see Fig. 3.14c-d). In the Orpheus basin, extensional deformation was localized on normal faults within the basement and prerift strata below the salt during Triassic rifting (Fig. 3.14b-d). Above the salt, extension was more distributed and accommodated simultaneously by different processes. The depositional loci, which formed by the uneven extension of the underlying Argo salt, were isolated into “pods” by intervening salt structures (Fig. 3.14c-d). During synrift deposition, the salt was progressively displaced from under the sediment pods forming asymmetric salt ridges or walls that likely reached the surface. During this process, known as passive diapirism or downbuilding (Vendeville and Jackson, 1992a, b), the salt body simultaneously rose as the surrounding strata subsided around it. As regional extension formed new basement faults below the salt (Fig. 3.14d), the southern end of the North Step began to subside more rapidly. In response, the width of sediment pods increased as the salt walls began to migrate basinward. In areas where salt structures do not reach the surface, broad extensional forced folds develop above the basement fault blocks. The locations of forced folds and salt structures, such as diapirs, salt walls or ridges that deform the sedimentary cover during rifting are important because subsequent episodes of deformation after rifting preferentially reactivated and amplified these structures (Figs. 3.14d-i, 3.15).

During subsequent tectonic events, cover deformation was at least partially decoupled from basement deformation, and as during rifting, accommodated simultaneously by different processes. Below the salt, shortening reactivated the CCFS with at least a component of reverse slip. In the cover above the salt layer, shortening, related to inversion of the CCFS, squeezed the preexisting salt ridges forming subvertical welds (Figs. 3.14e, 3.15). In cases where salt structures were absent after rifting, the Argo Salt functioned mainly as a detachment horizon. Above thin salt or squeezed salt structures (Figs. 3.14e, 3.15), detached thrusts and smaller folds deform the sedimentary cover. In areas where thick salt and/or preexisting extensional forced folds are present, more open, larger-amplitude detachment folds are possible where salt filled the cores of growing anticlines. It is also quite plausible that during this shortening event, the salt was displaced upward and outward onto the surface and later dissolved during the late Early Jurassic when the North Step was subject to erosion rather than deposition (see Fig 22b in Hudec and Jackson, 2007). This process would also create similar structural geometries, indicating that there are a number of geologically valid scenarios that could explain the development of these structures.

3.6.1. Comparisons to Previous Work

A lack of consensus exists among previous workers regarding the development of the Orpheus and overlying Scotian basins (Fig. 3.16). Pe-Piper and Piper (2004) and Weir-Murphy et al. (2004) discussed the development of the northern Scotian Shelf using both field and seismic data, whereas MacLean and Wade (1992) used seismic data to decipher the tectonic history of the northern Scotian Shelf. The investigation by MacLean and Wade (1992) is the only study that uses some of the same seismic data, and it is the only one that is directly compared with this work. They concluded that postrift deformation, aside from the formation of the Avalon Unconformity, was the result of the eastward evacuation of the Argo Salt in deeper parts of the basin south of the North Step. On the North Step, they attribute localized diapirism after the onset of sea floor spreading in the Early Jurassic as the main cause of structural deformation.

The conclusions of MacLean and Wade (1992) are based on only the 27 2D seismic line survey (the Laurentian Basin Survey) available at that time. The current database contains more than 150 2D seismic lines that provide better coverage over the study area. Subsequent to the work by MacLean and Wade (1992), workers in the field of salt tectonics, especially those that investigate salt tectonics during regional shortening (e.g., Vendeville and Nilsen, 1995; Letouzey et al., 1995; Bonini, 2003; Roca et al., 2006; Del Ventisette et al., 2005) has provided new insights on: 1) how the presence of salt can affect, and sometimes mask, known styles of deformation by decoupling deformation above and below the salt layer, 2) the processes that lead to and prevent the formation of salt structures, and 3) how preexisting salt structures react during multiple phases of regional deformation.

As previously mentioned, MacLean and Wade (1992) noted the presence of Late Jurassic to early Cenozoic deformation, but attributed salt evacuation and diapirism as the cause of this deformation. Salt movement likely occurred from the Early Jurassic onward, but the extent to which these strata are deformed cannot be attributed to salt tectonics alone. Because salt structures can arch, lift, and even pierce thick roofs in some cases, the idea that localized buoyancy-driven salt tectonics is the main driver of deformation in passive margin basins with salt is common (Vendeville and Nilsen, 1995). New insights on the behavior of salt, however, indicate that active diapirism driven by buoyancy alone is prevented by cover sequences as thin as one-third of the diapir height (Weijermars et al., 1993; Schultz-Ela et al., 1993; Jackson and Vendeville, 1994; Vendeville and Nilsen, 1995). The fact that some diapirs in the northern Scotian basin deform very thick roofs suggests that the rise of these diapirs was not driven by buoyancy, but rather by regional compression that squeezed the salt structures, forcing them upward causing the cover to deform.

Furthermore, shortening preferentially reactivates preexisting salt structures, rather than creating new ones, because they are weaker than the surrounding overburden. Therefore, the cover above either buried or exposed salt structures tends to shorten much more than adjacent areas of thicker overburden (i.e., south of the North Step; Hudec and Jackson, 2007). On the North Step, in both the Orpheus basin and overlying Scotian basin, deformation is localized around salt structures rather than in deeper parts of the basin. Also, without proper imaging of the disharmonic relationship between the folded synrift beds below the BU and folded postrift beds above it, it would be very easy to misinterpret the regional processes responsible for the cause deformation observed here.

3.6.2. Comparison to the Minas subbasin, onshore Nova Scotia

The Minas subbasin is an E-trending component of the Fundy rift basin bounded on the north by the Cobequid-Chedabucto fault zone (CCFS; also known as the Minas fault zone). It is similar to its offshore counterpart, the Orpheus basin (Tankard and Welsink. 1989; Olsen and Schlische, 1990; MacLean and Wade, 1992; Withjack et al., 1995, 2009). Many workers (e.g., Tankard and Welsink, 1989; MacLean and Wade, 1992; Withjack et al., 1995; Wade et al., 1996; Tanner and Brown, 2003) infered that because the onshore Minas subbasin and the offshore Orpheus basin share a common border-fault system, the tectonic events that affected the E-striking structures in the onshore Fundy basin likely affected the E-striking structures offshore as well. Today, the presence of faults with reverse separation, tight folds, and steeply dipping beds (Withjack et al., 1995; Baum, 2003; Baum et al., 2008) suggest that compressional deformation affected the margins of the Minas subbasin (Fig. 3.2c-d, 3.17).

Comparison of seismic profiles from the Minas basin with seismic profiles from the Orpheus basin indicate that the gross structural geometries of both basins are quite similar, although the border-fault zone in the Orpheus basin is significantly wider than that in the Minas subbasin. The preservation of Middle to Late Jurassic strata in the

Orpheus basin, and not the Minas subbasin, is related to: 1) the presence and withdrawal of Argo salt and/or 2) an increased amount of subsidence seaward. Although Baum et al. (2008) defined the 3D geometry and kinematics of inversion structures in the Fundy rift basin, using seismic, field, aeromagnetic, and DEM data, it is not known which postrift shortening event produced the structures observed in the Fundy basin (see Fig. 3.17). The work presented in this thesis suggests that the tectonic history of the Fundy basin is likely more complicated than previously thought, and that the NNE-shortening determined by Baum et al. (2008) may represent only the last episode of deformation to affect the margin of Nova Scotia and southern Newfoundland.

3.7. SUMMARY & CONCLUSIONS

- The offshore Orpheus basin is a buried E-trending fault-bounded Mesozoic rift basin on the northern margin of the Scotian Shelf affected by multiple episodes of Mesozoic to Cenozoic deformation. Like the onshore E-trending Minas subbasin of the Fundy basin, the Orpheus basin is bounded on the north by the E-striking Cobequid-Chedabucto fault system, a fault-zone that originally formed during the Paleozoic assemblage of Pangea.
- Four tectonostratigraphic packages, bounded by major angular unconformities, are present on recently acquired 2D seismic lines within the study area. Seismic horizons within these packages correlate with major biostratigraphic markers in five industry wells surrounding the study area. Package A comprises the synrift succession of clastic sedimentary rocks and thick evaporites (> 1 km in places), whereas Packages B through D comprise the postrift succession of clastic and carbonate sedimentary rocks. Seismic data from the Orpheus and Scotian basins

provide evidence of multiple episodes of deformation from the early Mesozoic to the early Cenozoic that are grouped into two phases: a rifting phase related to the formation of the Orpheus basin during the Middle Triassic to Early Jurassic, and a "passive margin" phase related to the formation of the Scotian basin beginning with the onset of seafloor spreading during the late Early Jurassic to early Middle Jurassic.

- Where salt was present above basement faults during rifting, cover deformation is decoupled from basement deformation. Forced folds and salt ridges developed in the cover above the salt, whereas below the salt layer, faulting accommodated basement extension. The second episode of deformation was compressional and occurred during the mid-Early Jurassic. As during rifting, deformation below the salt layer was decoupled from deformation above the salt layer. Subsalt shortening reactivated basement faults with at least a component of reverse slip, whereas above the salt layer, shortening further amplified extensional folds above basement fault blocks. Detached thrust faults and vertical salt welds also formed in response to this event, and uplift, associated with inversion of the Cobequid-Chedabucto fault system removed much of the later Early Jurassic strata on the North Step. A third episode of deformation occurred during the earliest Cretaceous forming a prominent angular unconformity. Regional uplift, possibly related to the breakup of the Grand Banks from Iberia, formed the widespread Avalon Unconformity on the northern margin of the Scotian Shelf. A fourth episode of deformation occurred during the early Cenozoic. During this event, Cretaceous and younger strata on the North Step were folded into anticlines and synclines, and many preexisting salt structures were further amplified. This work suggests that the tectonic history of the “passive” margin of offshore Nova Scotia is much more complex than previous thought.

- The edge of the passive margin of southeastern Canada experienced at least four stages of development: rifting, shortening during the rift/drift transition, regional uplift and erosion during the earliest Cretaceous, and a fourth event that had, at least locally on the North Step, a compressional component during the Oligocene. Because the main bounding faults of the Orpheus basin are the same as those in the Fundy basin, the kinematics of inversion in the Fundy basin (Baum, 2003; Baum et al., 2008; Withjack et al., 2009) may represent only the last episode of shortening during the Oligocene.

SECTION 4 – Comparison of Models with Geologic Examples from the Scotian Shelf and Future Work

4.1. Comparison of Models with Natural Examples

Generally, the geometries and evolutionary patterns observed in the synrift putty models in Section 2 aid in the interpretation and understanding of the structural evolution of areas where numerous salt structures are present (e.g., offshore eastern Canada; MacLean and Wade, 1992; Pe-Piper and Piper, 2004; eastern Prebetics, Spain; Roca et al., 2006). In this section, I compare the modeling results from both this thesis and previous work with geologic examples from eastern North America (Orpheus and overlying Scotian basins).

The structure of the northern Scotian Shelf (Fig. 3.3-4) is consistent with inversion of a rift basin affected by salt structures. Restoration of line 1124A-105 suggests that the inferred structure and evolution of the salt structures also fit well with the results of the analog models, where extension triggered diapirism (Model 2B (Fig. 2.14) and formed major salt structures. Surrounding the basement fault zone on the North Step, in both the Orpheus and Scotian basins, deformation is localized around salt structures, rather than in deeper parts of the basin (Fig. 3.5). In the models, much of the compressional deformation is preferentially accommodated by closing open putty ridges (Fig 2.16), by rejuvenating preexisting diapirs (Figs. 2.10, 2.12), and by further amplifying preexisting folds that formed during the extensional phase (Figs. 2.10, 2.12, 2.16, 2.17).

Similar to the models, the overburden above the salt layer on the North Step in the Orpheus basin is characterized by wide and slightly deformed synclines and by narrow and complex anticlines after the shortening phase (Figs. 2.12, 2.17, 3.6, 3.7). These complex anticlines are bounded by detached thrust faults and subvertical planar to squeezed diapiric bodies. The interpretation of the squeezed extension diapirs is supported by the presence of faults with normal separation below them, and precontractional sedimentary sequences above and around them. Some diapirs in the northern Scotian basin deform very thick roofs; this suggests that the rise of these diapirs were not driven by buoyancy, but rather by regional shortening that squeezed the salt structures, forcing them upward causing the cover to deform. Alternatively, in cases where diapirs developed after shortening, other modeling studies that examine the evolution of diapirs suggest their development can stem from the erosion of the crestal areas of salt-cored anticlines (Sans and Koyi, 2001), contractional generated differential loadings (Jackson and Vendeville, 1994), to vertical amplification and strain localization along detachment folds (Bonini, 2003).

The models presented here cannot reproduce and explain all the deformational geometries observed in areas affected by shortening. This is likely related to differences in the initial lithological configurations, the relative amounts of bulk shortening and extension, and/or the obliquity between the extension and shortening directions (Del Ventisette et al., 2006; Roca et al., 2006). In addition, syntectonic sedimentation and/or erosion, which could greatly affect the deformational style and history, have not been incorporated into the models. In this regard, they do not fully reproduce developed sediment pods, which form by differential loading (Hodgson et al., 1992; Rowan et al., 2003), or the erosional effects that both the Breakup Unconformity and base Cretaceous Avalon Unconformity (Figs. 3.10-11) had on the development or rejuvenation of salt structures (Vendeville and Nilsen, 1995; Roca et al., 2006; Hudec and Jackson, 2007). If preservation conditions are adequate and syntectonic sedimentation rates are not significantly greater than diapiric rise rates, they could also include isolated remains of the overhangs formed during the squeezing of preshortening salt structures over the horsts bounding the grabens (i.e., in Models 2A & 2B). In the Orpheus basin and overlying Scotian basin, multiple phases of uplift and erosion removed these features if they were present on the North Step.

4.2. Future Work

Much of Section 3 of this thesis presents a new hypothesis for the evolution of the northern Scotian Shelf. Although deformation patterns in the models are similar to those present on seismic data from the Orpheus basin and overlying Scotian basin, many questions still remain unanswered. Therefore possible future work should include:

- Perform additional experimental models with a salt analog that simulates oblique slip on major basement faults. Withjack et al. (1995) suggested that, because the E-striking Cobequid-Chedabucto fault system (CCFS) is the northern boundary of both the onshore Minas subbasin and the offshore Orpheus basin, it is likely that both basins have similar tectonic histories (Fig 3.18). It is well known that the Fundy and Minas fault systems experienced oblique movement both during rifting and during shortening (Withjack et al., 1995; Baum et al., 2008; Withjack et al., 2009). Therefore, an additional series of map-view experiments may give further insight into how the presence of a synrift salt layer reacts during multiple phases of oblique deformation.

- Perform preliminary experimental models with salt analog that simulates syntectonic deposition during extension. Because differential loading above a salt layer can greatly affect deformation patterns, these models will aid in understanding of how sedimentation will either encourage or hinder the growth of salt structures.
- Perform multi-layer extensional and contractional models for cross-sectional analysis. Because the models analyzed in this study only examine map-view deformation patterns, cross-sectional analysis of multi-layer models can be compared with seismic sections from the northern Scotian Shelf to better understand the influence of the preexisting extensional fabric on the geometries of compressional structures in profile. It will also help better identify which structures are reactivated and which are newly formed during the shortening phase.
- Perform additional mapping of the seismic dataset in both the Orpheus basin and overlying Scotian basin. Additional subsurface mapping will aid in a better understanding of the 3D geometry of structures, both basement involved and detached. If the shortening-related folds are completely detached from the basement, their trends may reflect the shortening direction during inversion. Because the folds within the synrift sequences are disharmonic with the folds in the Cretaceous and younger strata, their trends may be different as well.

References Cited

Alsop, G. I., 1996, Salt Tectonics: Geological Society Special Publications, v. 100, p. 1996.

Alves, T. M., Manuppella, G., Gawthorpe, R. L., Hunt, D. W., and Monteiro, J. H., 2003, The depositional evolution of diapir- and fault-bounded rift basins: examples from the Lusitanian Basin of West Iberia: Sedimentary Geology, v. 162, p. 273-303.

Baum, M. S., Withjack, M. O., and Schlische, R. W., 2003, Controls on structural geometries associated with rift-basin inversion: AAPG Annual Meeting Abstracts, v. 12, p. A10.

Baum, M. S., 2006, Controls on the Deformation Produced by Oblique Inversion of Rift Basins: Which Structures Reflect the Paleostrain State?: Ph.D Dissertation - Rutgers University.

Bonini, M., 2003. Detachment folding, fold amplification, and diapirism in thrust wedge experiments. Tectonics 22 (6), 1065, doi:10.1029/2002TC001458

Brun, J. P. and Nalpas, T., 1996, Graben inversion in nature and experiments: Tectonics, v. 15, p. 677-687.

Byerlee, J., 1978, Friction of rocks: Pure and Applied Geophysics, v. 116, p. 615-626.

Cloos, E., 1968, Experimental analysis of Gulf Coast fracture patterns: Aapg Bulletin, v. 52, p. 420-444.

Coward, M., Stewart, S., 1995. Salt-influenced structures in the Mesozoic–Tertiary cover of the southern North Sea, U.K. In: Jackson, M.P.A., Roberts, D.G., Snelson, S. (Eds.), Salt Tectonics. A Global Perspective. AAPG Memoir 65, pp. 229–250.

Del Ventisette, C., Montanari, D., Bonini, M., and Sani, F., 2005, Positive fault inversion triggering 'intrusive diapirism': an analogue modeling perspective: Terra Nova, v. 17, p. 478-485.

Del Ventisette, C., Montanari, D., Sani, F., and Bonini, M., 2006, Basin inversion and fault reactivation in laboratory experiments: Journal of Structural Geology, v. 28, p. 2067-2083.

Dooley, T., McClay, K.R., Hempton, M., Smit, D., 2005. Salt tectonics above complex basement extensional fault systems: results from analogue modeling. In: Dore´ , A.G., Vining, B.A. (Eds.), Petroleum Geology: North-West Europe and Global Perspectives: Proceedings of the 6th Petroleum Geology Conference. Geological Society, London, pp. 1631–1648.

Dooley, T. P., Jackson, M. P. A., and Hudec, M. R., 2009, Inflation and deflation of deeply buried salt stocks during lateral shortening: Journal of Structural Geology, v. 31, p. 582-600.

Eisenstadt, G. and Withjack, M. O., 1995, Estimating inversion; results from clay models: Geological Society Special Publications, v. 88, p. 119-136.

Eisenstadt, G. and Sims, D., 2005, Evaluating sand and clay models: do rheological differences matter?: Journal of Structural Geology, v. 27, p. 1399-1412.

Gartrell, A., Hudson, C., and Evans, B., 2005, The influence of basement faults during extension and oblique inversion of the Makassar Straits rift system: Insights from analog models: Aapg Bulletin, v. 89, p. 495-506.

Ge, H. X., Jackson, M. P. A., and Vendeville, B. C., 1997, Kinematics and dynamics of salt tectonics driven by progradation: Aapg Bulletin-American Association of Petroleum Geologists, v. 81, p. 398-423.

Ge, H. X. and Jackson, M. P. A., 1998, Physical modeling of structures formed by salt withdrawal: Implications for deformation caused by salt dissolution: Aapg Bulletin-American Association of Petroleum Geologists, v. 82, p. 228-250.

Handin, 1966. Strength and Ductility. In: S.P. Clark (Ed.), Handbook of Physical Constants, 97. Geological Society of America Memoir, pp. 233-289.

Hubbert, M.K., 1937. Theory of scale models as applied to the study of geological structures. Geological Society of America Bulletin 48, 1459-1519.

Hudec, M. R. and Jackson, M. P. A., 2007, Terra infirma: Understanding salt tectonics: Earth-Science Reviews, v. 82, p. 1-28.

Jackson, M.P.A., Talbot, C.J., 1986. External shapes, strain rates, and dynamics of salt structures. Geological Society of America Bulletin 97, 305–323.

Jackson, M. P. A., Vendeville, B. C., and Schultz-Ela, D. D., 1994, Structural Dynamics of Salt Systems: Annual Review of Earth and Planetary Sciences, v. 22, p. 93-117.

Jackson, M. P. A. and Vendeville, B. C., 1994, Regional Extension As A Geologic Trigger for Diapirism: Geological Society of America Bulletin, v. 106, p. 57-73.

Jansa, L. F. and Pe-Piper, G., 1985, Early Cretaceous Volcanism on the Northeastern American Margin and Implications for Plate-Tectonics: Geological Society of America Bulletin, v. 96, p. 83-91.

Jansa, L. F. and Pe-Piper, G., 1988, Middle Jurassic to Early Cretaceous Igneous Rocks Along Eastern North-American Continental-Margin: AAPG Bulletin-American Association of Petroleum Geologists, v. 72, p. 347-366.

Jansa, L. F., and J. A. Wade, 1975, Geology of the continental margin off Nova Scotia and Newfoundland, in W. J. M. van der Linden and J. A. Wade, eds., Offshore geology of eastern Canada, v. 2: Regional geology: Geological Survey of Canada Paper 74-30, p. 51–106.

Koyi, H. A., Jenyon, M. K., and Petersen, K., 1993, The effect of basement faulting on diapirism: Journal of Petroleum Geology, v. 16, p. 285-311.

Koyi, H. A. and Sans, M., 2006, Deformation transfer in viscous detachments; comparison of sandbox models to the South Pyrenean triangle zone: Geological Society Special Publications, v. 253, p. 117-134.

Le Calvez, J.H., and B.C. Vendeville, 2002, Experimental designs to model along-strike fault interaction: Journal of the Virtual Explorer (online), v. 7, p. 7-23.

Letouzey, J., Colletta, B., Vially, R., Chermette, J.C., 1995. Evolution of salt-related structures in compressional settings. In: Jackson, M.P.A., Roberts, D.G., Snelson, S. (Eds.), Salt Tectonics: A Global Perspective. AAPG Memoir 65, pp. 41–60.

MacLean, B.C., and J.A. Wade, 1992, Petroleum geology of the continental margin south of the islands of St. Pierre and Miquelon, offshore Eastern Canada: Bulletin of Canadian Petroleum Geology, v. 40, p. 222-253.

MacLean, B.C., and Wade, J.A. 1993. Seismic markers and stratigraphic picks in Scotian Basin wells. Atlantic Geoscience Centre, Geological Survey of Canada.

Mart, Y. and Dauteuil, O., 2000, Analogue experiments of propagation of oblique rifts: Tectonophysics, v. 316, p. 121-132.

McClay, K. R. and White, M. J., 1995, Analog Modeling of Orthogonal and Oblique Rifting: Marine and Petroleum Geology, v. 12, p. 137-151.

Nalpas, T. and Brun, J. P., 1993, Salt Flow and Diapirism Related to Extension at Crustal-Scale: Tectonophysics, v. 228, p. 349-362.

Nicol, A., J. J. Walsh, J. Watterson, and J. R. Underhill, 1997, Displacement rates of normal faults: Nature, v. 390, p. 157–159.

Olsen, P.E., P.M. Hanshaw, R.W. Schlische, P.J.W. Gore, 1989, Sedimentation and basin analysis in siliciclastic rock sequences; Volume 2, Tectonic, depositional, and paleoecological history of early Mesozoic rift basins, eastern North America: Field trips for the 28th international geological congress, Am. Geophys. Union, Washington, DC, United States, p. 174.

Olsen, P. E. and Schlische, R. W., 1990, Transtensional arm of the early Mesozoic Fundy rift basin: penecontemporaneous faulting and sedimentation: Geology, v. 18, p. 695-698.

Olsen, P. E., Kent, D. V., Cornet, B., Witte, W. K., and Schlische, R. W., 1996, High-resolution stratigraphy of the Newark rift basin (early Mesozoic, eastern North America): Geological Society of America Bulletin, v. 108, p. 40-77.

Olsen, P. E., 1997, Stratigraphic record of the early Mesozoic breakup of Pangea in the Laurasia-Gondwana rift system: Annual Review of Earth and Planetary Sciences, v. 25, p. 337-401.

Olsen, P. E., 1999, Geoscience - Giant lava flows, mass extinctions, and mantle plumes: Science, v. 284, p. 604-605.

Panien, M., Schreurs, G., and Pfiffner, A., 2005, Sandbox experiments on basin inversion: testing the influence of basin orientation and basin fill: Journal of Structural Geology, v. 27, p. 433-445.

Pe-Piper, G. and Piper, D. J. W., 2004, The effects of strike-slip motion along the Cobequid-Chedabucto-southwest Grand Banks fault system on the Cretaceous-Tertiary evolution of Atlantic Canada: Canadian Journal of Earth Sciences, v. 41, p. 799-808.

Pe-Piper, G. and Jansa, L. F., 1987, Geochemistry of Late Middle Jurassic-Early Cretaceous Igneous Rocks on the Eastern North-American Margin: Geological Society of America Bulletin, v. 99, p. 803-813.

Pe-Piper, G., Jansa, L.F., and Lambert R. St J., 1992. Early Mesozoic magmatism on the eastern Canadian margin: Petrogenetic and tectonic significance, *in* Puffer, J/H/. and Ragland, P.C. eds., Eastern North American Mesozoic Magmatism: Geological Society of America Special Paper 268

Pe-Piper, G., Jansa, L. F., and Palacz, Z., 1994, Geochemistry and Regional Significance of the Early Cretaceous Bimodal Basalt-Felsic Associations on Grand-Banks, Eastern Canada: Geological Society of America Bulletin, v. 106, p. 1319-1331.

Richardson, N. J., Underhill, J. R., and Lewis, G., 2005, The role of evaporite mobility in modifying subsidence patterns during normal fault growth and linkage, Halten Terrace, mid-Norway: Basin Research, v. 17, p. 203-223.

Roca, E., P. Anado´n, R. Utrilla, and A. Va´zquez, 1996, Rise, closure and reactivation of the Bicorb–Quesa diapir, eastern Prebetics, Spain: Journal of the Geological Society (London), v. 153, p. 311– 321.

Roca, E., Sans, M., and Koyi, H.A., 2006. Polyphase deformation of diapiric areas in models and in the eastern Prebetics (Spain). AAPG Bulletin 90 (1), 115–136.

Rowan, M. G., Trudgill, B. D., and Fiduk, J. C., 2000, Deep-water, salt-cored foldbelts; lessons from the Mississippi Fan and Perdido foldbelts, northern Gulf of Mexico: Geophysical Monograph, v. 115, p. 173-191.

Sans M., and Koyi, H., 2001. Modeling the role of erosion in diapir development. In: Koyi, H.A., Mancktelow, N.S. (eds.). Tectonic Modelling: AVolume in Honor of Hans Ramberg. Geological Society of America Memoir, 193, 111-122.

Schlische, R. W. and Ackermann, R. V., 1995, Kinematic Significance of Sediment-Filled Fissures in the North Mountain Basalt, Fundy Rift Basin, Nova-Scotia, Canada: Journal of Structural Geology, v. 17, p. 987-996.

Schlische, R. W., Withjack, M. O., and Eisenstadt, G., 2002, An experimental study of the secondary deformation produced by oblique-slip normal faulting: Aapg Bulletin, v. 86, p. 885-906.

Schlische, R. W., Withjack, M. O., and Olsen, P. E., 2003, Relative Timing of CAMP, Rifting, Continental Breakup, and Basin Inversion: Tectonic Significance: Geophysical Monograph, v. 136, p. 33-59.

Schultz-Ela, D. D. and Jackson, M. P. A., 1996, Relation of subsalt structures to suprasalt structures during extension: Aapg Bulletin-American Association of Petroleum Geologists, v. 80, p. 1896-1924.

Schultzela, D. D., Jackson, M. P. A., and Vendeville, B. C., 1993, Mechanics of Active Salt Diapirism: Tectonophysics, v. 228, p. 275-312.

Sinclair, I. K., 1995, Sequence stratigraphic response to Aptian-Albian rifting in conjugate margin basins; a comparison of the Jeanne d'Arc Basin, offshore Newfoundland, and the Porcupine Basin, offshore Ireland: p. 29-49.

Stewart, S. A., 1996b, Influence of detachment layer thickness on style of thin-skinned shortening: Journal of Structural Geology, v. 18, p. 1271-1274.

Stewart, S. A., Harvey, M. J., Otto, S. C., and Weston, P. J., 1996a, Influence of salt on fault geometry; examples from the UK salt basins: Geological Society Special Publications, v. 100, p. 175-202.

Stewart, S. A., Ruffell, A. H., and Harvey, M. J., 1997, Relationship between basement-linked and gravity-driven fault systems in the UKCS salt basins: Marine and Petroleum Geology, v. 14, p. 581-604.

Tankard, A.J. and Welsink, H.J. 1989. Mesozoic extension and styles of basin formation in Atlantic Canada, *in* Tankard, A.J., and Balkill, eds., Extensional Tectonics and Stratigraphy of the North Atlantic Margin, pp. 175-1995: AAPG Memoir, vol. 46

Vendeville, B. C., and Jackson, M. P. A., 1992a, The rise of diapirs during thin-skinned extension: Marine and Petroleum Geology, v. 9, p. 331-353.

Vendeville, B. C., and Jackson, M. P. A., 1992b, The fall of diapirs during thin-skinned extension: Marine and Petroleum Geology, v. 9, p. 354-371.

Vendeville, B. C., Ge, H., and Jackson, M. P. A., 1995, Scale models of salt tectonics during basement-involved extension: Petroleum Geoscience, v. 1, p. 179-183.

Vendeville, B.V., and Nielsen, K.T., 1995, Episodic growth of salt diapirs driven by horizontal shortening: Gulf Coast Section SEPM Foundation 16th Annual Research Conference, Salt, Sediment and Hydrocarbons, p. 285–295.

Wade, J. A. and MacLean, B. C., 1990, Aspects of the geology of the Scotian Basin from recent seismic and well data; the geology of the southeastern margin of Canada: Geological Society of America Special Pub.

Wade, J. A., MacLean, B. C., and Williams, G. L., 1995, Mesozoic and Cenozoic Stratigraphy, Eastern Scotian Shelf - New Interpretations: Canadian Journal of Earth Sciences, v. 32, p. 1462-1473.

Wade, J. A., Brown, D. E., Traverse, A., and Fensome, R. A., 1996, The Triassic-Jurassic Fundy Basin, eastern Canada: Regional setting, stratigraphy and hydrocarbon potential: Atlantic Geology, v. 32, p. 189-231.

Weijermars, R., Jackson, M. P. A., and Vendeville, B., 1993, Rheological and tectonic modeling of salt provinces: Tectonophysics, v. 217, p. 143-174.

Weir Murphy, S.L., Pe-Piper, G., Piper, D.J.W., and MacRae, R.A. 2004. Cretaceous rocks of the Orpheus graben, offshore Nova Scotia. Atlantic Geoscience Society Colloquium, Program and Abstracts, 30: 32.

Williams, G. D., C. M. Powell, and M. A. Cooper. 1989. Geometry and kinematics of inversion tectonics *in* Inversion tectonics meeting: Geological Society Special Publications, v. 44 p. 3-15

Withjack, M. O. and Jamison, W. R., 1986, Deformation produced by oblique rifting: Tectonophysics, v. 126, p. 99-124.

Withjack, M. O., Meisling, K. E., and Russell, L. R., 1988, Forced Folding and Basement-Detached Normal Faulting in the Haltenbanken Area, Offshore Norway: Aapg Bulletin-American Association of Petroleum Geologists, v. 72, p. 259.

Withjack, M. O., Olson, J., and Peterson, E., 1990, Experimental Models of Extensional Forced Folds: Aapg Bulletin, v. 74, p. 1038-1054.

Withjack, M. O., Olsen, P. E., and Schlische, R. W., 1995, Tectonic Evolution of the Fundy Rift Basin, Canada - Evidence of Extension and Shortening During Passive Margin Development: Tectonics, v. 14, p. 390-405.

Withjack, M. O., Schlische, R. W., and Olsen, P. E., 1998, Diachronous rifting, drifting, and inversion on the passive margin of central eastern North America: An analog for other passive margins: Aapg Bulletin, v. 82, p. 817-835.

Withjack, M. O. and Callaway, S., 2000, Active normal faulting beneath a salt layer: An experimental study of deformation patterns in the cover sequence: Aapg Bulletin, v. 84, p. 627-651.

Withjack, M. O. and Schlische, R. W., 2006, Geometric and experimental models of extensional fault-bend folds: Geological Society Special Publications, v. 253, p. 285-305.

Withjack, M. O., Schlische, R. W., and Olsen, P. E., 2002, Rift-basin structure and its influence on sedimentary systems: Special Publication - Society for Sedimentary Geology, v. 73, p. 57-81.

Withjack, M.O., Schlische, R.W., Henza, A.A., 2007. Scaled experimental models of extension: dry sand vs. wet clay. Houston Geological Survey Bulletin 49 (8), 31-49.

APPENDIX 1

Scaling

Most scaled experimental models use either dry sand or wet clay as the primary modeling material. In this study, similar to other modeling studies (e.g., Withjack and Callaway 2000; Eistenstadt and Sims, 2005, Withjack and Schlische, 2006; Withjack et al., 2007), wet clay represents upper crustal rocks. It is composed mainly of kaolinite particles (<0.005 mm in diameter) and water (~40% by weight) and has a density of 1.55-1.60 g cm^{-3}. Its coefficient of internal friction is ~0.6, and its cohesive strength is ~ 50 Pa. For comparison with a natural prototype, experimental models must be geometrically, kinematically, and dynamically similar (Hubbert, 1937). Because the strength of most rocks in the upper crust increases with depth (e.g., Byerlee, 1978), the modeling materials must behave in a similar fashion. Accordingly,

$$\tau = C_0 + \mu\sigma_n \qquad (1)$$

where τ and σ_n, are the shear and normal stresses on a potential fault surface, C_0 is the cohesion, and μ is the coefficient of internal friction. This relationship, however, only describes the initiation of new faults, not the reactivation of existing faults. For most sedimentary rocks, the coefficient of internal friction ranges from roughly 0.55 to 0.85 (e.g., Handin, 1966; Byerlee, 1978).

Properly scaled experimental models require two conditions to achieve dynamic similarity (Weijermars et al., 1993; Vendeville et al., 1995; Withjack and Callaway, 2000). First, the modeling materials and rocks in the upper crust must have similar coefficients of internal friction (resulting in geometric similarity). Second,

$$C_0^* = \rho^* \bullet g^* \bullet l^* \qquad (2)$$

the cohesive strength ratio (C_0^*) between the model and prototype must equal the product of the model-to-prototype ratios for density (ρ^*), gravity (g^*), and length (l^*), ensuring dynamic similarity between the models and nature (e.g., Hubbert, 1937; Weijermars et al., 1993; Vendeville et al., 1995). In these models, the values of ρ^* and g^* are roughly 0.62 and 1.0, respectively. Thus, (C_0^*), and the length ratio (l^*) must have similar magnitudes to ensure dynamic similarity. In nature, C ranges from less than 1 MPa (for loosely compacted sedimentary rocks) to more than 10 MPa (for intact crystalline rocks) (Handin, 1966). As mentioned previously, the wet clay in our models has a cohesive strength of ~50 Pa, resulting in a value of C^* between 10^{-4} and 10^{-6}. Therefore, L^* ranges between 10^{-4} and 10^{-6} in our models, depending on the cohesion of the natural prototype. If the clay simulates a layer of loosely compacted sedimentary rock, then 1 cm in the model represents ~100 m in nature. Alternatively, if the clay simulates intact crystalline rock, then 1 cm in the model represents about ~10 km in nature. In my models, 8 cm represents roughly 15 km in nature (i.e., the thickness of the brittle crust).

To simulate the ductile behavior of salt (viscosity ~10^{16} – 10^{20} Pa s), dynamic similarity is achieved by using a viscous silicone polymer, whose effective viscosity (μ_m) is about 1.0 x 10^3 Pa s (Vendeville et al., 1995; Withjack and Callaway, 2000; Koyi and Sans, 2006).

Following Withjack and Callaway (2000), dynamic similarity between the models and natural prototypes when strata deform by viscous flow is achieved by,

$$d_r^* = \left[\rho^* \bullet g^* \bullet \left(l^*\right)^2\right] \Big/ \mu^* \qquad (3)$$

where d_r^* and μ^* are model-to-prototype ratios for displacement rate and viscosity, respectively (e.g., Hubbert, 1937; Weijermars et al., 1993; Vendeville et al., 1995).

Appropriate values for displacement rates in the models are determined by reformatting equation 3, allowing,

$$d_{rm} = \left(\rho^* \bullet g^* / \mu_m\right) \bullet \left(l^*\right)^2 \bullet P \qquad (4)$$

where d_{rm} is the displacement rate of the moving wall the models, μ_m is the viscosity of the putty layer, and $P = d_{rn} \bullet \mu_n$, the product of the displacement rate on a master normal fault in nature and the viscosity of a natural salt layer. In the models, d_{rm} is 3.0 cm hr^{-1} (or 8.3 x 10^{-4} cm s^{-1}) for the extensional phase. Accordingly, natural displacement rates (i.e., rates of extension), which range from about 1 to 10 mm yr^{-1} (or 10^{-7} to 10^{-8} cm s^{-1}), and salt viscosities, which range from less than 10^{16} to more than 10^{19} Pa s, indicate that $P = d_{rn} \bullet \mu_n$ ranges from about 10^5 to 10^{12} Pa cm (Withjack and Callaway, 2000). In the models, the value for d_{rm} represents a suite of natural conditions where P has the same value. For instance, the models can represent a scenario with lower natural fault displacement rates (~ 10^{-9} cm/s) and higher salt viscosity (~ 10^{20} Pa s) or natural conditions where fault displacement rates are high (~ 10^{-8} cm/s) and the salt viscosity is lower (~ 10^{17} Pa s).

APPENDIX 2

Properties of Silicone Polymer

CLEARCO

Properties of Polydimethylsiloxanes from 0.65cSt to 2.5 million cSt.

Product Code	Viscosity cSt	Viscosity Temp. Coefficient	Pour point °C	Flash Point °C	Specific Gravity	Refractive Index	Coeff. of Thermal Expansion cc/cc/°C, 0-150°C	Thermal Conductivity @ 25°C g /cal/cm/sec °C	Maximum Volatility, % wt. Loss, 24 hours @ 150°C	Surface Tension	Dielectric Constant	Dielectric Strength	Molecular Weight
Low Viscosities													
PSF-0.65cSt	.65	.32	-68	-1	.761	1.3750	0.00134	0.00024	100%	15.9	2.20	300	162
PSF-1cSt	1.0	.37	-85	39	.818	1.3825	0.00134	0.00024	100%	17.4	2.30	350	237
PSF-1.5cSt	1.5	.46	-75	63	.853	1.3880	0.00134	0.00024	100%	18.0	2.39	350	340
PSF-2cSt	2.0	.48	-80	79	.873	1.3900	0.00117	0.00025	100%	18.7	2.45	350	410
PSF-3cSt	3.0	.51	-70	100	.898	1.3935	0.00114	0.00026	100%	19.2	2.50	350	550
PSF-5cSt	5.0	.54	-65	135	.918	1.3970	0.00112	0.00027	90%	19.7	2.60	375	770
PSF-7cSt	7.0	.55	-65	150	.930	1.3980	0.00110	0.00028	N/a	19.9	2.65	375	950
PSF-10cSt	10	.56	-65	163	.935	1.3990	0.00108	0.00030	15%	20.1	2.68	375	1,250
PSF-20cSt	20	.59	-60	232	.950	1.4000	0.00107	0.00032	10%	20.6	2.72	375	2,000
Standard Viscosities													
PSF-50cSt	50	.59	-55	285	.960	1.4015	0.00106	0.00034	0.5%	20.8	2.75	400	3,780
PSF-100cSt	100	.60	-55	315	.966	1.4025	0.00093	0.00036	0.5%	20.9	2.75	400	5,970
PSF-200cSt	200	.60	-60	315	.968	1.4030	0.00093	0.00037	0.5%	21.0	2.75	400	9,430
PSF-350cSt	350	.60	-60	315	.970	1.4031	0.00093	0.00037	0.5%	21.1	2.75	400	13,650
PSF-500cSt	500	.60	-55	315	.971	1.4033	0.00093	0.00038	0.5%	21.1	2.75	400	17,250
PSF-1,000cSt	1,000	.61	-50	315	.971	1.4034	0.00093	0.00038	0.5%	21.2	2.75	400	28,000
Hi-Viscosities													
PSF-5,000cSt	5,000	.61	-48	315	.973	1.4035	0.00093	0.00038	2%	21.3	2.75	400	49,350
PSF-10,000cSt	10,000	.61	-48	315	.974	1.4035	0.00093	0.00038	2%	21.5	2.75	400	62,700
PSF-12,500cSt	12,500	.61	-46	315	.974	1.4035	0.00093	0.00038	2%	21.5	2.75	400	67,700
PSF-30,000cSt	30,000	.61	-43	315	.976	1.4035	0.00093	0.00038	2%	21.5	2.75	400	91,700
PSF-60,000cSt	60,000	.61	-42	315	.976	1.4035	0.00093	0.00038	2%	21.5	2.75	400	116,500
PSF-100,000cSt	100,000	.61	-41	321	.977	1.4035	0.00092	0.00038	2%	21.5	2.75	400	139,000
PSF-300,000cSt	300,000	.61	-41	321	.977	1.4035	0.00092	0.00038		21.5	2.75	400	204,000
PSF-600,000cSt	600,000	.61	-41	321	.978	1.4035	0.00092	0.00038		21.6	2.75	400	260,000
PSF-1,000,000cSt	1,000,000	.62	-39	321	.978	1.4035	0.00092	0.00038		21.6	2.75	400	308,000
PSF-2,500,000cSt	2,500,000	.62	-38	321	.978	1.4035	0.00092	0.00038		21.6	2.75	400	423,000
PSF-20,000,000cSt	20,000,000	.62	-35	321	.979	1.4035	0.00092	0.00038		21.6	2.75	400	>500,000

APPENDIX 3

List of Seismic Lines

	Line Name	Min X	Max X	Min Y	Max Y	Company
1	1034-105	426389	431913	4984059	4935724	TGS/Nopec
2	1042-105	440723	440765	4993328.142	4970159	TGS/Nopec
3	1046-105	443548	447424	5078461	4926656	TGS/Nopec
4	1050-105	453483	453807	5078436	4969223	TGS/Nopec
5	1058-105	460017	460461	5078453	4970156	TGS/Nopec
6	1062-105	465544	466320	5078268	4969247	TGS/Nopec
7	1066-105	472210	472347	5078605	4961013	TGS/Nopec
8	1070-105	478076	478474	5078103	4960386	TGS/Nopec
9	1078-105	482383	483453	5078800	4923052	TGS/Nopec
10	1082-105	488064	489560	5078097	4922981	TGS/Nopec
11	1090-105	494596	495649	5078605	4923607	TGS/Nopec
12	1100A-105	500974	501862	5078442	4925173	TGS/Nopec
13	1108A-105	506837	508186	5078265	4926440	TGS/Nopec
14	1116A-105	511973	513784	5078794	4930438	TGS/Nopec
15	1124A-105	519032	519675	5078462	4930771	TGS/Nopec
16	1132A-105	524921	525988	5078101	4931408	TGS/Nopec
17	1140A-105	530757	531469	5078634	4936005	TGS/Nopec
18	1148A-105	536467	537214	5078102	4936356	TGS/Nopec
19	1205A-105	563094	607276.645	4945309.111	4945177	TGS/Nopec
20	1205B-105	477412	549026.006	4945194	4945151	TGS/Nopec
21	1206A-105	576506	576886	5044609	4939217	TGS/Nopec
22	1212A-105	582520	582891	5044977	4939896	TGS/Nopec
23	1224A-105	588836	588902	5044731	4939634	TGS/Nopec
24	1229-105	568930	725679.133	4958367	4958195	TGS/Nopec
25	1230A-105	594255	594844	5045072	4940330	TGS/Nopec

26	1238A-105	600823	600956	5044978	4942542	TGS/Nopec
27	1243A-105	568645	655534.027	4969048	4968298	TGS/Nopec
28	1243B-105	467146	539495.54	4967559	4967394	TGS/Nopec
29	1246A-105	606631	606720	5045462	4944613	TGS/Nopec
30	1254A-105	612774	613109	5045846	4945031	TGS/Nopec
31	1262A-105	618644	618859	5045344	4944848	TGS/Nopec
32	1267A-105	563006	742204.818	4980832	4980720	TGS/Nopec
33	1267B-105	419072	547220	4980619	4980099	TGS/Nopec
34	1270A-105	624786	624932	5045473	4944869	TGS/Nopec
35	1278A-105	630486	630636	5045831	4945612	TGS/Nopec
36	1281B-105	418728	542490	4994089	4993494	TGS/Nopec
37	1286A-105	636034	636783	5045718	4949199	TGS/Nopec
38	1294A-105	642166	642856	5045836	4946441	TGS/Nopec
39	1295B-105	411042	538513	5004235	5003642	TGS/Nopec
40	1309B-105	411480	542823	5014064	5013850	TGS/Nopec
41	1323B-105	411226	533164	5026016	5024843	TGS/Nopec
42	1337A-105	571761	610124.463	5038188	5038131	TGS/Nopec
43	1337B-105	410752	541890	5037569	5034541	TGS/Nopec
44	1351B-105	410325	550610	5048374	5047840	TGS/Nopec
45	1365B-105	410518	542579	5064995	5064230	TGS/Nopec
46	2001-LC	541079	541877	5099493	4941593	TGS/Nopec
47	2002-LC	543450	543785	5082805	4918637	TGS/Nopec
48	2003-LC	544201	544838	5082771	4941735	TGS/Nopec
49	2004-LC	545540	546612	5082871	4941989	TGS/Nopec
50	2005-LC	546149.935	547684	5082683.288	4941811	TGS/Nopec
51	2006-LC	547645.879	549212	5081704.637	4941806	TGS/Nopec
52	2007-LC	548461	550122	5103513	4941730	TGS/Nopec

53	2008-LC	550707	552242	5083022	4918676	TGS/Nopec
54	2009-LC	553050	554252	5103134	4941820	TGS/Nopec
55	2010-LC	555401	557222	5083203	4918670	TGS/Nopec
56	2011-LC	557612	559685	5103475	4941769	TGS/Nopec
57	2012-LC	560562.93	562435	5082987.181	4918652	TGS/Nopec
58	2013-LC	563141	564145	5103362	4941706	TGS/Nopec
59	2014-LC	565412.807	566106	5083016.326	4942246	TGS/Nopec
60	2015-LC	566287	567323	5082531	4918702	TGS/Nopec
61	2016-LC	568034	569531.073	5082727	4941686.722	TGS/Nopec
62	2018-LC	534373	577492.126	4928073	4928034	TGS/Nopec
63	2019-LC	534410	577532	4938101	4938052	TGS/Nopec
64	2020-LC	534293	577418	4958338	4958203	TGS/Nopec
65	2021-LC	534106	577375	4963001	4962459	TGS/Nopec
66	2022-LC	534162	576676	4968415	4967323	TGS/Nopec
67	2023-LC	534232	582812.44	4971137	4970077	TGS/Nopec
68	2024-LC	534242	582716	4973659	4972760	TGS/Nopec
69	2025-LC	534446	583070.503	4975760.281	4974950	TGS/Nopec
70	2026-LC	534399	583030	4977488	4976664	TGS/Nopec
71	2027-LC	534213	577517.148	4979213.073	4978540	TGS/Nopec
72	2028-LC	534320	577368	4980991	4980499	TGS/Nopec
73	2029-LC	534346	577461.129	4982107	4981492	TGS/Nopec
74	2030-LC	534321	577368	4982979	4982563	TGS/Nopec
75	2031-LC	534346	582706.3	4985646.418	4984723	TGS/Nopec
76	2032-LC	534547	583010.514	4988809.105	4987545	TGS/Nopec
77	2033-LC	534508	577280.096	4994935	4994014	TGS/Nopec
78	2034-LC	534418	577189.089	5001951.27	5000940	TGS/Nopec
79	2035-LC	529283	577114.295	5005148.186	5004148	TGS/Nopec

80	2036-LC	529222	577059	5007475	5006617	TGS/Nopec
81	2037-LC	529174	577084.295	5009833.029	5009031	TGS/Nopec
82	2038-LC	534125	577128	5012272	5011515	TGS/Nopec
83	2040-LC	534081	582442.357	5014943.09	5014037	TGS/Nopec
84	2042-LC	534203	582491	5017913	5017017	TGS/Nopec
85	2043-LC	534184	577146.084	5020640	5019837	TGS/Nopec
86	2044-LC	534125	576977	5023174	5022336	TGS/Nopec
87	2045-LC	534274	576822.987	5025609.262	5024760	TGS/Nopec
88	2046-LC	528891	576804	5026848	5025935	TGS/Nopec
89	2047-LC	529045	576844	5029414	5028478	TGS/Nopec
90	2049-LC	528734	576532.157	5030702.147	5029848	TGS/Nopec
91	2050-LC	534002	576216	5034221	5033378	TGS/Nopec
92	2051-LC	533953	576205.837	5038053.05	5037470	TGS/Nopec
93	2052-LC	533946	576132	5041789	5041563	TGS/Nopec
94	2053-LC	534042	576336.889	5046085.026	5045863	TGS/Nopec
95	2054-LC	534141	576507.957	5064964	5064874	TGS/Nopec
96	2055-LC	533646	576020	5070976	5070910	TGS/Nopec
97	2056-LC	533433	575804.75	5084016	5083966.983	TGS/Nopec
98	2057-LC	533321	575690.745	5093850	5093827	TGS/Nopec
99	2058-LC	459788	592134.828	4953550	4953506	TGS/Nopec
100	2059-LC	534036	577157.017	4948333	4948292	TGS/Nopec
101	2060-LC	460359.662	576414	5010312	4946697.99	TGS/Nopec
102	2061-LC	541487	569868	5017166	4964226	TGS/Nopec
103	2062-LC	550798	565075.918	5004980	4966246.196	TGS/Nopec
104	98G10-01	486669.007	545310.554	5055323.075	5055179.075	ConocoPhillips
105	98G10-02	487515.007	545130.475	5048090.209	5047807.075	ConocoPhillips
106	98G10-03	487656.007	545205.008	5043722.075	5043316.075	ConocoPhillips

107	98G10-45	544830.008	545858.008	5102690.076	4898654.073	ConocoPhillips
108	98G10-46	542481.008	542751.008	5077690.076	4948451.074	ConocoPhillips
109	98G10-47A	540021.008	540637.008	5077634.076	4948297.074	ConocoPhillips
110	98G10-48	537387.008	537731.008	5077684.076	4975982.074	ConocoPhillips
111	98G10-49	534745.508	535417.008	5077611.076	4975915.074	ConocoPhillips
112	98G10-50	486530.007	545032.008	5059380.075	5059131.075	ConocoPhillips
113	98G10-51	486559.007	545110.008	5052167.075	5051777.075	ConocoPhillips
114	98G10-52	486503.007	544992.508	5039465.075	5039132.075	ConocoPhillips
115	98G10-57	529912.008	530276.008	5074997.451	5017006.075	ConocoPhillips
116	98G10-58	526116.008	526564.008	5077896.076	5016883.075	ConocoPhillips
117	98G10-59	522987.008	523227.008	5076261.576	5016948.075	ConocoPhillips
118	98G10-61	514167.008	514213.008	5077817.576	5016878.075	ConocoPhillips
119	98G10-62	509175.008	509235.008	5077698.076	5016882.075	ConocoPhillips
120	98G10-63	504592.008	504693.008	5077699.076	5017136.075	ConocoPhillips
121	STP-01	538146	599794	5100958	4932093	NRCAN
122	STP-02	471265.133	581354	4990159	4952997	NRCAN
123	STP-07a	547643	565269	4971074	4924665	NRCAN
124	STP-10	575453	601049	5058953	4962769	NRCAN
125	STP-11	591115	623896	5082958	4903804	NRCAN
126	STP-12	612197	619899	5050682	4979717	NRCAN
127	STP-13	626733	630955.45	5075586	4957339.664	NRCAN
128	STP-14	644031	644070	5058613	4986938	NRCAN
129	STP-15	657845.538	661984	5056869	4935482.686	NRCAN
130	STP-16	669206	688311	5057232	4993436	NRCAN
131	STP-17	673593	699950	5044495	4949042	NRCAN
132	STP-18	693133	708196	5033771	5008412	NRCAN
133	STP-19	556305	700622	5039483	5028711	NRCAN

134	STP-20	421836	568533	5026987	5026168	NRCAN
135	STP-21	448390	590856	5016542	4998373	NRCAN
136	STP-22	572623	708016	5014570	4987937	NRCAN
137	STP-23	550484.513	595337	4995096	4925809.524	NRCAN
138	STP-24	519906	529245	5067762	5031031	NRCAN
139	STP-25	529235	558304	5071520	5029104	NRCAN
140	STP-26	537450	559059	5060444	5017795	NRCAN
141	STP-27	561941	582025	5039630	4996751	NRCAN
142	STP-28	531360	548366	5039097	4998843	NRCAN
143	STP-29	539820	574338	5033629	5010962	NRCAN
144	STP-3	451867	517087	5080400	4906787	NRCAN
145	STP-4	468970	521644	5070580	4933686	NRCAN
146	STP-5	477622	563353	5081685	4870506.625	NRCAN
147	STP-6	493474.143	552990	5077305.429	4924040	NRCAN
148	STP-7B	504236.167	548007	5082639.417	4969457	NRCAN
149	STP-8	544333	568912.128	5008781	4950117.743	NRCAN
150	STP-9	545225	570486	5061304	5000438	NRCAN

Appendix 4

Detailed Processing Parameters for TGS/Nopec Seismic Data

TGS

CANADA
LC-105 & NS-103
NON-EXCLUSIVE 2-D SURVEY

ACQUISITION PARAMETERS

Acquisition Date:	May 2002-October 2002
Data Acquired By:	GSI, M/V Admiral
Recording Instrument:	I/O MSX
Filter settings:	Low: 2Hz – 6 dB/octave
	High: 206Hz – 264 dB/octave
Airgun Source Volume	5240 cubic inch
Gun Depth:	6 meters
Shotpoint Interval:	37.5 meters
Group Interval:	12.5 meters
Streamer type:	I/O MSX
Streamer Depth:	9 meters
Recording channels:	640
Streamer Length:	8000 meters
Record Length:	14336 ms
Sample Interval:	2 milliseconds
Nominal Fold:	106

PROCESSING SEQUENCE

- LC-105 Processing performed by Spectrum - Processing completed April 2003
- NS-103 Processing performed by TGS-NOPEC - Processing completed March 2003
- Resample 2ms to 4ms
- Edit bad traces and shots
- Merge seismic trace headers with navigation
- FK anti-alias filter and trace drop - 640 channels to 320 - output NAV-MERGE - *NS-103 only*
- 2:1 adjacent trace sum - 640 channels to 320 - output NAV-MERGE – *LC-105 only*
- Spherical divergence correction
- Deconvolution – single design gate, 280ms operator, 16ms gap
- Water velocity Radon
- Velocity analysis every 2km
- Primary velocity Radon- output RADON
- Migration velocity analysis every 1km
- Kirchhoff pre stack time migration- output PSTM-GATHERS
- Residual velocity analysis every 1km – output PSTM-GATHERS+NMO
- Stack - Output RAW MIG
- Filter and scaling - output PROC-MIG

AVAILABLE DELIVERABLES

- Raw field data/shot ordered
- Field data with navigation in trace headers/shot ordered
- Radon de-multiple CDP gathers
- Pre stack time migrated CDP gathers without NMO correction
- Pre stack time migrated CDP gathers with NMO correction
- Raw migration
- Processed migration
- Stacking velocities (ASCII)
- Migration velocities (ASCII)
- Processed source-receiver navigation – UKOOA
- Post stack navigation – UKOOA
- Workstation-ready tapes available in SMT, Landmark, and Geoquest

TGS

Laurentian Channel
NON-EXCLUSIVE 2-D CANADA SURVEY

ACQUISITION PARAMETERS

Acquisition Date:	**August 1999**
Data Acquired By:	**Geco-Prakla**
Kilometers:	**4,495.800 kilometers**
Shooting Orientation:	**North-South/East-West**
Recording Instrument:	**Nessie 3**
Streamer Type:	**Geco-Prakla Nessie 4**
Streamer Positioning:	**Compass / RGPS**
Airgun Source:	**7918 cubic inches**
Gun Depth:	**7.5 meters +/-1 meter**
Shotpoint Interval:	**37.5 meters**
Group Interval:	**25 meters**
Recording Channels:	**320**
Streamer Depth:	**9 meters +/-1.5 meters**
Streamer Length:	**8000 meters**
Record Length:	**14.336 seconds**
Sample Interval:	**2 milliseconds**
Nominal Fold:	**106**

PROCESSING SEQUENCE

- **Data processing performed by: CGG Canada Services Ltd.**
- **Processing completed January 2000**
- **Swell noise removal**
- **Spherical divergence correction**
- **Shot domain F-K filter**
- **Convert source signature to minimum phase equivalent**
- **Deconvolution – single gate, shot average, 250 ms operator, 4 ms gap**
- **Predictive deconvolution – 240 ms operator, 24 ms gap**
- **Trace to trace editing**
- **Resample to 4ms - record length 11000 ms**
- **Velocity analysis- 2000 m**
- **Radon demultiple – 0-3000 ms**
- **FK demultiple - 2000-11000 ms**
- **Wave equation modeling demultiple – on selected lines**
- **2D Kirchhoff DMO**
- **Velocity analysis - 500 m**
- **Spectral whitening**
- **Stack**
- **Peg leg multiple removal – on selected lines**
- **FX migration (steep dip)**
- **FX deconvolution and AGC**

AVAILABLE DELIVERABLES

- **Raw field data/shot ordered**
- **Raw stack**
- **Raw migration**
- **Processed stack**
- **Processed migration**
- **Stacking velocities (ASCII)**
- **Migration velocities (ASCII)**
- **Post stack navigation –UKOOA**
- **Workstation-ready tapes available in SMT, Landmark, and Geoquest**

Appendix 5 - Biostratigraphic Picks for Wells

Dauntless D-35

Year	Author	Journal	Top	Bottom	Units	Division	Age	Method
1995	WILLIAMS,G.L.	BAS-PAL-01-95GLW	313.95	380.4	M		(CANNOT DATE)	PALYNOLOGY
1995	WILLIAMS,G.L.	BAS-PAL-01-95GLW	414.53	414.53	M	MIDDLE	MIOCENE	PALYNOLOGY
1995	WILLIAMS,G.L.	BAS-PAL-01-95GLW	460.86	564.8	M	EARLY TO MIDDLE	MIOCENE	PALYNOLOGY
1995	WILLIAMS,G.L.	BAS-PAL-01-95GLW	620.58	752.87	M	EARLY	OLIGOCENE	PALYNOLOGY
1995	WILLIAMS,G.L.	BAS-PAL-01-95GLW	770.85	848.27	M	LATE	EOCENE	PALYNOLOGY
1995	WILLIAMS,G.L.	BAS-PAL-01-95GLW	963.18	972.32	M	EARLY	EOCENE	PALYNOLOGY
1995	WILLIAMS,G.L.	BAS-PAL-01-95GLW	1018.04	1277.74	M	LATE	PALEOCENE	PALYNOLOGY
1995	WILLIAMS,G.L.	BAS-PAL-01-95GLW	1292.37	1418.56	M	EARLY	PALEOCENE	PALYNOLOGY
1995	WILLIAMS,G.L.	BAS-PAL-01-95GLW	1470.98		M		MAASTRICHTIAN	PALYNOLOGY
1988	ASCOLI,P.	GSC OPEN FILE REPORT #1791	1566.69		M		CAMPANIAN	PLANKTONIC FORAMS
1988	ASCOLI,P.	GSC OPEN FILE REPORT #1791	1758.72		M		SANTONIAN	PLANKTONIC FORAMS
1988	ASCOLI,P.	GSC OPEN FILE REPORT #1791	1871.49		M		CONIACIAN	PLANKTONIC FORAMS
1988	ASCOLI,P.	GSC OPEN FILE REPORT #1791	1993.42		M		TURONIAN	PLANKTONIC FORAMS
1988	ASCOLI,P.	GSC OPEN FILE REPORT #1791	2023.9		M	LATE	CENOMANIAN	PLANKTONIC FORAMS
1988	ASCOLI,P.	GSC OPEN FILE REPORT #1791	2211.05		M	EARLY & MIDDLE	CENOMANIAN	PLANKTONIC FORAMS
1988	ASCOLI,P.	GSC OPEN FILE REPORT #1791	2267.74		M	LATE	ALBIAN	PLANKTONIC FORAMS
1988	ASCOLI,P.	GSC OPEN FILE REPORT #1791	2767.62		M	EARLY & MIDDLE	ALBIAN	CALC BENTH FORAMS
1988	ASCOLI,P.	GSC OPEN FILE REPORT #1791	2837.72		M		APTIAN	CALC BENTH FORAMS
1988	ASCOLI,P.	GSC OPEN FILE	3109		M		BARREMIAN	AREN BENTH

		REPORT #1791						FORAMS
1988	ASCOLI,P.	GSC OPEN FILE REPORT #1791	3291.88		M		HAUTERIVIAN	CALC BENTH FORAMS
1988	ASCOLI,P.	GSC OPEN FILE REPORT #1791	3624.12		M		BERRIASIAN-VALANGINIAN	CALC/AREN BENTH FORAMS
1988	ASCOLI,P.	GSC OPEN FILE REPORT #1791	3831.38		M		L OXFORDIAN-TITHONIAN	CALC BENTH FORAMS
1988	ASCOLI,P.	GSC OPEN FILE REPORT #1791	4572.06		M		OXFORDIAN	CALC BENTH FORAMS
1985	ASCOLI,P.	EPGS-PAL-02-85PA	3624	3831	M		BERRIASIAN-VALANGINIAN	CALC BENTH FORAMS

Hesper P-52

Year	Author	Journal	Top	Bottom	Units	Division	Age	Method
1990	ASCOLI,P.	BAS-PAL-02-90PA	2990	3670	M		HAUTERIVIAN-BARREMIAN (& BERRIASIAN-VALANGINIAN ? IN PART)	MICROPALEO
1990	ASCOLI,P.	BAS-PAL-02-90PA	3690	3890	M		TITHONIAN	MICROPALEO
1990	ASCOLI,P.	BAS-PAL-02-90PA	3910	4160	M		KIMMERIDGIAN	MICROPALEO
1990	ASCOLI,P.	BAS-PAL-02-90PA	4180	4520	M		OXFORDIAN	MICROPALEO
1990	ASCOLI,P.	BAS-PAL-02-90PA	4540	5679	M		OXFORDIAN ?	MICROPALEO
1987	NOVA/HUSKY RESEARCH CORP LTD	PALYNOLOGY REPORT	1260	1370	M		MAASTRICHTIAN	PALYNOLOGY
1987	NOVA/HUSKY RESEARCH CORP LTD	PALYNOLOGY REPORT	1370	1495	M		CAMPANIAN	PALYNOLOGY
1987	NOVA/HUSKY RESEARCH CORP LTD	PALYNOLOGY REPORT	1495	1650	M		CONIACIAN ?-SANTONIAN	PALYNOLOGY
1987	NOVA/HUSKY RESEARCH CORP LTD	PALYNOLOGY REPORT	1650	1660	M		TURONIAN (PROBABLE)	PALYNOLOGY
1987	NOVA/HUSKY RESEARCH CORP LTD	PALYNOLOGY REPORT	1660	1885	M		CENOMANIAN	PALYNOLOGY
1987	NOVA/HUSKY RESEARCH CORP LTD	PALYNOLOGY REPORT	1885	2340	M		ALBIAN	PALYNOLOGY
1987	NOVA/HUSKY RESEARCH CORP LTD	PALYNOLOGY REPORT	2340	2610	M		APTIAN	PALYNOLOGY
1987	NOVA/HUSKY RESEARCH CORP LTD	PALYNOLOGY REPORT	2610	2800	M	EARLY	APTIAN	PALYNOLOGY
1987	NOVA/HUSKY	PALYNOLOGY	2800	3080	M		HAUTERIVIAN-BARREMIAN	PALYNOLOGY

	RESEARCH CORP LTD	REPORT						
1987	NOVA/HUSKY RESEARCH CORP LTD	PALYNOLOGY REPORT	3080	3400	M		HAUTERIVIAN	PALYNOLOGY
1987	NOVA/HUSKY RESEARCH CORP LTD	PALYNOLOGY REPORT	3400	3690	M		BERRIASIAN-VALANGINIAN	PALYNOLOGY
1987	NOVA/HUSKY RESEARCH CORP LTD	PALYNOLOGY REPORT	3690	4000	M		KIMMERIDGIAN-PORTLANDIAN	PALYNOLOGY
1987	NOVA/HUSKY RESEARCH CORP LTD	PALYNOLOGY REPORT	4000	4500	M	EARLY	KIMMERIDGIAN	PALYNOLOGY
1987	NOVA/HUSKY RESEARCH CORP LTD	PALYNOLOGY REPORT	4500	4875	M		OXFORDIAN	PALYNOLOGY
1987	NOVA/HUSKY RESEARCH CORP LTD	PALYNOLOGY REPORT	4875	5200	M		CALLOVIAN	PALYNOLOGY
1987	NOVA/HUSKY RESEARCH CORP LTD	PALYNOLOGY REPORT	5200	5600	M		BATHONIAN	PALYNOLOGY
1987	NOVA/HUSKY RESEARCH CORP LTD	PALYNOLOGY REPORT	5600	5679	M		BAJOCIAN ?	PALYNOLOGY
1987	NOVA/HUSKY RESEARCH CORP LTD	PALYNOLOGY REPORT		1260	M		PALEOCENE-EOCENE	PALYNOLOGY

Sachem D-76

Year	Author	Journal	Top	Bottom	Units	Division	Age
2005	ASCOLI,P.	M.R.G.-PAL-02-2005PA	1379.54	1405.15	M		MAASTRICHTIAN
2005	ASCOLI,P.	M.R.G.-PAL-02-2005PA	1417.34	1591.08	M		CAMPANIAN
2005	ASCOLI,P.	M.R.G.-PAL-02-2005PA	1609.36	1700.8	M		SANTONIAN
2005	ASCOLI,P.	M.R.G.-PAL-02-2005PA	1719.09	1758.72	M		CONIACIAN
2005	ASCOLI,P.	M.R.G.-PAL-02-2005PA	1773.35	1874.54	M	LATE	CENOMANIAN
2005	ASCOLI,P.	M.R.G.-PAL-02-2005PA	1883.69	2688.37	M		L ALBIAN-E CENOMANIAN
2005	ASCOLI,P.	M.R.G.-PAL-02-2005PA	2715.8	2926.12	M	EARLY-MIDDLE	ALBIAN
2005	ASCOLI,P.	M.R.G.-PAL-02-2005PA	2944.4	3182.15	M		APTIAN
2005	ASCOLI,P.	M.R.G.-PAL-02-2005PA	3200.44	3438.19	M		BARREMIAN
2005	ASCOLI,P.	M.R.G.-PAL-02-2005PA	3456.47	3602.78	M		HAUTERIVIAN
2005	ASCOLI,P.	M.R.G.-PAL-02-2005PA	3621.07	3739.94	M		BERRIASIAN-VALANGINIAN
2005	ASCOLI,P.	M.R.G.-PAL-02-2005PA	3758.23	3931.97	M		L KIMMERIDGIAN-TITHONIAN
2005	ASCOLI,P.	M.R.G.-PAL-02-2005PA	3950.26	4206.29	M		L OXFORDIAN-E KIMMERIDGIAN
2005	ASCOLI,P.	M.R.G.-PAL-02-2005PA	4224.58	4562.91	M	EARLY-MIDDLE	OXFORDIAN
2005	ASCOLI,P.	M.R.G.-PAL-02-2005PA	4581.2	4876.86	M		CALLOVIAN
1980	DOEVEN,P.	EPGS-PAL-41-80PD	1734.33	1734.33	M	EARLY	SANTONIAN
1980	DOEVEN,P.	EPGS-PAL-41-80PD	1758.72	1758.72	M		CONIACIAN-E SANTONIAN
1980	DOEVEN,P.	EPGS-PAL-41-80PD	1768.47	1768.47	M		CONIACIAN
1980	DOEVEN,P.	EPGS-PAL-41-80PD	1773.35	1773.35	M	LATE	CENOMANIAN
1980	DOEVEN,P.	EPGS-PAL-41-80PD	1786.76	1786.76	M		(EARLY PART OF) L CENOMANIAN
1980	DOEVEN,P.	EPGS-PAL-41-80PD	1835.53	1835.53	M	EARLY	CENOMANIAN
1976	MOBIL OIL CANADA	PALEONTOLOGICAL SUMMARY	0	475.49	M		PLIOCENE-PLEISTOCENE TO RECENT
1976	MOBIL OIL CANADA	PALEONTOLOGICAL SUMMARY	475.49	658.38	M		MIOCENE-PLIOCENE
1976	MOBIL OIL CANADA	PALEONTOLOGICAL SUMMARY	658.38	808.95	M	LATE	MIOCENE
1976	MOBIL OIL	PALEONTOLOGICAL	808.95	918.98	M	MIDDLE	MIOCENE

	CANADA	SUMMARY					
1976	MOBIL OIL CANADA	PALEONTOLOGICAL SUMMARY	918.98	1371.62	M		PALEOCENE
1976	MOBIL OIL CANADA	PALEONTOLOGICAL SUMMARY	1371.62	1426.48	M		MAASTRICHTIAN
1976	MOBIL OIL CANADA	PALEONTOLOGICAL SUMMARY	1426.48	1627.65	M		CAMPANIAN
1976	MOBIL OIL CANADA	PALEONTOLOGICAL SUMMARY	1627.65	1734.33	M		SANTONIAN
1976	MOBIL OIL CANADA	PALEONTOLOGICAL SUMMARY	1734.33	1773.35	M		CONIACIAN
1976	MOBIL OIL CANADA	PALEONTOLOGICAL SUMMARY	1773.35	2072.67	M		CENOMANIAN
1976	MOBIL OIL CANADA	PALEONTOLOGICAL SUMMARY	2072.67	3063.28	M		ALBIAN
1976	MOBIL OIL CANADA	PALEONTOLOGICAL SUMMARY	3063.28	3208.06	M		APTIAN
1976	MOBIL OIL CANADA	PALEONTOLOGICAL SUMMARY	3208.06	3352.84	M		BARREMIAN (PROBABLE)
1976	MOBIL OIL CANADA	PALEONTOLOGICAL SUMMARY	3352.84		M		HAUTERIVIAN (PROBABLE)
1976	MOBIL OIL CANADA	PALEONTOLOGICAL SUMMARY	3758.23		M		TITHONIAN-BERRIASIAN
1976	MOBIL OIL CANADA	PALEONTOLOGICAL SUMMARY	4486.71	4876.86	M		OXFORDIAN
1976	MOBIL OIL CANADA	PALYNOLOGY SUMMARY	274.32	1005.85	M		CENOZOIC (PROBABLE NEOGENE)
1976	MOBIL OIL CANADA	PALYNOLOGY SUMMARY	1005.85	1371.62	M		PALEOCENE
1976	MOBIL OIL CANADA	PALYNOLOGY SUMMARY	1371.62	1706.9	M		CAMPANIAN
1976	MOBIL OIL CANADA	PALYNOLOGY SUMMARY	1706.9	1767.86	M		SANTONIAN (LOWER PART POSSIBLE L CONIACIAN)
1976	MOBIL OIL CANADA	PALYNOLOGY SUMMARY	1767.86	1828.82	M		TURONIAN-CONIACIAN
1976	MOBIL OIL	PALYNOLOGY	1828.82	2072.67	M		CENOMANIAN

	CANADA	SUMMARY					
1976	MOBIL OIL CANADA	PALYNOLOGY SUMMARY	2072.67	2956.6	M		ALBIAN
1976	MOBIL OIL CANADA	PALYNOLOGY SUMMARY	2956.6	3261.4	M		APTIAN
1976	MOBIL OIL CANADA	PALYNOLOGY SUMMARY	3261.4	3383.32	M		BARREMIAN
1976	MOBIL OIL CANADA	PALYNOLOGY SUMMARY	3383.32	3566.2	M		HAUTERIVIAN
1976	MOBIL OIL CANADA	PALYNOLOGY SUMMARY	3566.2	3901.49	M		BERRIASIAN-VALANGINIAN
1976	MOBIL OIL CANADA	PALYNOLOGY SUMMARY	3901.49	4297.73	M		KIMMERIDGIAN (TITHONIAN ? IN UPPER PART)
1976	MOBIL OIL CANADA	PALYNOLOGY SUMMARY	4297.73	4876.86	M		OXFORDIAN

Hermine E-94

Year	Author	Journal	Top	Bottom	Units	Division	Age	Method
2006	WILLIAMS,G.L.	GSC OPEN FILE REPORT #4976	341.38	435.86	M	LATE	MIOCENE	PALYNOLOGY
2006	WILLIAMS,G.L.	GSC OPEN FILE REPORT #4976	441.96	463.3	M	MID	MIOCENE (SERRAVALLIAN)	PALYNOLOGY
2006	WILLIAMS,G.L.	GSC OPEN FILE REPORT #4976	469.39	545.59	M	EARLY	OLIGOCENE (RUPELIAN)	PALYNOLOGY
2006	WILLIAMS,G.L.	GSC OPEN FILE REPORT #4976	551.69	563.88	M	LATE	EOCENE (PRIABONIAN)	PALYNOLOGY
2006	WILLIAMS,G.L.	GSC OPEN FILE REPORT #4976	569.98	600.46	M	MIDDLE	EOCENE (BARTONIAN)	PALYNOLOGY
2006	WILLIAMS,G.L.	GSC OPEN FILE REPORT #4976	606.55	691.9	M	MIDDLE	EOCENE (LATE LUTETIAN)	PALYNOLOGY
2006	WILLIAMS,G.L.	GSC OPEN FILE REPORT #4976	710.19	792.48	M	MIDDLE	EOCENE (EARLY LUTETIAN)	PALYNOLOGY
2006	WILLIAMS,G.L.	GSC OPEN FILE REPORT #4976	801.63	829.06	M	EARLY	EOCENE (LATE YPRESIAN)	PALYNOLOGY
2006	WILLIAMS,G.L.	GSC OPEN FILE REPORT #4976	829.06	847.35	M	EARLY	EOCENE (EARLY YPRESIAN)	PALYNOLOGY
2006	WILLIAMS,G.L.	GSC OPEN FILE REPORT #4976	847.35	911.35	M		(AGE NOT DETERMINED)	PALYNOLOGY
2006	WILLIAMS,G.L.	GSC OPEN FILE REPORT #4976	920.5	1002.79	M		MAASTRICHTIAN	PALYNOLOGY
2006	WILLIAMS,G.L.	GSC OPEN FILE REPORT #4976	1014.99	1060.71	M	LATE	CAMPANIAN	PALYNOLOGY
2006	WILLIAMS,G.L.	GSC OPEN FILE REPORT #4976	1069.85	1133.86	M	EARLY	CAMPANIAN	PALYNOLOGY
2006	WILLIAMS,G.L.	GSC OPEN FILE REPORT #4976	1143	1188.72	M		SANTONIAN	PALYNOLOGY
2006	WILLIAMS,G.L.	GSC OPEN FILE REPORT #4976	1197.87	1252.73	M		TURONIAN-CONIACIAN	PALYNOLOGY
2006	WILLIAMS,G.L.	GSC OPEN FILE REPORT #4976	1261.87	1283.21	M		CENOMANIAN	PALYNOLOGY
2006	WILLIAMS,G.L.	GSC OPEN FILE REPORT #4976	1289.31	1313.69	M	LATE	ALBIAN	PALYNOLOGY
2006	WILLIAMS,G.L.	GSC OPEN FILE REPORT #4976	1316.74	1420.37	M	EARLY TO MIDDLE	ALBIAN	PALYNOLOGY
2006	WILLIAMS,G.L.	GSC OPEN FILE REPORT #4976	1426.47	1542.29	M		APTIAN	PALYNOLOGY
2006	WILLIAMS,G.L.	GSC OPEN FILE REPORT #4976	1548.39	1642.88	M		BARREMIAN	PALYNOLOGY
2006	WILLIAMS,G.L.	GSC OPEN FILE REPORT #4976	1652.02		M		PENNSYLVANIAN (WESTPHALIAN)	PALYNOLOGY

2006	WILLIAMS,G.L.	GSC OPEN FILE REPORT #4976	2386.58	3261.36	M		PALEOZOIC	PALYNOLOGY
2006	WILLIAMS,G.L.	GSC OPEN FILE REPORT #4976		2346.96	M		MISSISSIPPIAN (L VISEAN TO NAMURIAN)	PALYNOLOGY
2004	THOMAS, F.C.	M.R.G.-PAL.5-2004FCT	119.79	146.61	M		PLEISTOCENE	MICROPALEO
2004	THOMAS, F.C.	M.R.G.-PAL.5-2004FCT	146.61	344.43	M		(INDETERMINATE)	MICROPALEO
2004	THOMAS, F.C.	M.R.G.-PAL.5-2004FCT	362.72	371.86	M		PLIOCENE ?	MICROPALEO
2004	THOMAS, F.C.	M.R.G.-PAL.5-2004FCT	390.15	719.34	M		(INDETERMINATE)	MICROPALEO
2004	THOMAS, F.C.	M.R.G.-PAL.5-2004FCT	728.48	819.92	M		EOCENE	MICROPALEO
2004	THOMAS, F.C.	M.R.G.-PAL.5-2004FCT	838.21	847.35	M	EARLY	EOCENE	MICROPALEO
2004	THOMAS, F.C.	M.R.G.-PAL.5-2004FCT	865.64	957.08	M		MAASTRICHTIAN	MICROPALEO
2004	THOMAS, F.C.	M.R.G.-PAL.5-2004FCT	975.37	1042.43	M		CAMPANIAN	MICROPALEO
2004	THOMAS, F.C.	M.R.G.-PAL.5-2004FCT	1060.72	1356.38	M		CONIACIAN-SANTONIAN	MICROPALEO
2004	THOMAS, F.C.	M.R.G.-PAL.5-2004FCT	1374.66	1383.81	M		CENOMANIAN ?-E TURONIAN	MICROPALEO
2004	THOMAS, F.C.	M.R.G.-PAL.5-2004FCT	1402.1	1566.69	M		ALBIAN ?	MICROPALEO
2004	THOMAS, F.C.	M.R.G.-PAL.5-2004FCT	1584.98	1588.03	M		BERRIASIAN ?-VALANGINIAN	MICROPALEO
2004	THOMAS, F.C.	M.R.G.-PAL.5-2004FCT	1615.46	3267.5	M		(INDETERMINATE)	MICROPALEO
2003	WILLIAMS,G.L.	GSC OPEN FILE REPORT #1654	341.38	435.87	M	LATE	MIOCENE	PALYNOLOGY
2003	WILLIAMS,G.L.	GSC OPEN FILE REPORT #1654	441.97	463.3	M	MID	MIOCENE (SERRAVALLIAN)	PALYNOLOGY
2003	WILLIAMS,G.L.	GSC OPEN FILE REPORT #1654	469.4	545.6	M	EARLY	OLIGOCENE (RUPELIAN)	PALYNOLOGY
2003	WILLIAMS,G.L.	GSC OPEN FILE REPORT #1654	551.69	563.89	M	LATE	EOCENE (PRIABONIAN)	PALYNOLOGY
2003	WILLIAMS,G.L.	GSC OPEN FILE REPORT #1654	569.98	600.46	M	MIDDLE	EOCENE (BARTONIAN)	PALYNOLOGY
2003	WILLIAMS,G.L.	GSC OPEN FILE REPORT #1654	606.56	664.47	M	MIDDLE	EOCENE (LUTETIAN)	PALYNOLOGY
1990	WILLIAMS,G.L. ET AL	GEOL OF THE CONT. MARGIN OF E CANADA NO. 2 CHAPTER 3	1767.8	1777	M		PENNSYLVANIAN (E WESTPHALIAN C)	PALYNOLOGY
1990	WILLIAMS,G.L. ET AL	GEOL OF THE CONT. MARGIN OF E CANADA NO. 2 CHAPTER 3	1770	2325.6	M		MISSISSIPPIAN (VISEAN-E NAMURIAN)	PALYNOLOGY
1980	THOMAS,F.C.	EPGS-PAL-02-80FCT			M		(QUALITATIVE)	MICROPALEO

Emerillion C-56

Year	Author	Journal	Top	Bottom	Units	Division	Age	Method
1993	FORD,J.H. (FORD BIOSTRATIGRAPHIC SERVICES)	HIGH RESOLUTION PALYNOLOGICAL ANALYSIS	1240.55	1338.09	M		SANTONIAN	PALYNOLOGY
1993	FORD,J.H. (FORD BIOSTRATIGRAPHIC SERVICES)	HIGH RESOLUTION PALYNOLOGICAL ANALYSIS	1338.09	1563.64	M		(INDETERMINATE)	PALYNOLOGY
1993	FORD,J.H. (FORD BIOSTRATIGRAPHIC SERVICES)	HIGH RESOLUTION PALYNOLOGICAL ANALYSIS	1563.64	1588.03	M		CONIACIAN	PALYNOLOGY
1993	FORD,J.H. (FORD BIOSTRATIGRAPHIC SERVICES)	HIGH RESOLUTION PALYNOLOGICAL ANALYSIS	1588.03	1661.18	M		TURONIAN	PALYNOLOGY
1993	FORD,J.H. (FORD BIOSTRATIGRAPHIC SERVICES)	HIGH RESOLUTION PALYNOLOGICAL ANALYSIS	1661.18	1734.33	M		CENOMANIAN	PALYNOLOGY
1993	FORD,J.H. (FORD BIOSTRATIGRAPHIC SERVICES)	HIGH RESOLUTION PALYNOLOGICAL ANALYSIS	1734.33	1844.06	M		ALBIAN	PALYNOLOGY
1993	FORD,J.H. (FORD BIOSTRATIGRAPHIC SERVICES)	HIGH RESOLUTION PALYNOLOGICAL ANALYSIS	1844.06	1935.5	M		APTIAN	PALYNOLOGY
1993	FORD,J.H. (FORD BIOSTRATIGRAPHIC SERVICES)	HIGH RESOLUTION PALYNOLOGICAL ANALYSIS	1935.5	2087.91	M		BARREMIAN	PALYNOLOGY
1993	FORD,J.H. (FORD BIOSTRATIGRAPHIC SERVICES)	HIGH RESOLUTION PALYNOLOGICAL ANALYSIS	2087.91	2118.39	M		BATHONIAN AND/OR CALLOVIAN	PALYNOLOGY
1993	FORD,J.H. (FORD BIOSTRATIGRAPHIC SERVICES)	HIGH RESOLUTION PALYNOLOGICAL ANALYSIS	2118.39	2392.71	M		BATHONIAN	PALYNOLOGY
1993	FORD,J.H. (FORD BIOSTRATIGRAPHIC SERVICES)	HIGH RESOLUTION PALYNOLOGICAL ANALYSIS	2392.71	2563.4	M		AALENIAN & BAJOCIAN	PALYNOLOGY

1993	FORD,J.H. (FORD BIOSTRATIGRAPHIC SERVICES)	HIGH RESOLUTION PALYNOLOGICAL ANALYSIS	2563.4	3152.28	M		L PLIENSBACHIAN TO TOARCIAN	PALYNOLOGY
1993	FORD,J.H. (FORD BIOSTRATIGRAPHIC SERVICES)	HIGH RESOLUTION PALYNOLOGICAL ANALYSIS	3152.28	3276.64	M	EARLY ?	JURASSIC ?	PALYNOLOGY
1990	ASCOLI,P.	BULL.CAN.PET.GEOL. V.38 NO.4 P.485-492			M		(SEE GSC OPEN FILE #1791)	MICROPALEO
1988	ASCOLI,P.	EPGS-PAL-02-88PA	1139.97	1499.63	M		N/A	MICROPALEO
1988	ASCOLI,P.	EPGS-PAL-02-88PA	1499.63	1652.04	M		N/A	MICROPALEO
1988	ASCOLI,P.	EPGS-PAL-02-88PA	1652.04	1743.48	M		N/A	MICROPALEO
1988	ASCOLI,P.	EPGS-PAL-02-88PA	1743.48	2109.24	M		N/A	MICROPALEO
1988	ASCOLI,P.	EPGS-PAL-02-88PA	2109.24	2475.01	M		N/A	MICROPALEO
1988	ASCOLI,P.	EPGS-PAL-02-88PA	2475.01	2880.4	M		N/A	MICROPALEO
1988	ASCOLI,P.	GSC OPEN FILE REPORT #1791	1139.97	1167.4	M		MAASTRICHTIAN	PLANKTONIC FORAMS
1988	ASCOLI,P.	GSC OPEN FILE REPORT #1791	1185.69	1264.94	M		CAMPANIAN	PLANKTONIC FORAMS
1988	ASCOLI,P.	GSC OPEN FILE REPORT #1791	1283.22	1420.39	M		SANTONIAN	PLANKTONIC FORAMS
1988	ASCOLI,P.	GSC OPEN FILE REPORT #1791	1438.67	1481.35	M		CONIACIAN	PLANKTONIC FORAMS
1988	ASCOLI,P.	GSC OPEN FILE REPORT #1791	1499.63	1630.7	M		TURONIAN	PLANK/CALC BENTH FORAM
1988	ASCOLI,P.	GSC OPEN FILE REPORT #1791	1652.04	1722.14	M		CENOMANIAN	PLANKTONIC FORAMS
1988	ASCOLI,P.	GSC OPEN FILE REPORT #1791	1743.48	1935.5	M		L APTIAN-ALBIAN	PLANK/CALC BENTH FORAM
1988	ASCOLI,P.	GSC OPEN FILE REPORT #1791	1956.84	1965.98	M	EARLY	APTIAN	CALC BENTH FORAMS
1988	ASCOLI,P.	GSC OPEN FILE REPORT #1791	1987.32	2087.91	M		BARREMIAN	OSTRACODS

1988	ASCOLI,P.	GSC OPEN FILE REPORT #1791	2087.91	2087.91	M		(UNCONFORMITY)	MICROPALEO
1988	ASCOLI,P.	GSC OPEN FILE REPORT #1791	2109.24	2453.67	M		CALLOVIAN-E OXFORDIAN	CALC BENTH FORAM/OSTRA
1988	ASCOLI,P.	GSC OPEN FILE REPORT #1791	2475.01	2880.4	M		BATHONIAN	OSTRACODS
1986	ASCOLI,P.	EPGS-PAL-01-86PA	1130.82	1139.97	M		PALEOCENE-E EOCENE (PARS)	MICROPALEO
1986	ASCOLI,P.	EPGS-PAL-01-86PA	1139.97	1167.4	M		MAASTRICHTIAN	MICROPALEO
1986	ASCOLI,P.	EPGS-PAL-01-86PA	1185.69	1264.94	M		CAMPANIAN	MICROPALEO
1986	ASCOLI,P.	EPGS-PAL-01-86PA	1283.22	1420.39	M		SANTONIAN	MICROPALEO
1986	ASCOLI,P.	EPGS-PAL-01-86PA	1438.67	1481.35	M		CONIACIAN	MICROPALEO
1986	ASCOLI,P.	EPGS-PAL-01-86PA	1499.63	1630.7	M		TURONIAN	MICROPALEO
1986	ASCOLI,P.	EPGS-PAL-01-86PA	1652.04	1722.14	M		CENOMANIAN	MICROPALEO
1986	ASCOLI,P.	EPGS-PAL-01-86PA	1743.48	1935.5	M		L APTIAN-ALBIAN	MICROPALEO
1986	ASCOLI,P.	EPGS-PAL-01-86PA	1956.84	1965.98	M	EARLY	APTIAN	MICROPALEO
1986	ASCOLI,P.	EPGS-PAL-01-86PA	1987.32	2087.91	M		BARREMIAN	MICROPALEO
1986	ASCOLI,P.	EPGS-PAL-01-86PA	2109.24	2453.67	M		CALLOVIAN-E OXFORDIAN	MICROPALEO
1986	ASCOLI,P.	EPGS-PAL-01-86PA	2475.01	2880.4	M		BATHONIAN	MICROPALEO
1986	ASCOLI,P.	EPGS-PAL-01-86PA	2901.73	3063.28	M		BAJOCIAN	MICROPALEO
1986	ASCOLI,P.	EPGS-PAL-01-86PA	3084.61	3240.06	M		BAJOCIAN ?	MICROPALEO
1986	ASCOLI,P.	EPGS-PAL-01-86PA	3267.5	3276.64	M	EARLY	JURASSIC (SINEMURIAN ?)	MICROPALEO
1981	ASCOLI,P.	EPGS-PAL-21-81PA	1240.55	1264.94	M		CAMPANIAN	MICROPALEO
1981	ASCOLI,P.	EPGS-PAL-21-81PA	1283.22	1420.39	M		SANTONIAN	MICROPALEO
1981	ASCOLI,P.	EPGS-PAL-21-81PA	1438.67	1481.35	M		CONIACIAN	MICROPALEO
1981	ASCOLI,P.	EPGS-PAL-21-81PA	1499.63	1630.7	M		TURONIAN	MICROPALEO
1981	ASCOLI,P.	EPGS-PAL-21-81PA	1652.04	1722.14	M		CENOMANIAN	MICROPALEO
1981	ASCOLI,P.	EPGS-PAL-21-81PA	1743.48	1935.5	M		L APTIAN-ALBIAN	MICROPALEO
1981	ASCOLI,P.	EPGS-PAL-21-81PA	1956.84	1965.98	M	EARLY	APTIAN	MICROPALEO
1981	ASCOLI,P.	EPGS-PAL-21-81PA	1987.32	2087.91	M		BARREMIAN	MICROPALEO

1981	ASCOLI,P.	EPGS-PAL-21-81PA	2109.24	2453.67	M		CALLOVIAN-E OXFORDIAN	MICROPALEO
1981	ASCOLI,P.	EPGS-PAL-21-81PA	2475.01	2880.4	M		BATHONIAN	MICROPALEO
1981	ASCOLI,P.	EPGS-PAL-21-81PA	2901.73	3063.28	M		BAJOCIAN	MICROPALEO
1981	ASCOLI,P.	EPGS-PAL-21-81PA	3084.61	3240.06	M		BAJOCIAN ?	MICROPALEO
1981	ASCOLI,P.	EPGS-PAL-21-81PA	3267.5	3276.64	M	EARLY	JURASSIC	MICROPALEO

Appendix 6 - Time to Depth Tables for Wells

Dauntless D-35

TWT (s)	Depth (m)		TWT (s)	Depth (m)
0.508	457.2000		2.084	2530.4496
0.51	457.2000		2.08	2530.4496
0.902	853.4400		2.198	2743.2000
0.904	853.4400		2.206	2743.2000
0.95	914.4000		2.188	2743.2000
0.952	914.4000		2.364	3048.0000
1.014	991.2096		2.368	3048.0000
1.206	1219.2000		2.474	3276.6000
1.208	1219.2000		2.476	3276.6000
1.204	1219.2000		2.626	3657.6000
1.386	1429.5120		2.628	3657.6000
1.384	1429.5120		2.718	3855.7200
1.38	1429.5120		2.718	3855.7200
1.396	1429.5120		2.822	4114.8000
1.452	1524.0000		2.814	4114.8000
1.452	1524.0000		2.884	4267.2000
1.44	1524.0000		2.878	4267.2000
1.636	1828.8000		3.03	4663.4400
1.64	1828.8000		3.032	4663.4400
1.63	1828.8000			
1.73	1975.1040			
1.73	1975.1040			
1.838	2133.6000			
1.84	2133.6000			
1.966	2339.3400			
1.966	2339.3400			
2.024	2438.4000			
2.026	2438.4000			
2.018	2438.4000			

Hesper P-52

TWT (s)	Depth (m)
0	40.5
0.296	316.649
0.475	475.45
0.6384	628.764
0.7852	771.106
0.9286	928.078
1.0562	1077.43
1.1904	1229.83
1.26	1261.5
1.2966	1383.754
1.3928	1534.63
1.495	1687.03
1.601	1839.43
1.7052	1991.83
1.8032	2144.229
1.8914	2296.63
1.9814	2449.03
2.0634	2601.43
2.1434	2753.83
2.1812	2807.17
2.365	3063.5
2.58	3599.5

Sachem D-76

TWT (s)	Depth (m)
0	29.9
0.0766	88.422
0.2614	235.335
0.4232	399.927
0.55	534.954
0.72	701.07
0.944	914.43
1.13	1127.79
1.3516	1380.774
1.4798	1584.99
1.6096	1767.87
1.7598	1981.23
1.8898	2194.59
2.0034	2377.469
2.1284	2590.83
2.2508	2807.238
2.3414	2974.877
2.5148	3322.35
2.64	3581.429
2.744	3817.649
2.82	3971.573
2.9408	4267.229
3.0586	4572.029

Hermine E-94

TWT (s)	Depth (m)
0	26
0.555	482
0.89	847
1.195	1242
1.43	1635
1.78	2406
1.9	2726
2.16	3293

Emerillion C-56

TWT (s)	Depth (m)
0	30
0.74	690
1.16	1156
1.48	1580
1.8	2088
2.324	3307

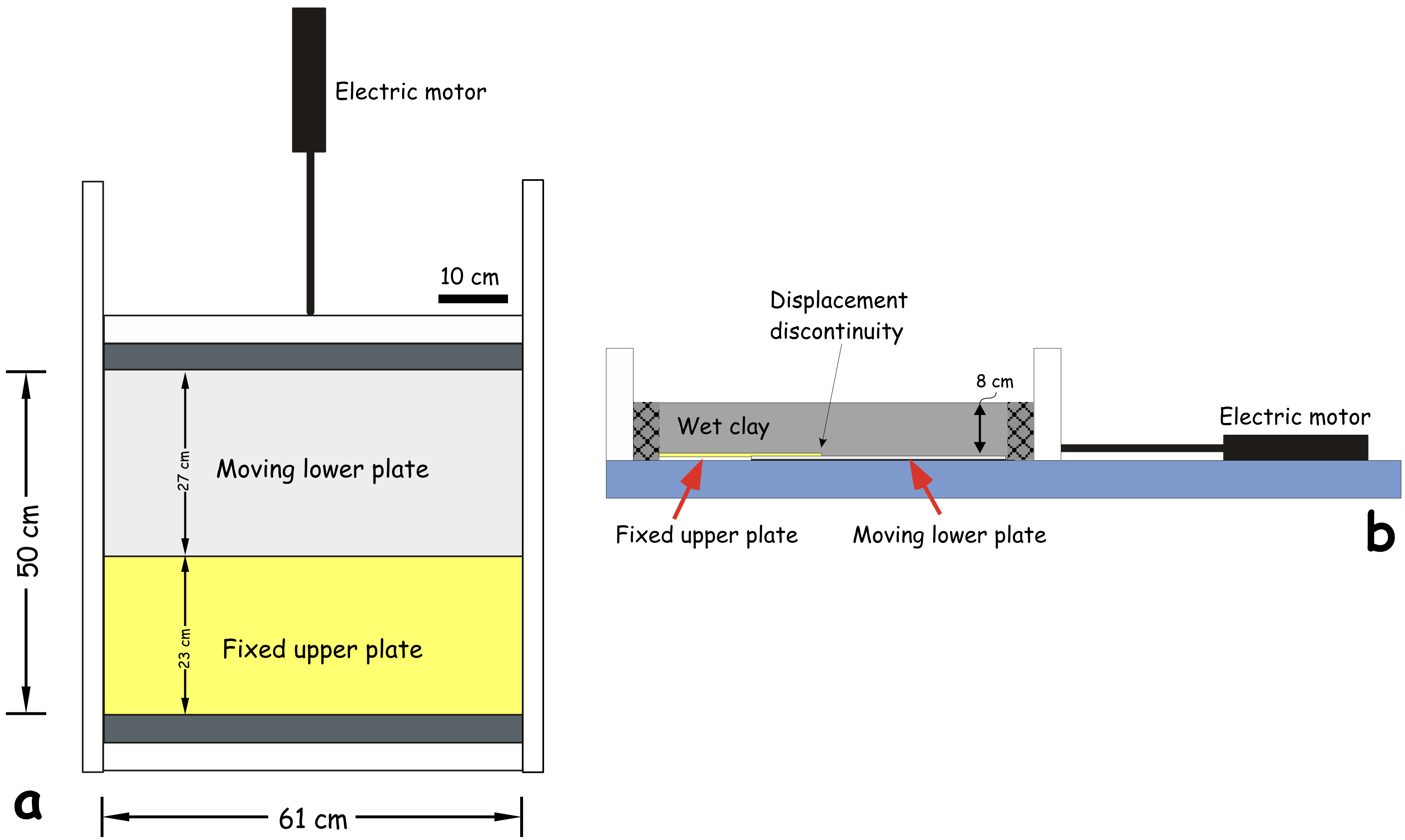

Figure 2.1. Experimental apparatus. **a)** Scaled map-view drawing of modeling apparatus. **b)** *Cross-sectional view of apparatus*. Note that model is 8-cm thick at the start of the first phase.

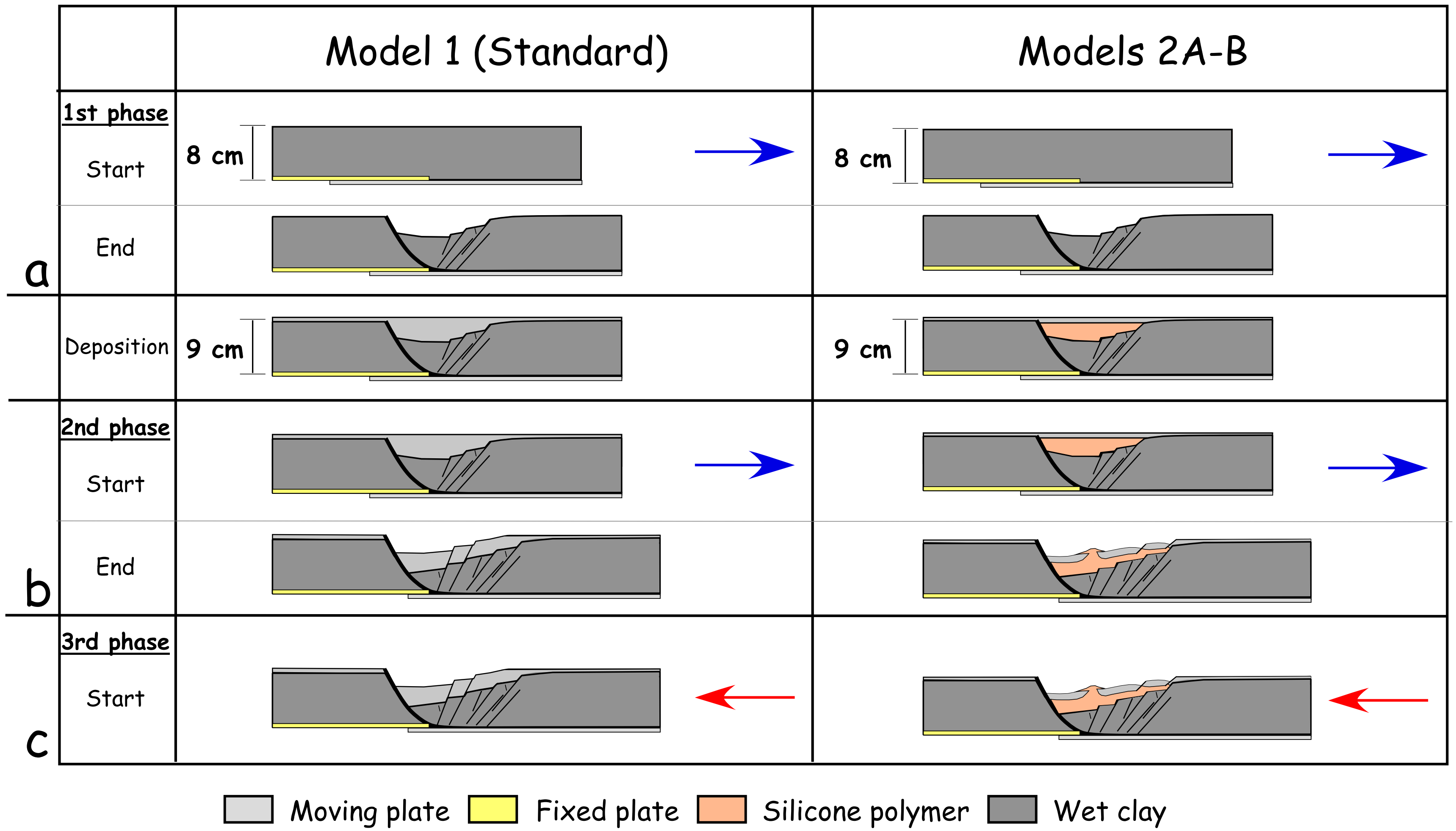

Figure 2.2. Schematic cross-sectional views of experimental setup. Arrows indicate displacement direction of moving plate. See text for detailed description of model setup.

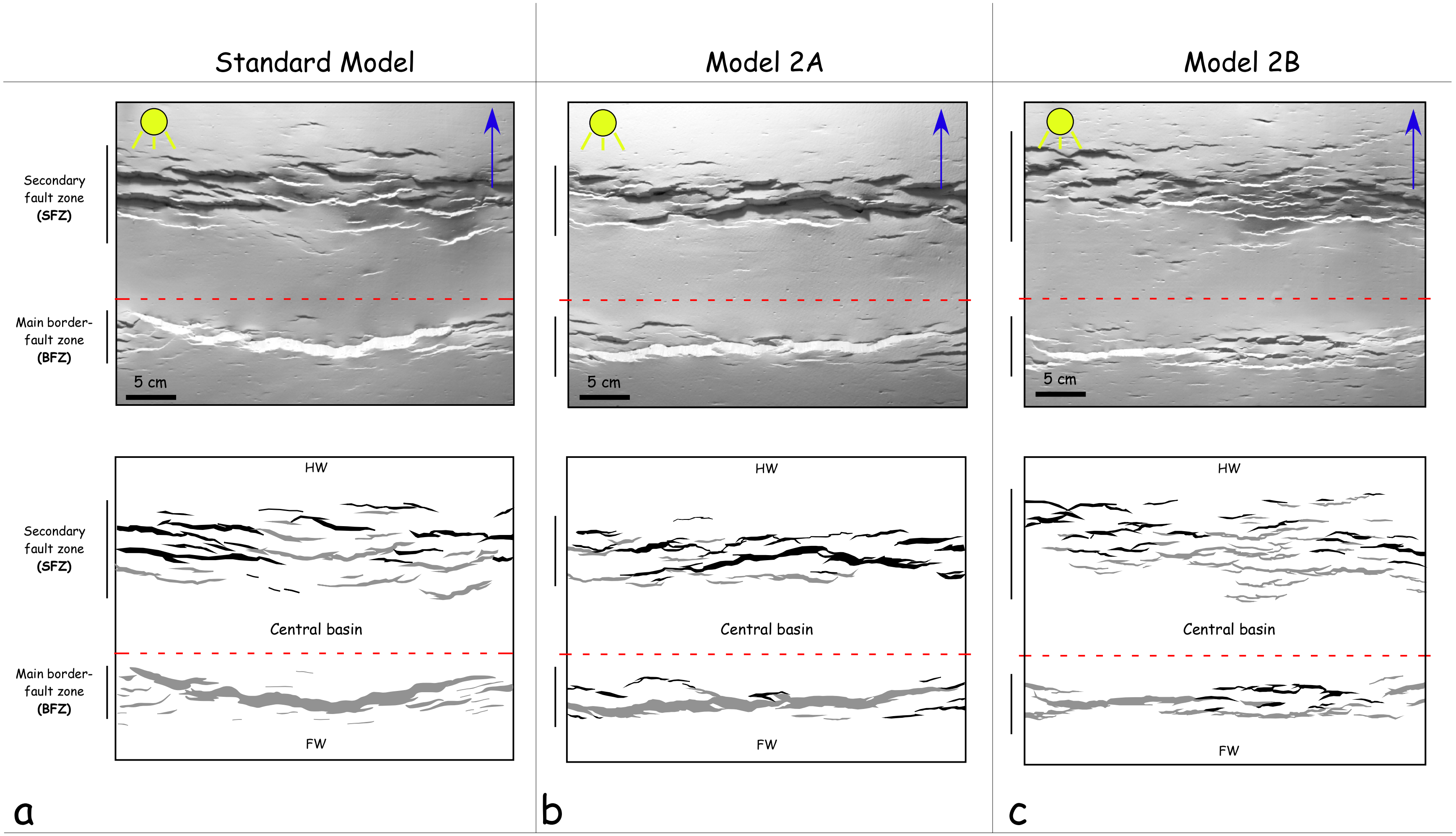

Figure 2.3. End phase 1. a) Standard Model; b) Model 2A; c) Model 2B. **top.** Photograph of model surface after 5 cm of extension. **bottom.** Line-drawing of model surface. Note red dashed line shows edge of fixed plate. Blue arrow shows displacement direction of moving plate. Grey faults dip towards moving wall; black faults dip away from moving wall. HW=hanging-wall of BFZ; FW=footwall of BFZ

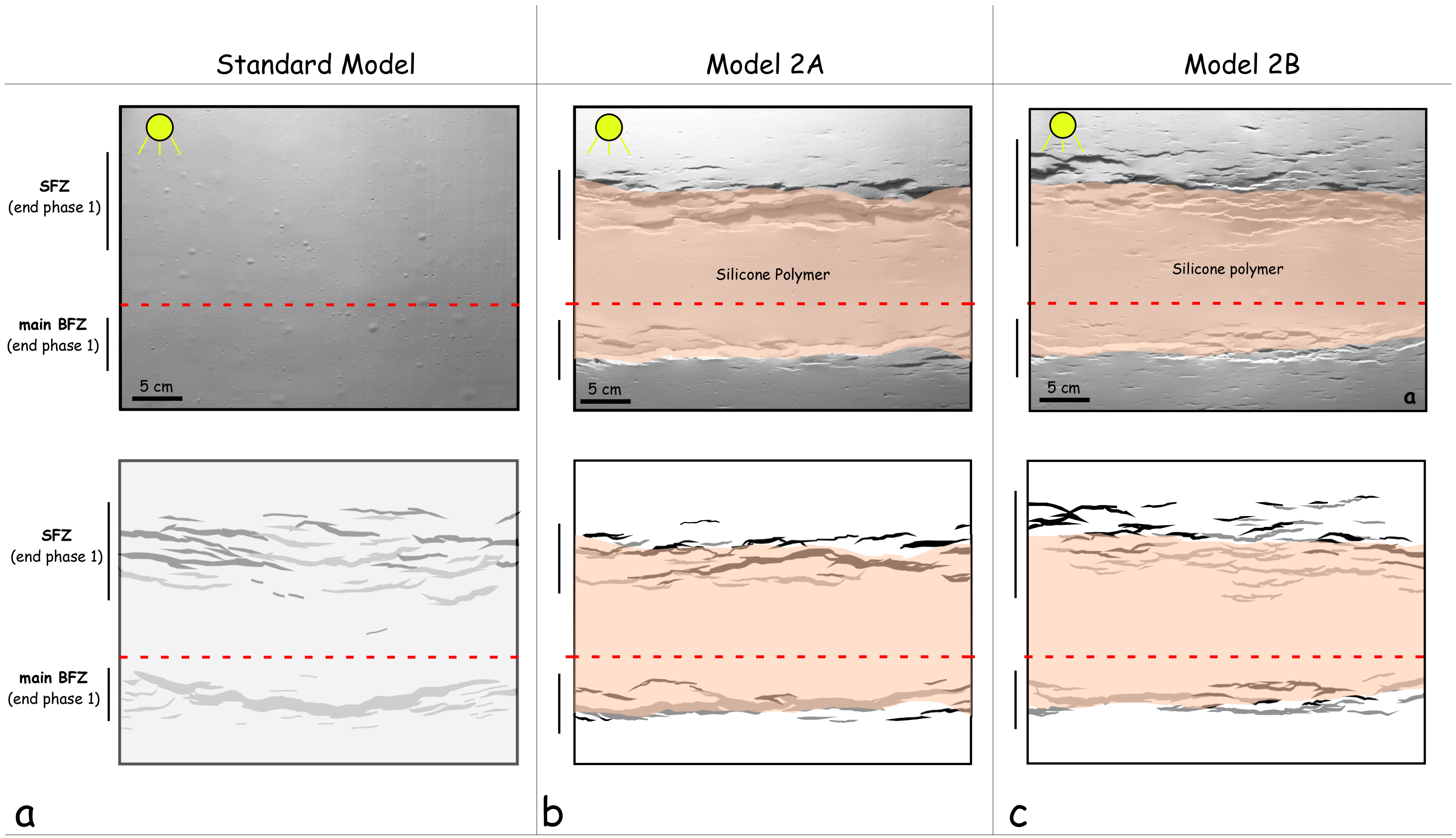

Figure 2.4. After deposition and aggradation. a) Standard model; b) Model 2A; c) Model 2B. **top.** Photograph of model surface after deposition of wet clay (standard) and silicone putty (models 2A & 2B) before 1 cm aggradation of wet clay. **bottom.** Line-drawing of model surface highlighting extent of putty. Red dashed line shows edge of fixed plate. Grey faults dip toward moving wall; black faults dip away from moving wall.

Figure 2.5. Model 1 (standard), evolution during phase 2. Overhead photographs showing evolution of surface deformation during phase 2. After addition of synrift clay and 1 cm of aggradation, model was subjected to additional 5 cm of orthogonal extension. Red dashed line indicates edge of fixed plate.

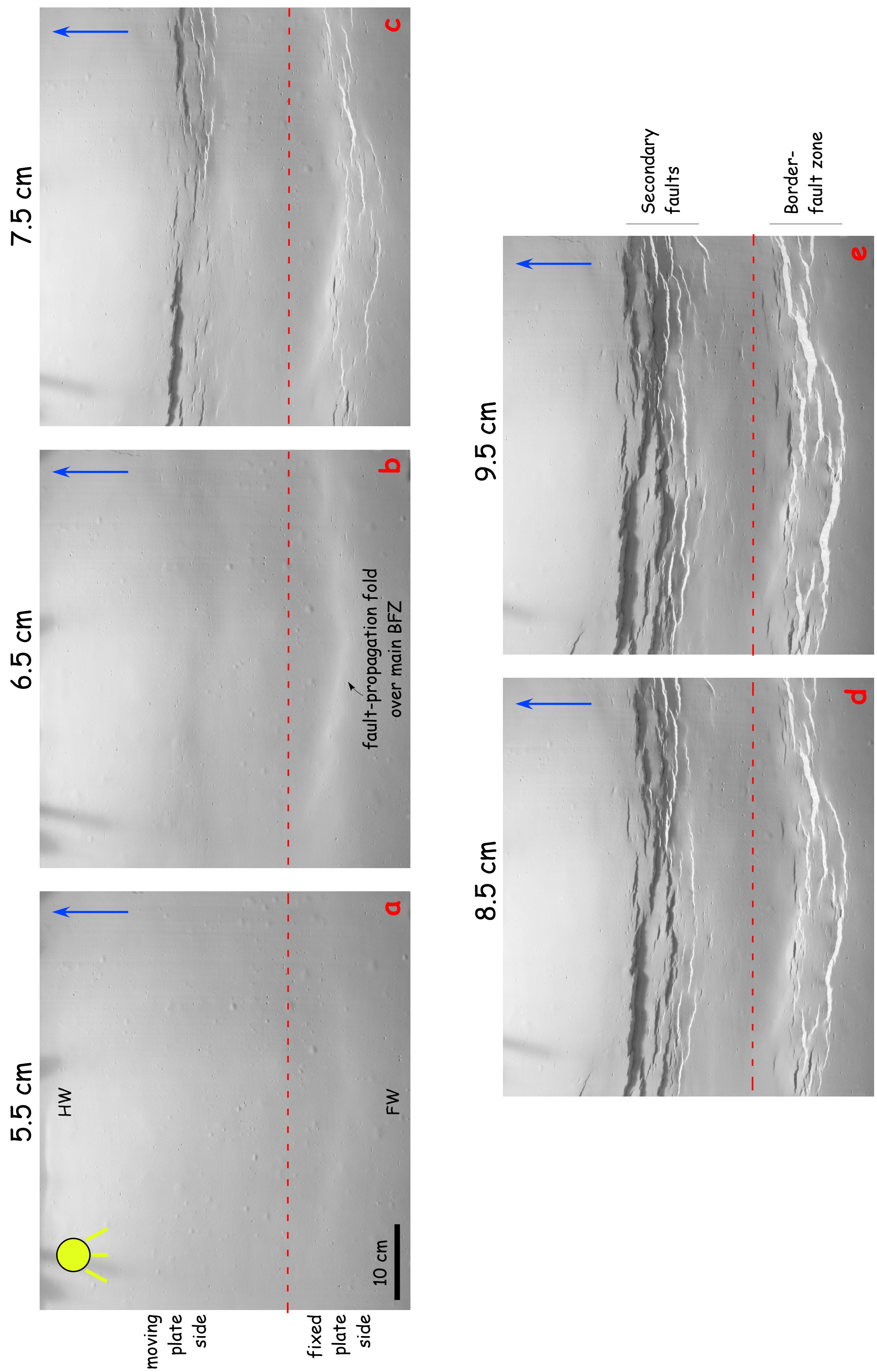
5.5 cm
6.5 cm
7.5 cm
8.5 cm
9.5 cm
HW
FW
10 cm
moving plate side
fixed plate side
fault-propagation fold over main BFZ
Secondary faults
Border-fault zone
a
b
c
d
e

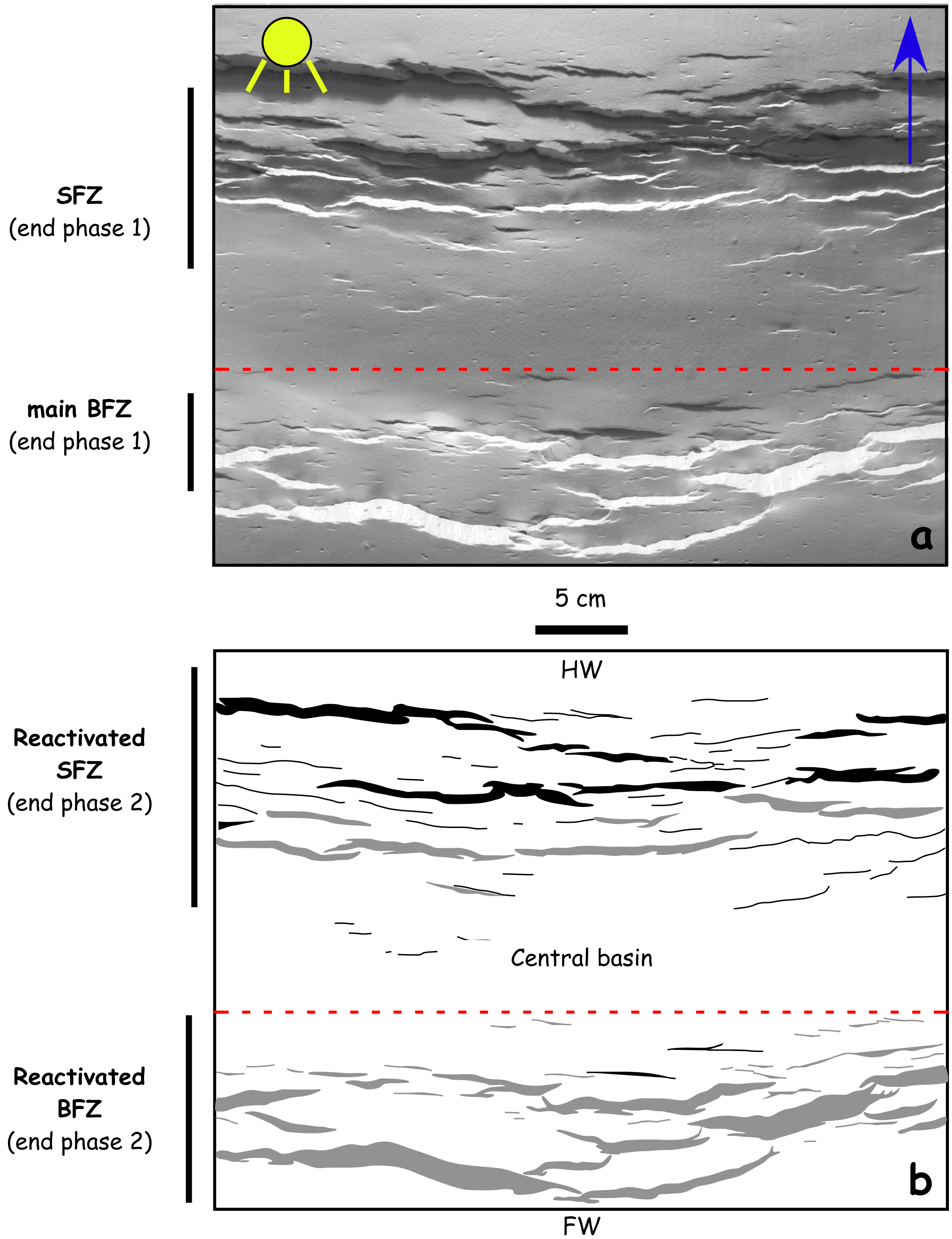

Figure 2.6. Model 1 (standard), end phase 2. **a.** Photograph of model surface after 10 cm of extension. Blue arrow shows displacement direction of moving plate. **b.** Line drawing of model surface. Note that the width of both the main border-fault zone (BFZ) and the secondary fault zone (SFZ) have increased at the end of phase 2. Red dashed line shows edge of fixed plate. Grey faults dip toward moving wall; black faults dip away from moving wall. HW=hanging wall of BFZ; FW= footwall of BFZ

Figure 2.7. Model 1 (standard), evolution during phase 3. Overhead photographs showing evolution of surface deformation during phase 3. Note change in surface topography after 10 cm of shortening. Although uplifted above regional level, main border-fault zone still shows normal separation. Red dashed line indicates edge of fixed plate.

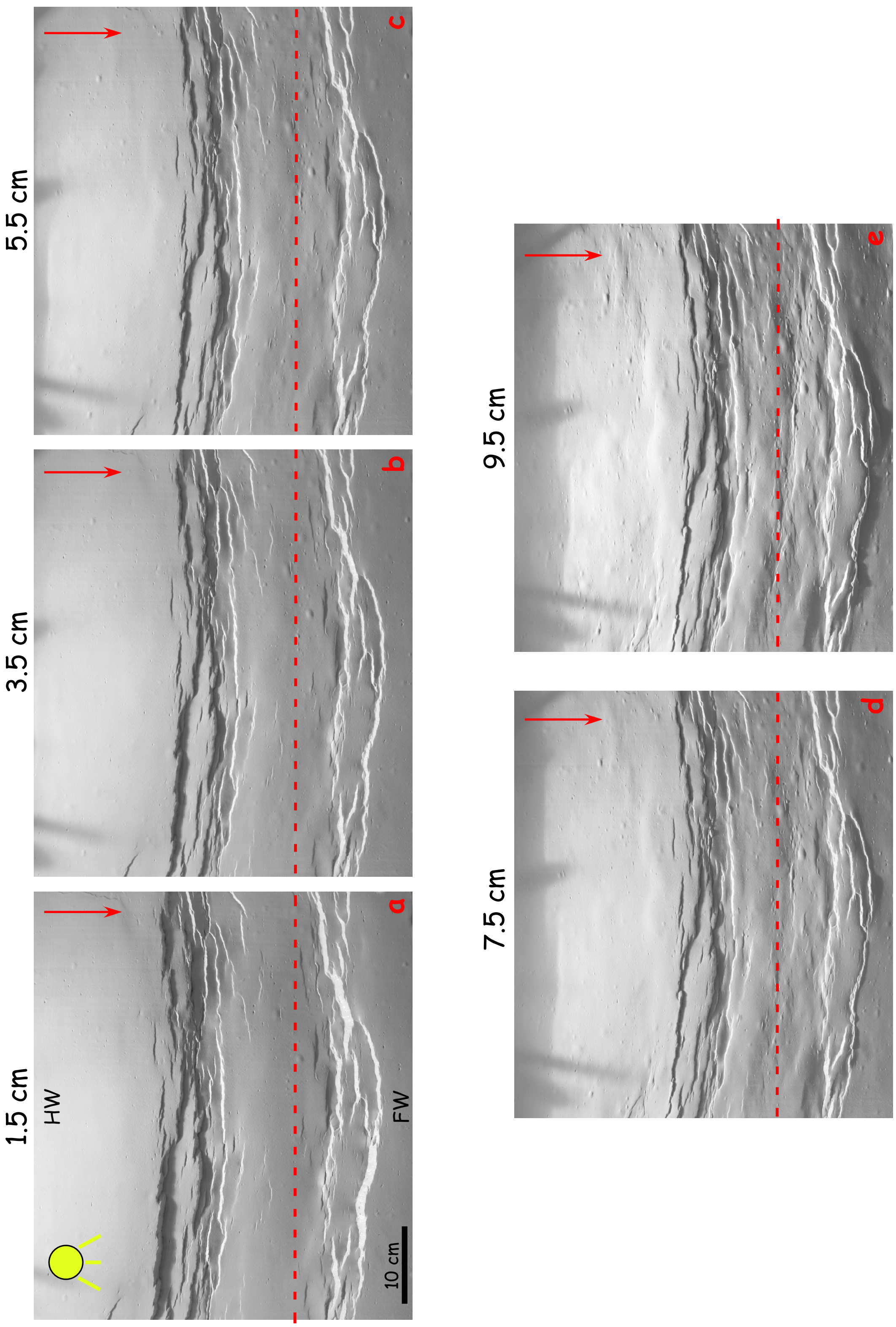
1.5 cm
3.5 cm
5.5 cm
7.5 cm
9.5 cm
HW
FW
10 cm
a
b
c
d
e

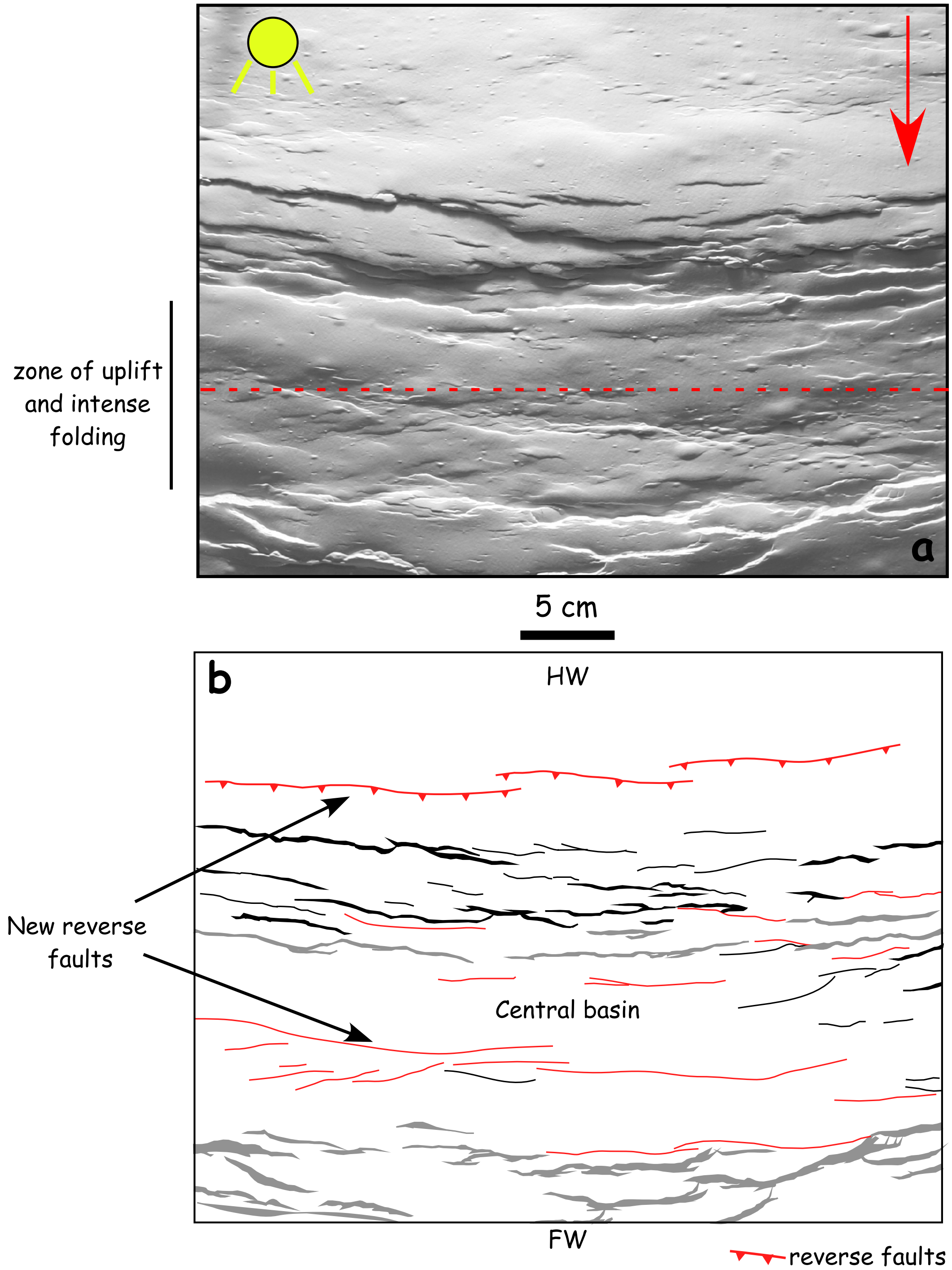

Figure 2.8. Model 1 (standard), end phase 3. **a.** Photograph of model surface after 10 cm of shortening. Red arrow shows displacement direction of moving plate. **b.** Line drawing of model surface. Pre-existing normal faults (grey/black) are reactivated with reverse slip. Red faults are newly formed reverse faults. Red dashed line shows edge of fixed plate. Grey faults dip toward moving wall, black faults dip away from moving wall.

Figure 2.9. Model 2A, evolution during phase 2. Overhead photographs showing evolution of surface deformation during phase 2. After addition of synrift putty and clay cover, model subjected to additional 5 cm of orthogonal extension. Red dashed line indicates edge of fixed plate.

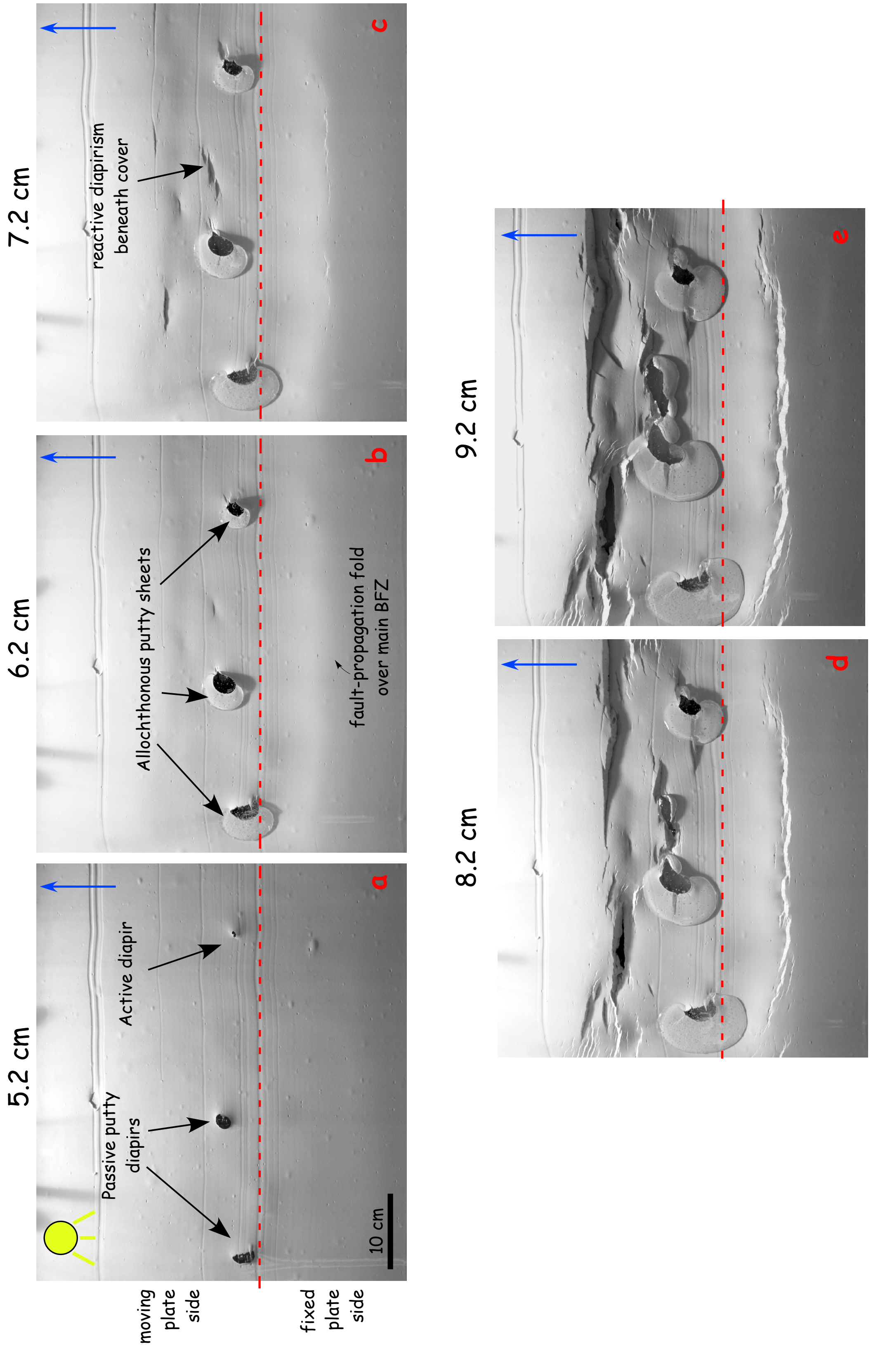
5.2 cm
6.2 cm
7.2 cm
8.2 cm
9.2 cm
Passive putty diapirs
Active diapir
Allochthonous putty sheets
reactive diapirism beneath cover
fault-propagation fold over main BFZ
10 cm
moving plate side
fixed plate side
a
b
c
d
e

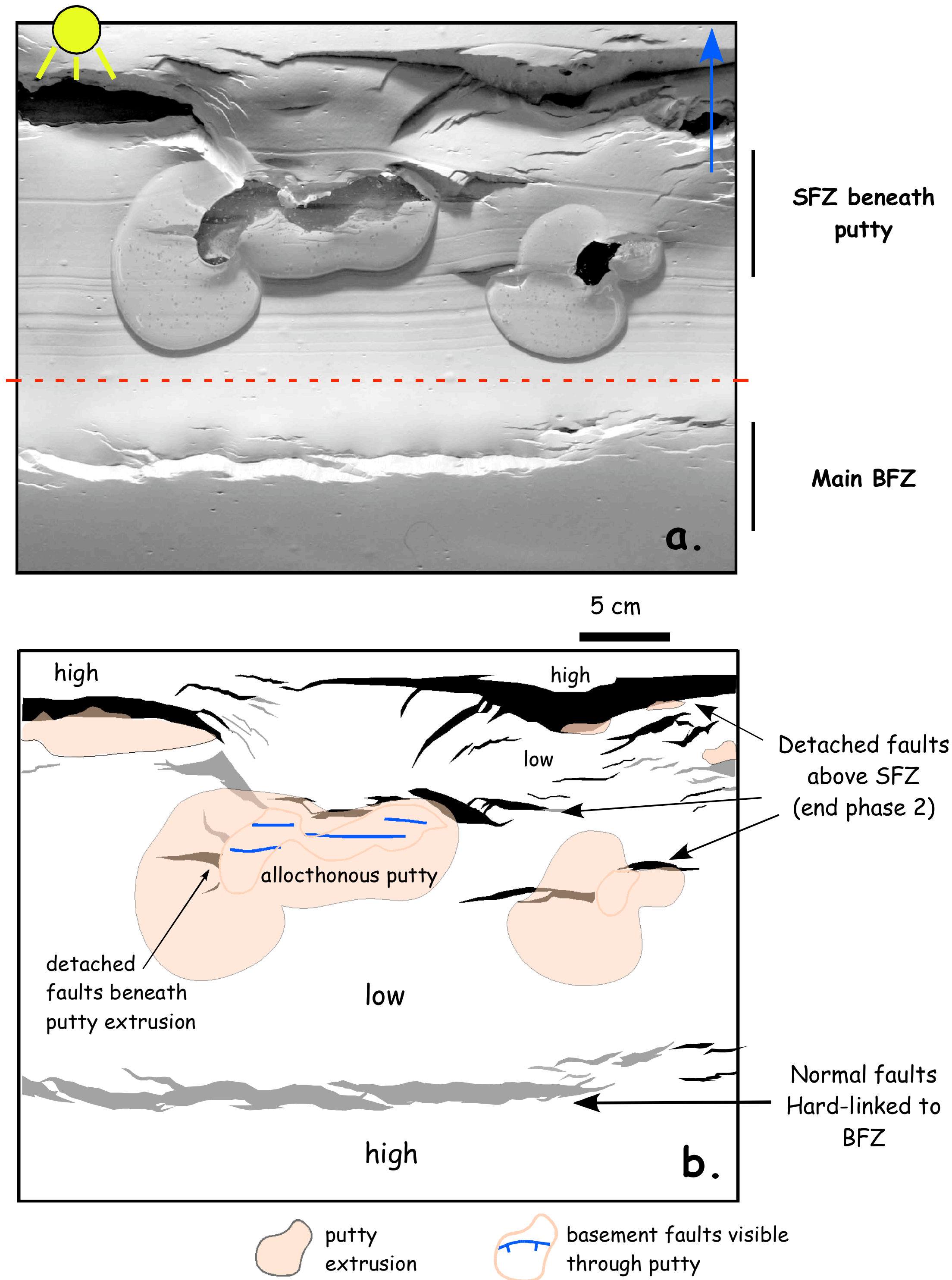

Figure 2.10. Model 2A, end of phase 2. **a.** Photograph of model surface after 10 cm of extension. Blue arrow shows displacement direction of moving plate. Red dashed line shows edge of fixed plate. **b.** Line-drawing of model surface. Blue faults are subputty faults with normal separation visible through putty layer. Grey faults dip toward moving wall; black faults dip away from moving wall.

Figure 2.11. Model 2A, evolution during phase 3 (shortening). Red arrow indicates shortening direction. Overhead photographs showing evolution of surface deformation during phase 3. Red dashed line indicates edge of fixed plate. Note drastic change in surface topography after 10 cm of shortening. Putty movement during shortening produces deep withdraw basins (e.g. blue dashed box above), and localized topographic highs above regional level . The main border fault system still maintains normal separation at the end of phase 3.

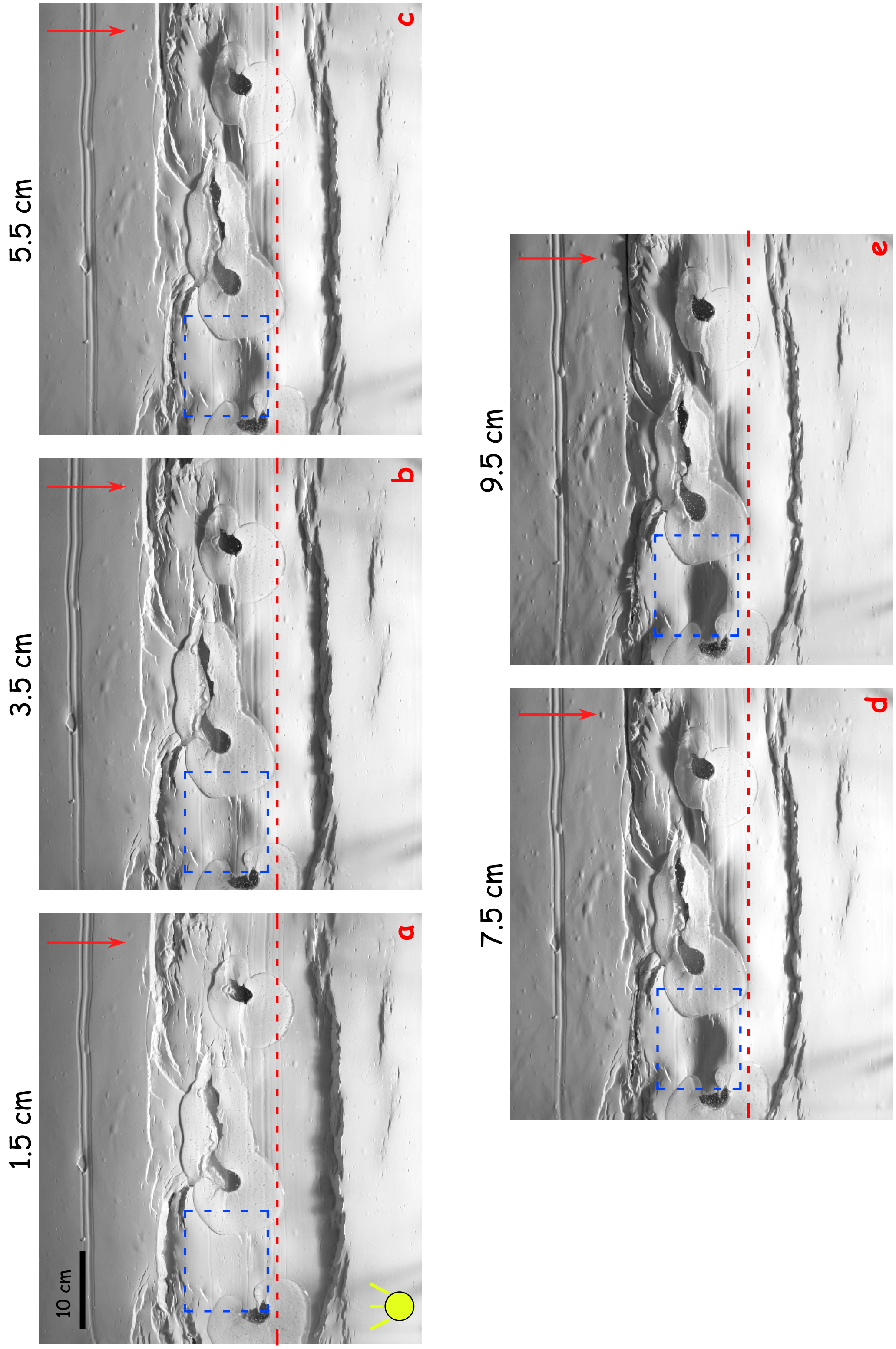

1.5 cm
3.5 cm
5.5 cm
7.5 cm
9.5 cm
10 cm
a
b
c
d
e

Figure 2.12. Oblique photographs of model surface at end of phase 3. *See detailed explanation of figure in text.*

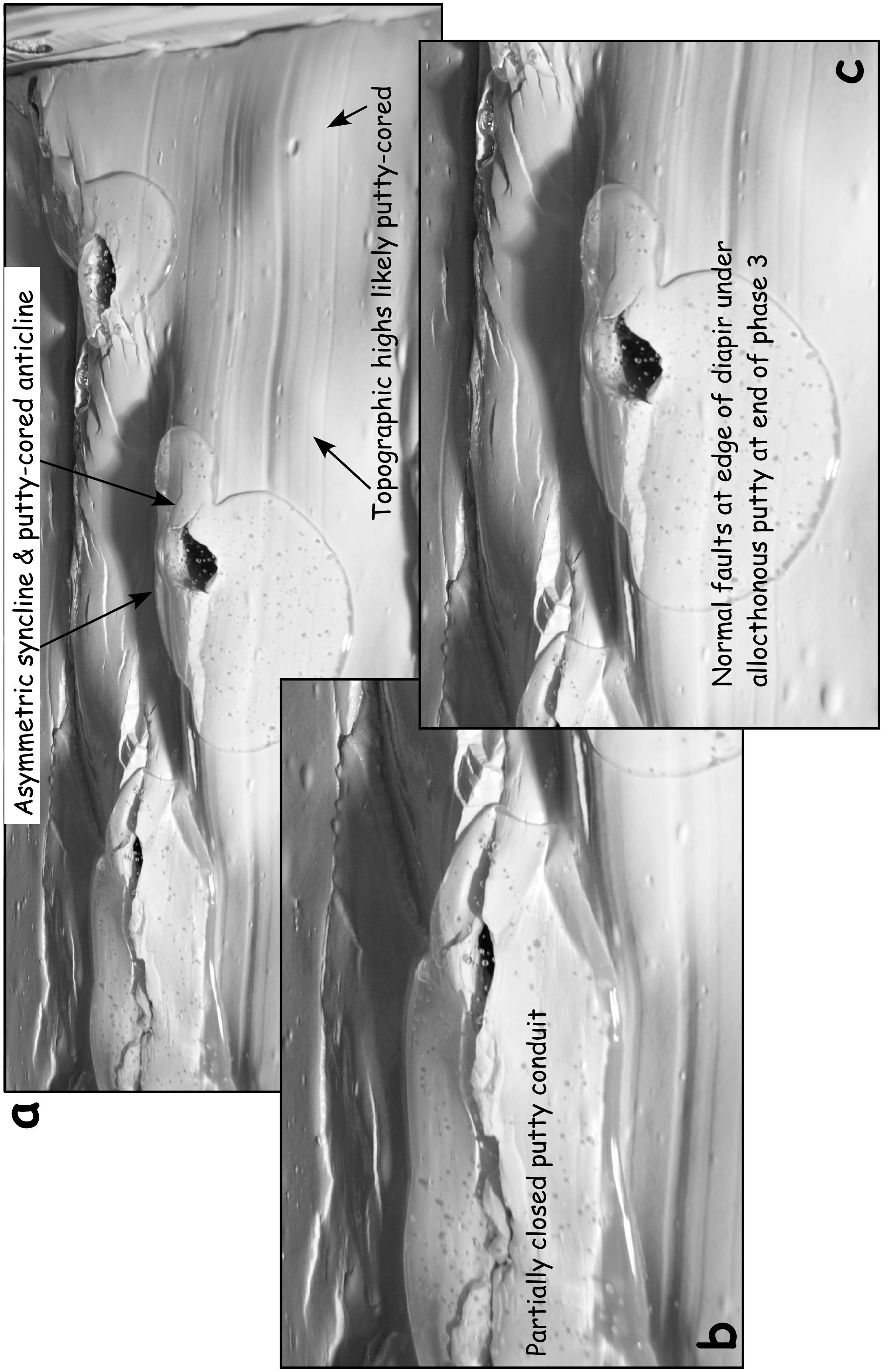
a
Asymmetric syncline & putty-cored anticline
Topographic highs likely putty-cored
b
Partially closed putty conduit
c
Normal faults at edge of diapir under
allocthonous putty at end of phase 3

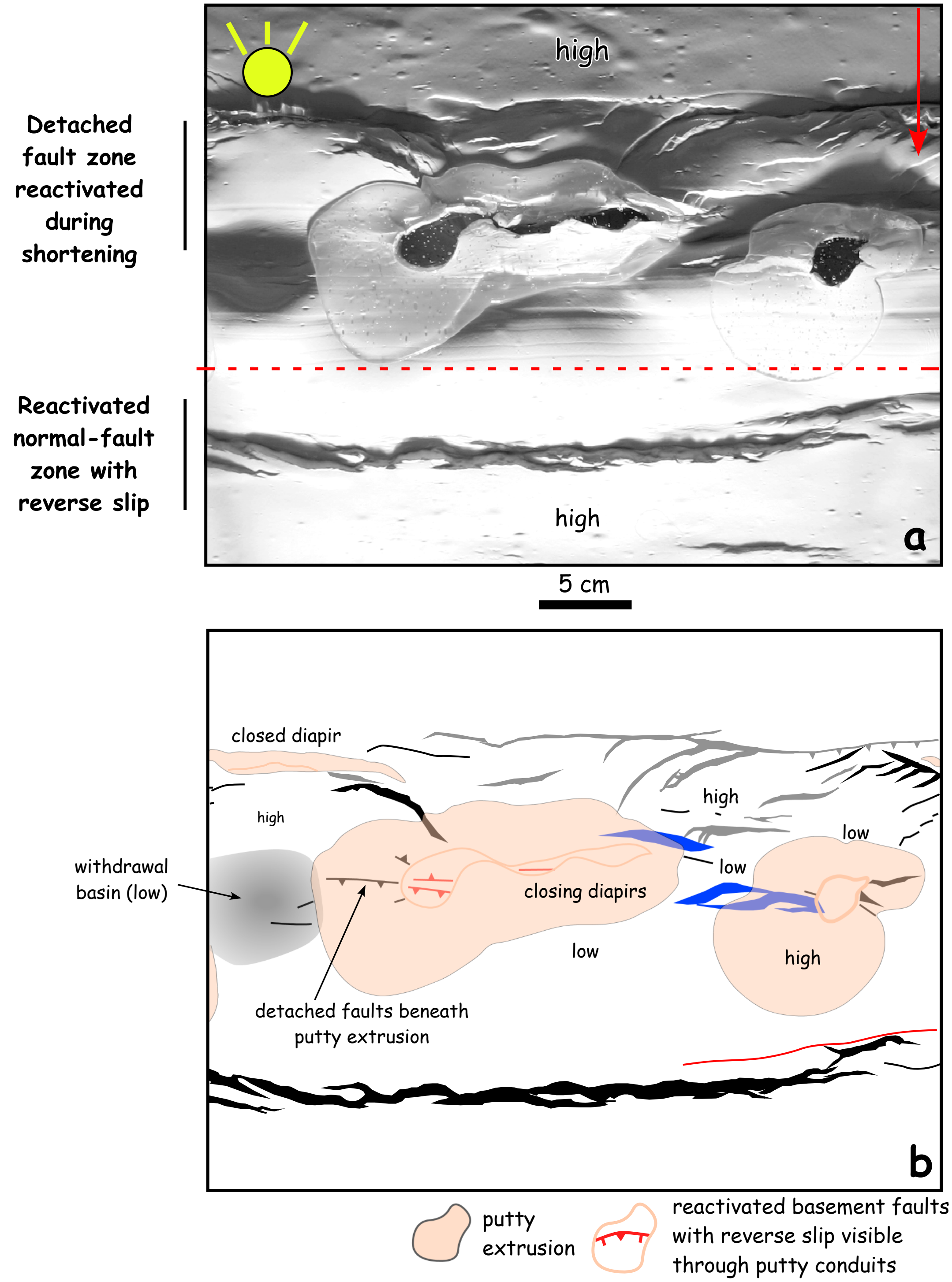

Figure 2.13. Model 2A, end of phase 3. **a.** Photograph of model surface after 10 cm of extension. Red arrow shows displacement direction of moving plate. Red dashed line shows edge of fixed plate. **b.** Line drawing of model surface. Red faults are reactivated faults visible through putty layer and new reverse faults; blue faults continue to grow as normal faults. Grey/blue faults dip away from moving wall; black faults dip towards moving wall.

Figure 2.14. Model 2B, evolution during phase 2. Overhead photographs showing evolution of surface deformation during phase 2. Red dashed line indicates edge of fixed plate. After addition of synrift putty and clay cover, model was subjected to additional 5 cm of orthogonal extension.

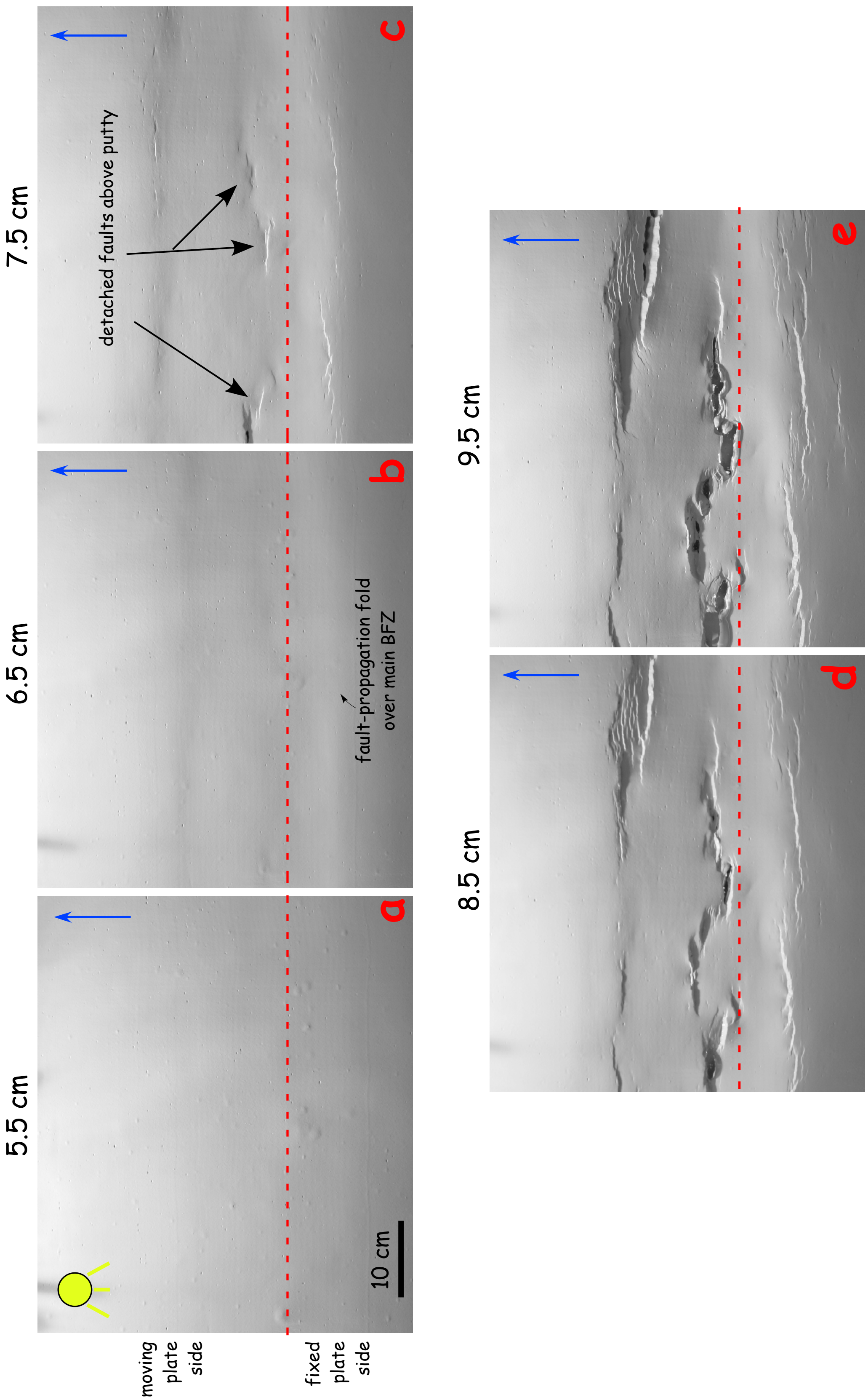
5.5 cm
6.5 cm
7.5 cm
8.5 cm
9.5 cm
moving plate side
fixed plate side
10 cm
a
b
c
d
e
detached faults above putty
fault-propagation fold over main BFZ

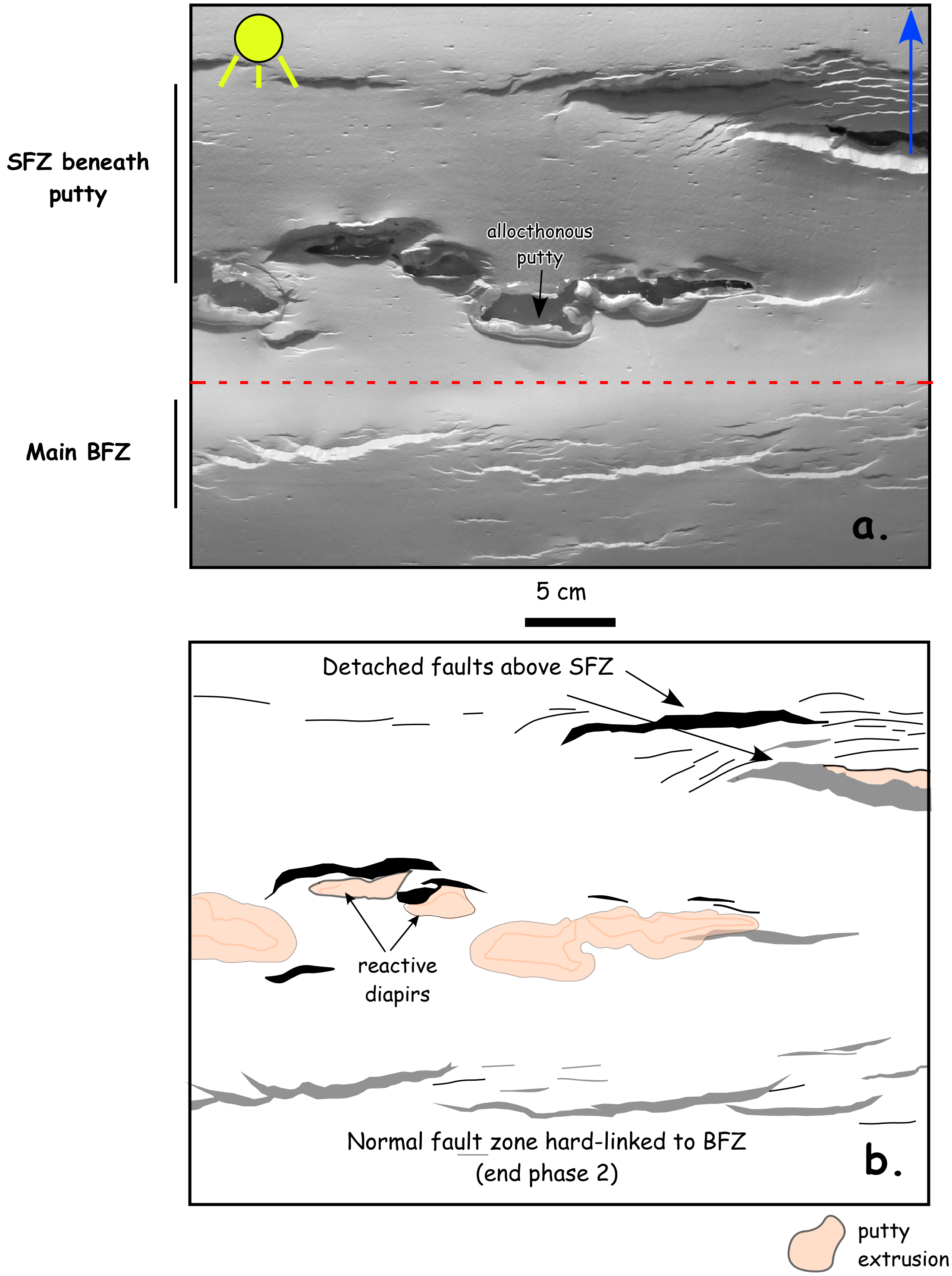

Figure 2.15. Model 2B, end of phase 2. **a.** Photograph of model surface after 10 cm of extension. Blue arrow shows displacement direction of moving plate. Red dashed line shows edge of fixed plate. **b.** Line drawing of model surface. Grey faults dip toward moving wall; black faults dip away from moving wall.

Figure 2.16. Model 2B, evolution during phase 3 (shortening). Red arrow indicates shortening direction. Overhead photographs showing evolution of surface deformation during phase 3. Red dashed line indicates edge of fixed plate. Putty movement during shortening produced withdrawal basins, and localized topographic highs above regional level. Main border-fault system still maintains normal separation at the end of phase 3.

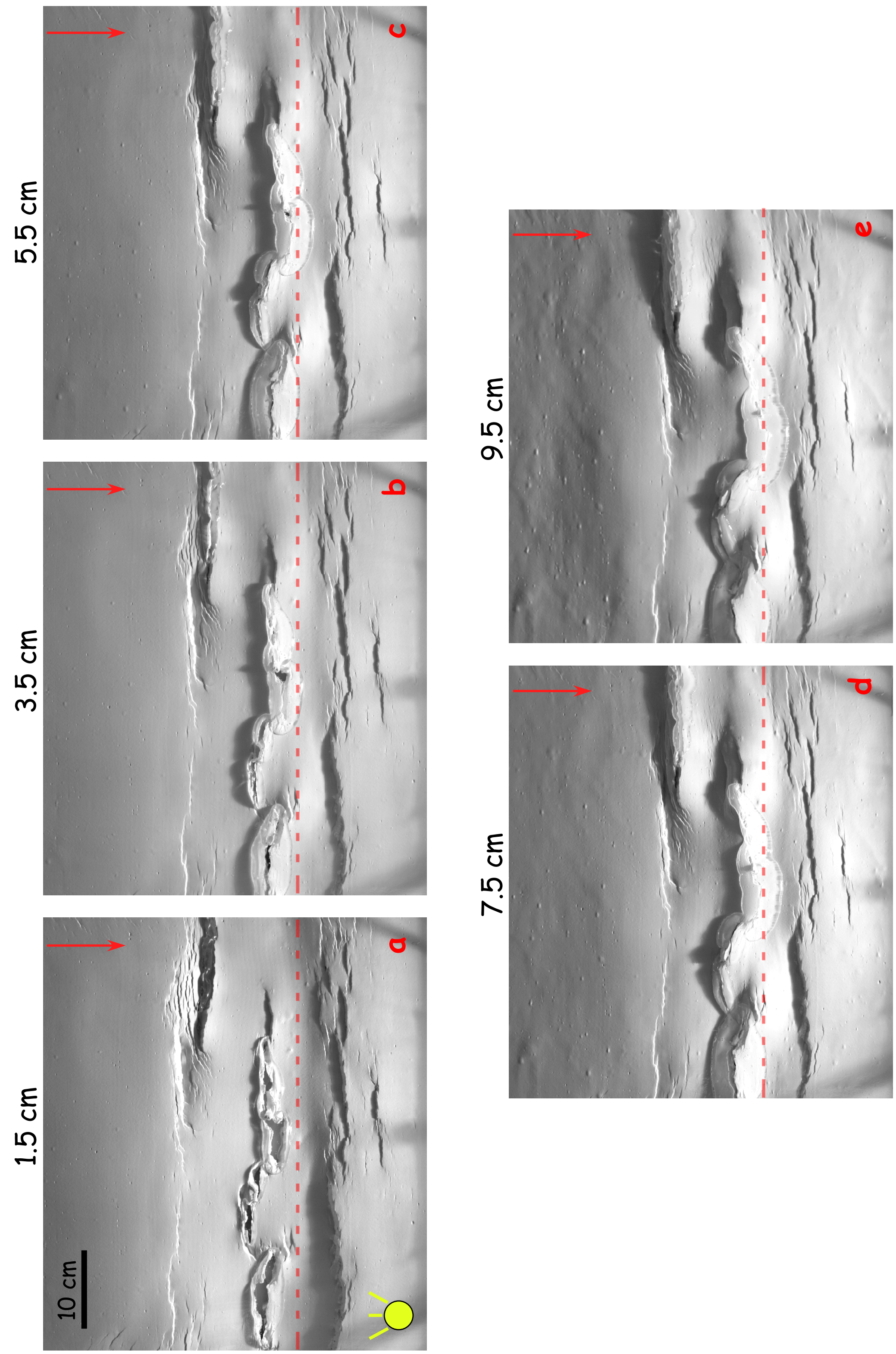
1.5 cm
3.5 cm
5.5 cm
7.5 cm
9.5 cm
10 cm
a
b
c
d
e

Figure 2.17. Oblique photographs of model surface at end of phase 3. See text for detailed explanation. Red dashed lines indicate location of main border-fault zone (BFZ)

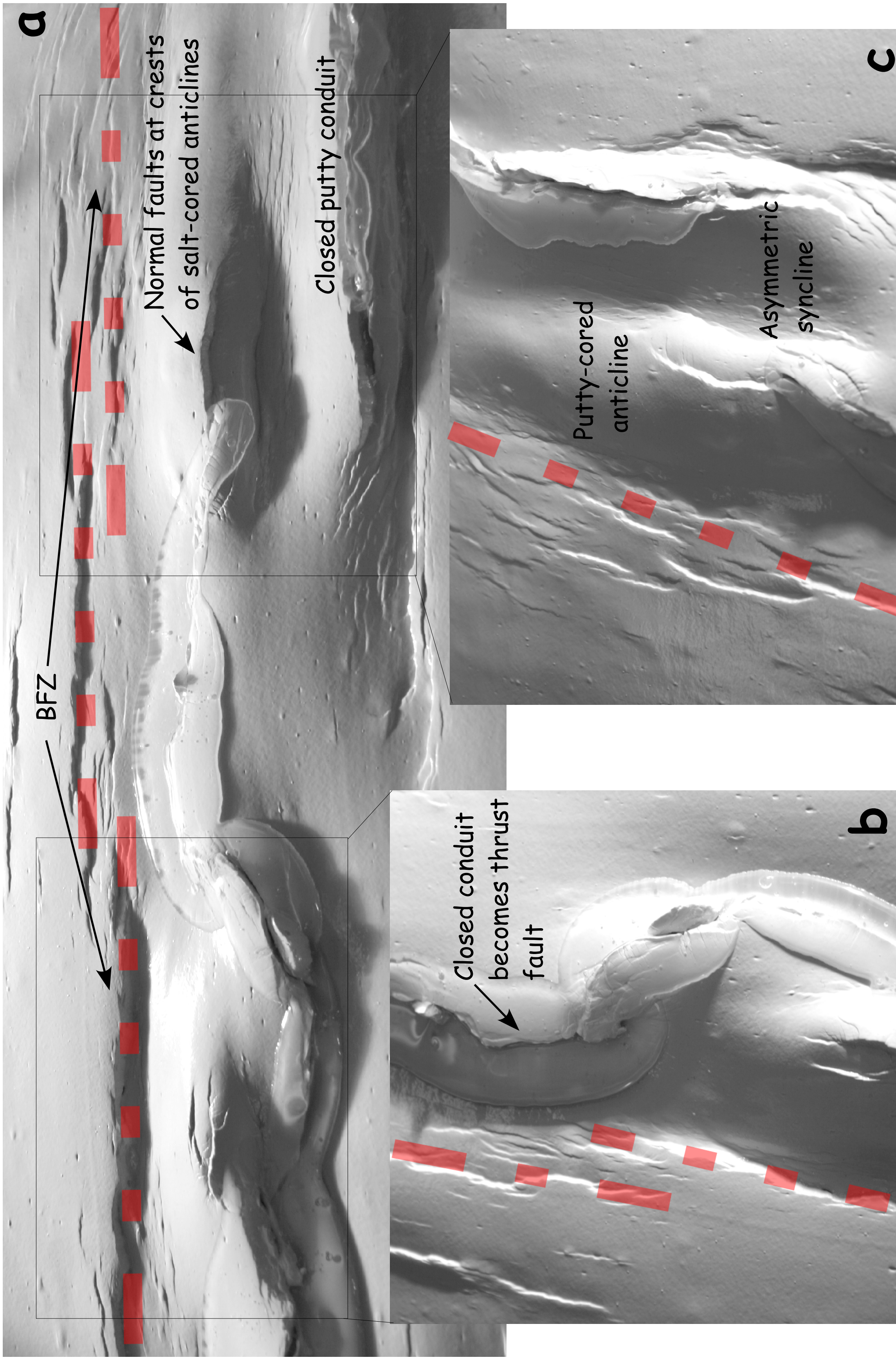
a
Normal faults at crests of salt-cored anticlines
Closed putty conduit
BFZ
b
Closed conduit becomes thrust fault
c
Putty-cored anticline
Asymmetric syncline

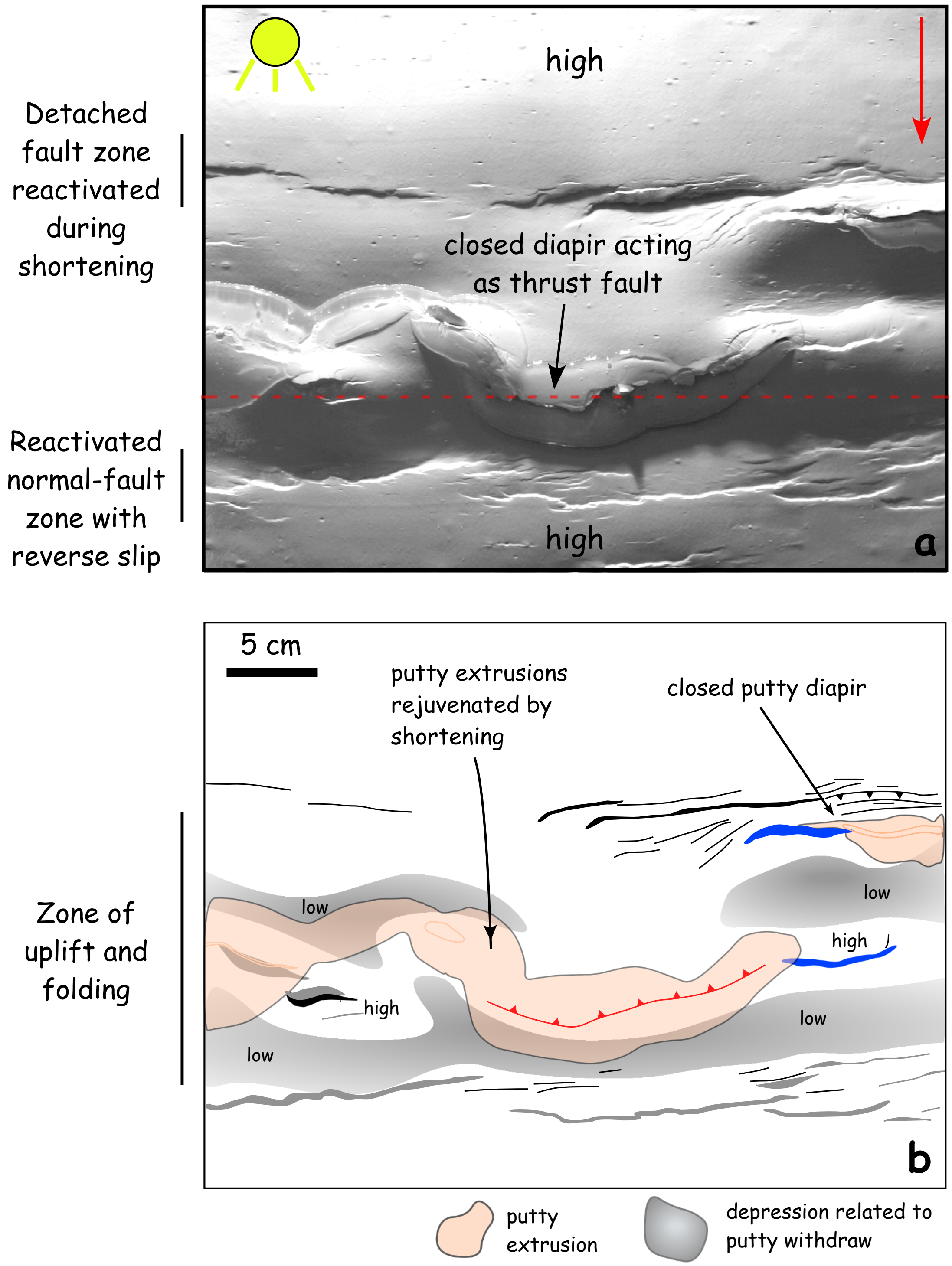

Figure 2.18. Model 2B, end of phase 3. **a.** Photograph of model surface after 10 cm of extension. Red arrow shows displacement direction of moving plate. Red dashed line shows edge of fixed plate. **b.** Line-drawing of model surface. Red fault is closed diapir acting as thrust fault. Blue faults continue to grow as normal faults. Grey/blue faults dip towards moving wall; black faults dip away from moving wall.

Figure 2.19. Summary figure showing line drawings of model surface at end of phase 2 extension (top), and Phase 3 inversion (bottom). Red faults are reverse faults. In phase 3 (bottom), blue faults continue to grow as normal faults. In both phase 2 and phase 3, black faults dip toward the moving wall; grey faults dip away from moving wall.

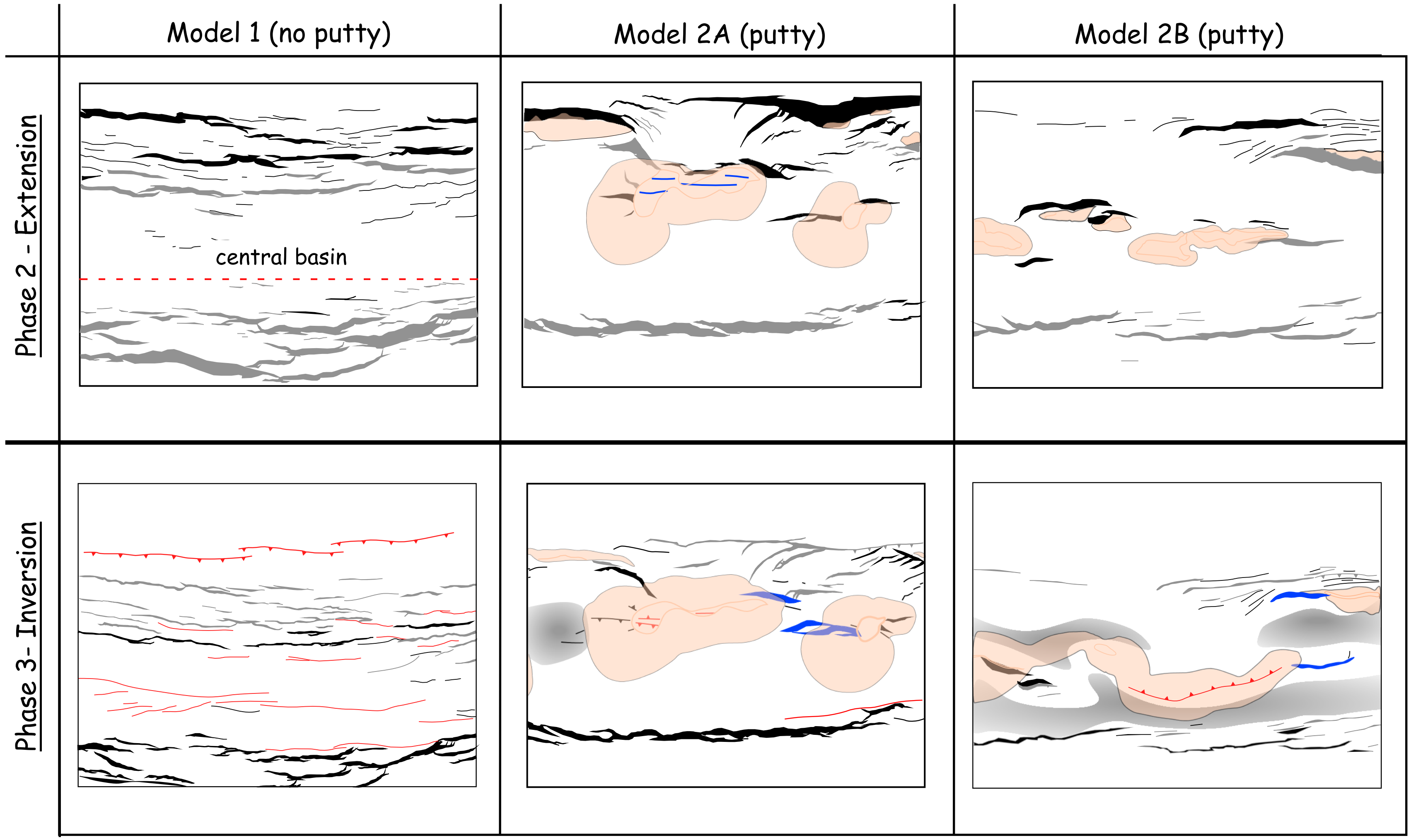
Model 1 (no putty)
Model 2A (putty)
Model 2B (putty)
Phase 2 - Extension
Phase 3- Inversion
central basin

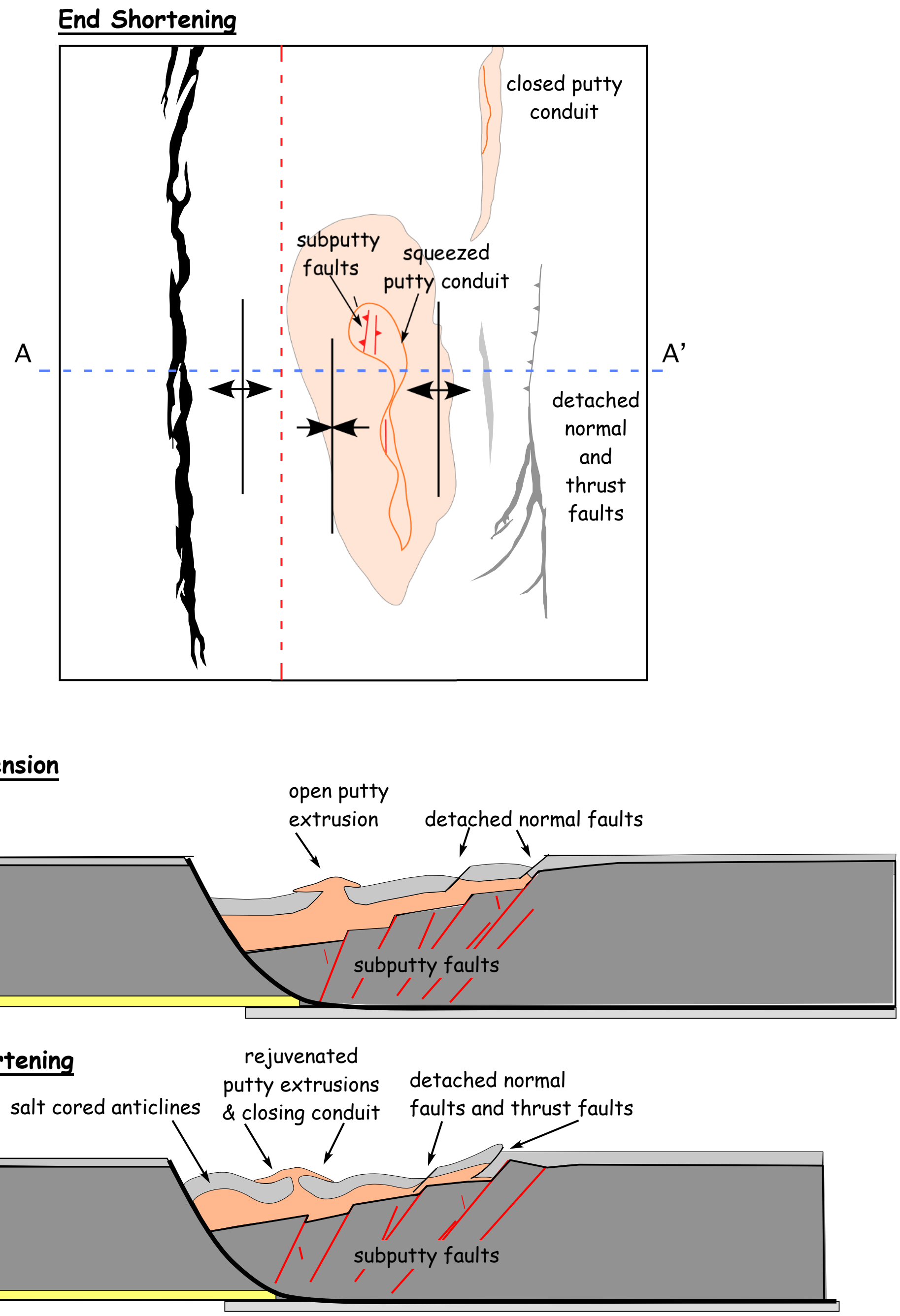

Figure 2.20. Summary figure showing line drawings of model surface and hypothetical cross-section after extension (top), and inversion (bottom). Red dashed line is edge of fixed plate. Red faults are subputty faults. Grey and black faults are supraputty faults, black faults dip toward the moving wall; grey faults dip away from moving wall.

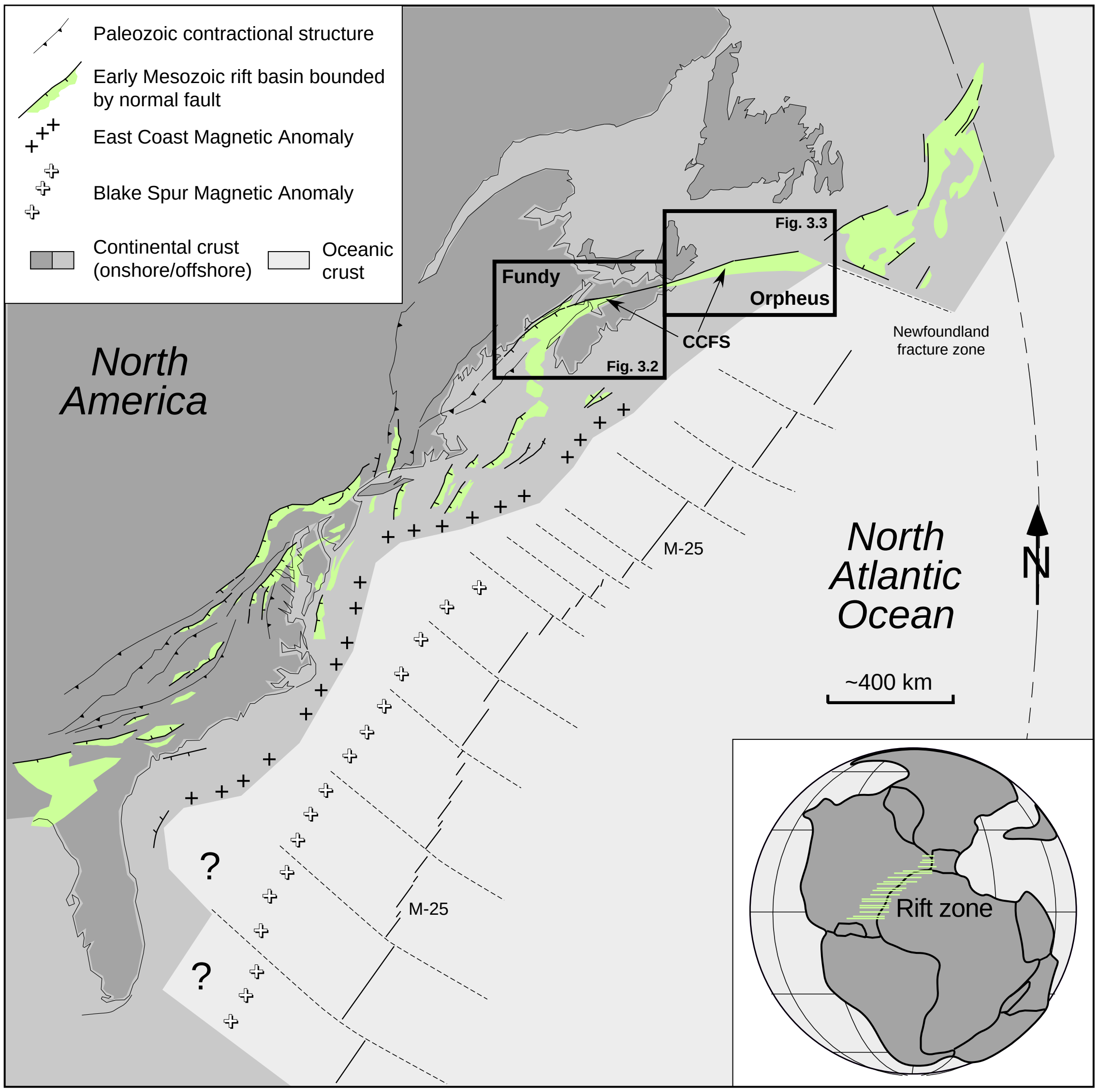

Figure 3.1. Major Paleozoic contractional structures and early Mesozoic rift basins of eastern North America, and tectonic features of the eastern North Atlantic Ocean (Kiltgord et al., 1988; Olsen et al., 1989; Welsink et al., 1989). Black boxes indicate study areas. CCFS = Cobequid- Chedabucto fault system. Inset shows Pangea supercontinent during Late Triassic time (Olsen, 1997) and green area highlights rift zone between eastern North America, northwest Africa, and Iberia. Modified from Withjack and Schlische (2005).

Figure 3.2. Map and seismic sections across the Fundy basin. (a) Map of the Fundy basin highlighting major structural components and basin-bounding faults. *CCFS = Cobequid-Chedabucto fault system.* Red dashed lines indicate locations of seismic lines. (b) Seismic line 87-79, and onshore continuation. (c) Northeastern portion of seismic line 82-28 and onshore continuation. (d) Close up of dashed box in **c**. Top: uninterpreted seismic profile. Bottom: corresponding interpretation highlighting folded synrift strata against major basin-bounding fault. Seismic lines displayed at approximately 1:1 assuming an average velocity of 3.5 km/s. Arrows show component of fault slip in plane of cross section. (Modified from Baum et al., 2008; Withjack et al., 2009)

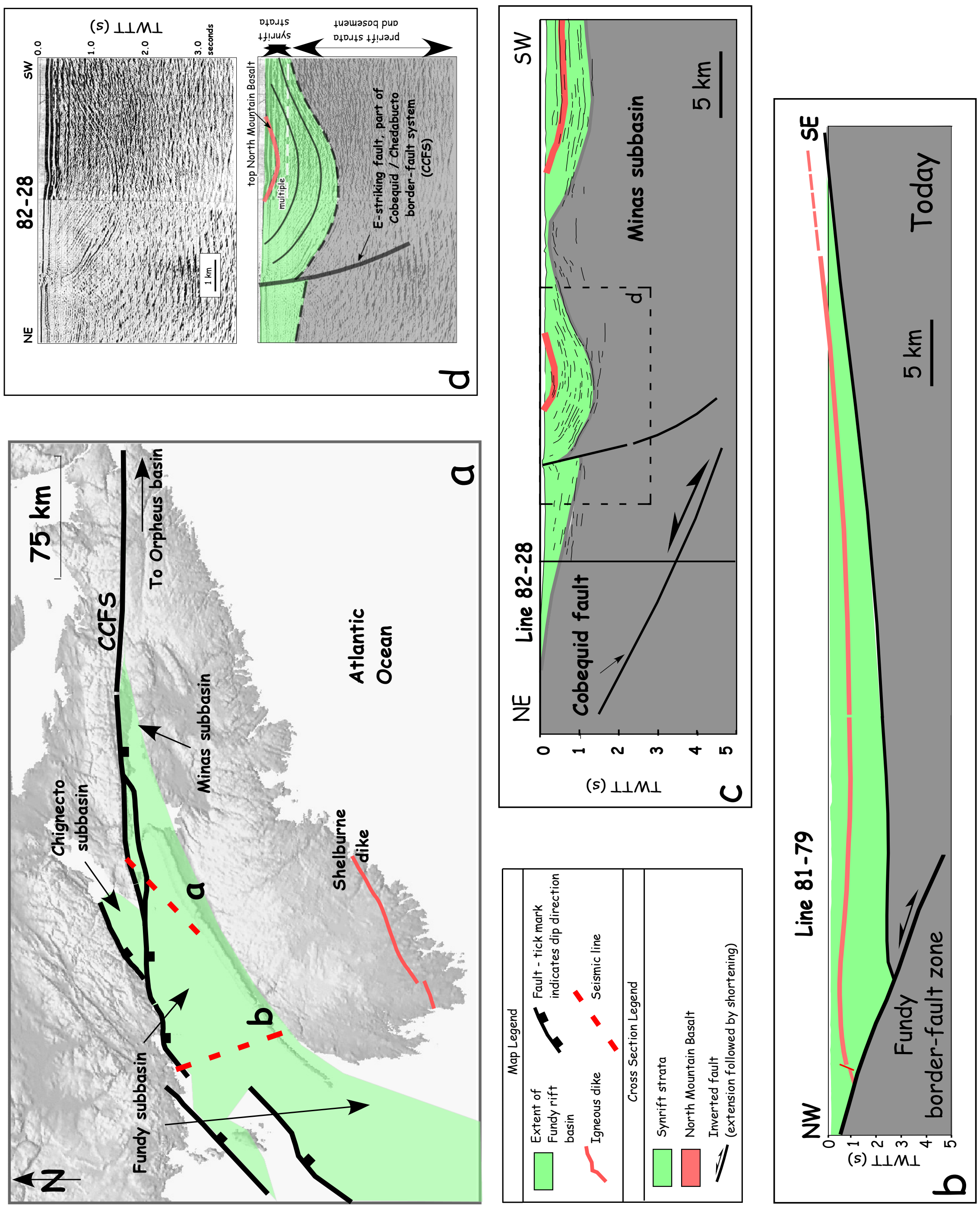

a
75 km
CCFS
To Orpheus basin
Chignecto subbasin
Minas subbasin
Fundy subbasin
Atlantic Ocean
Shelburne dike
a
b
Map Legend
Extent of Fundy rift basin
Igneous dike
Fault - tick mark indicates dip direction
Seismic line
Cross Section Legend
Synrift strata
North Mountain Basalt
Inverted fault (extension followed by shortening)
b
Line 81-79
NW
SE
TWTT (s)
0
1
2
3
4
5
Fundy border-fault zone
5 km
Today
c
Line 82-28
NE
SW
TWTT (s)
0
1
2
3
4
5
Cobequid fault
Minas subbasin
5 km
d
d
82-28
NE
SW
0.0
1.0
2.0
3.0
seconds
TWTT (s)
1 km
top North Mountain Basalt
multiple
synrift strata
prerift strata and basement
E-striking fault, part of Cobequid / Chedabucto border-fault system (CCFS)

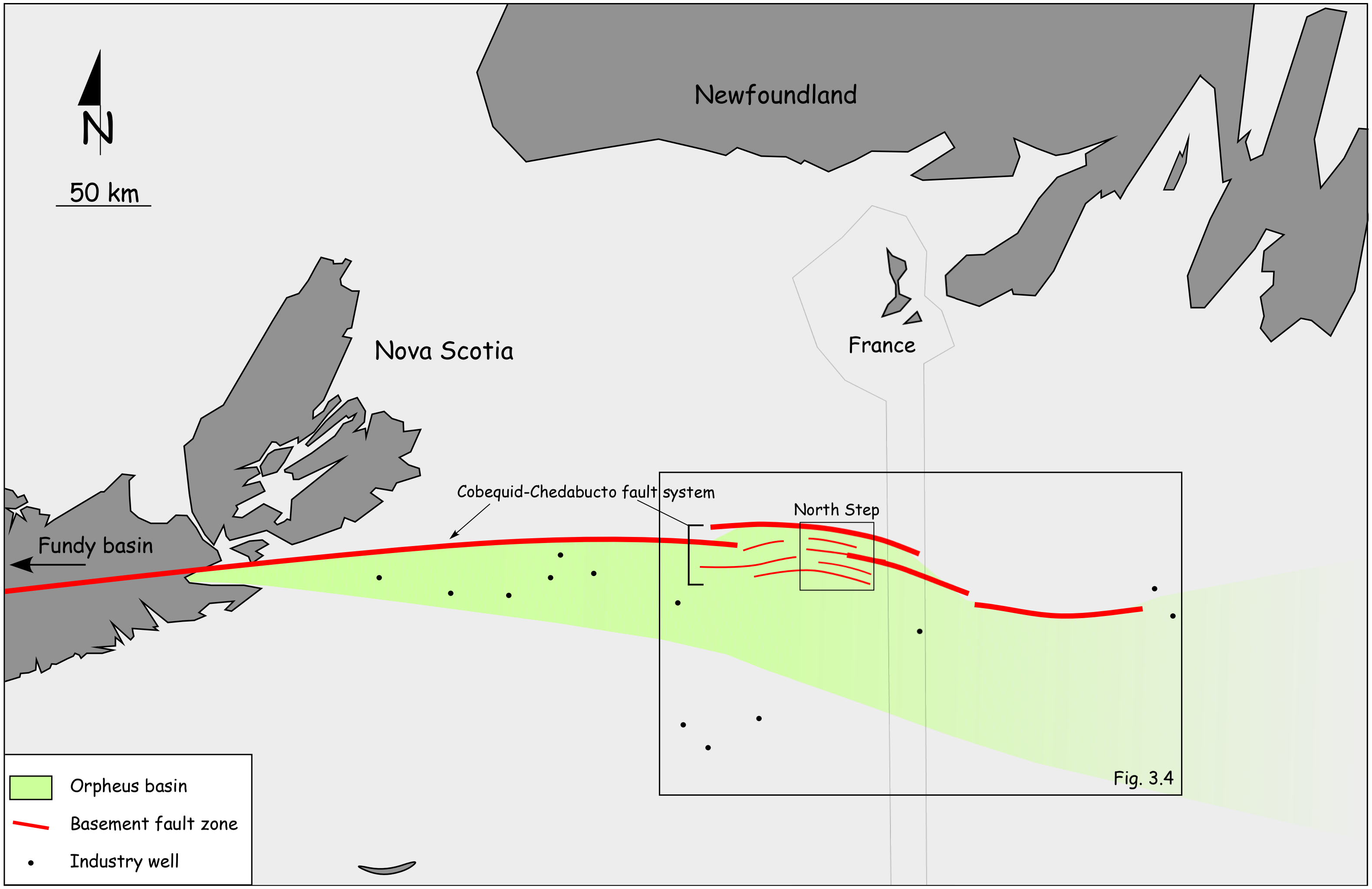

Figure 3.3. Structural components of offshore Nova Scotia and southern Newfoundland. Red lines show Cobequid-Chedabucto fault system (CCFS). Thick red lines indicate faults with largest displacements. Black box indicates location of seismic survey. See Figure 3.4 for line locations.

Figure 3.4. Map showing extent of seismic coverage. Orpheus basin has three segments based on quality of seismic data near major basement faults. Note high density of seismic lines in the northern part of the central segment. Dashed box indicates North Step (i.e., the study area). Five industry wells are used to tie seismic lines with regional stratigraphy: (1) Hesper I-52, (2) Sachem D-76, (3) Dauntless D-35, (4) Emerillion C-56, (5) Hermine E-94

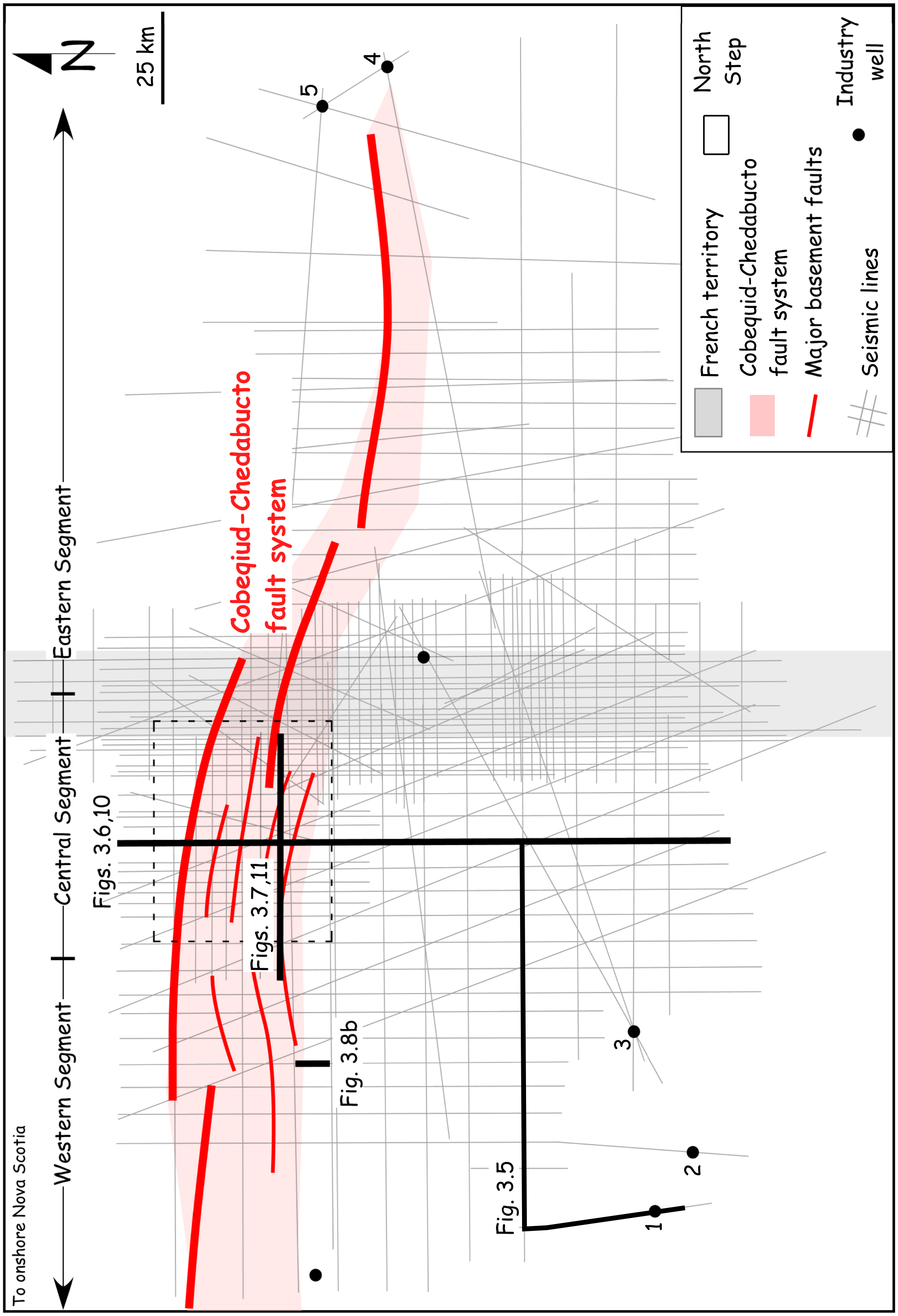

To onshore Nova Scotia
Western Segment
Central Segment
Eastern Segment
N
25 km
Cobequid-Chedabucto fault system
Figs. 3.6,10
Figs. 3.7,11
Fig. 3.8b
Fig. 3.5
1
2
3
4
5
French territory
North Step
Cobequid-Chedabucto fault system
Major basement faults
Industry well
Seismic lines

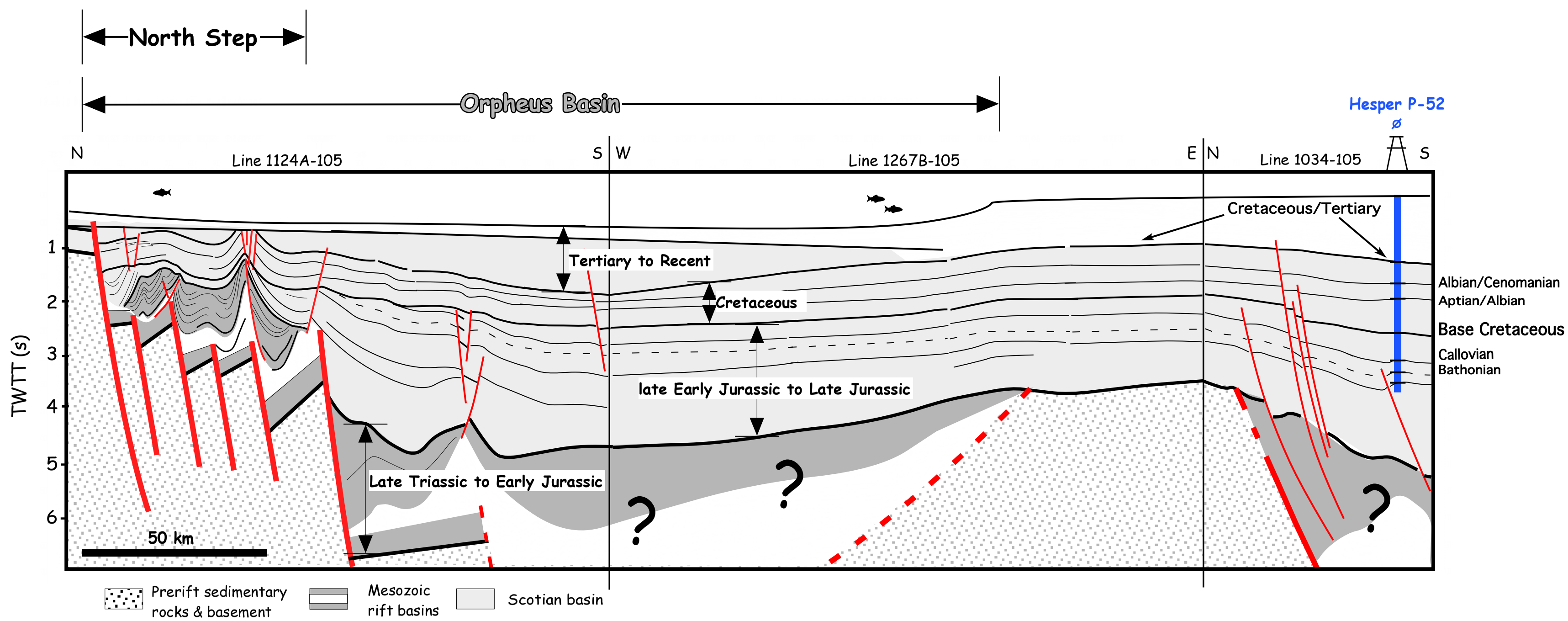

Figure 3.5. Regional composite seismic line highlighting ages of horizons based on well information. Line drawing composed of three seismic line segments (see figure 3.4 for composite line location). Dark grey area indicates Mesozoic rift basin infill, white area indicates salt. Light grey area indicates postrift Scotian basin infill. Blue line is Hesper P-52 well displayed in two-way travel time (TWTT). Thick red solid and dashed lines are basement faults, whereas thin solid red lines are faults that do not involve basement. Approximate vertical exaggeration is 8:1 assuming an average velocity of 3.5 km/s.

Figure 3.6. Seismic line 1124A-105 (top) and corresponding interpretation (bottom) of unconformity-bounded packages (A-D). Thick red lines are major basement-involved faults, and thin red lines are faults that do not involve basement. Vertical axis is in two-way travel time (TWTT). Line drawings of seismic profiles are displayed at approximately 1:1, assuming an average velocity of 3.5 km/s.

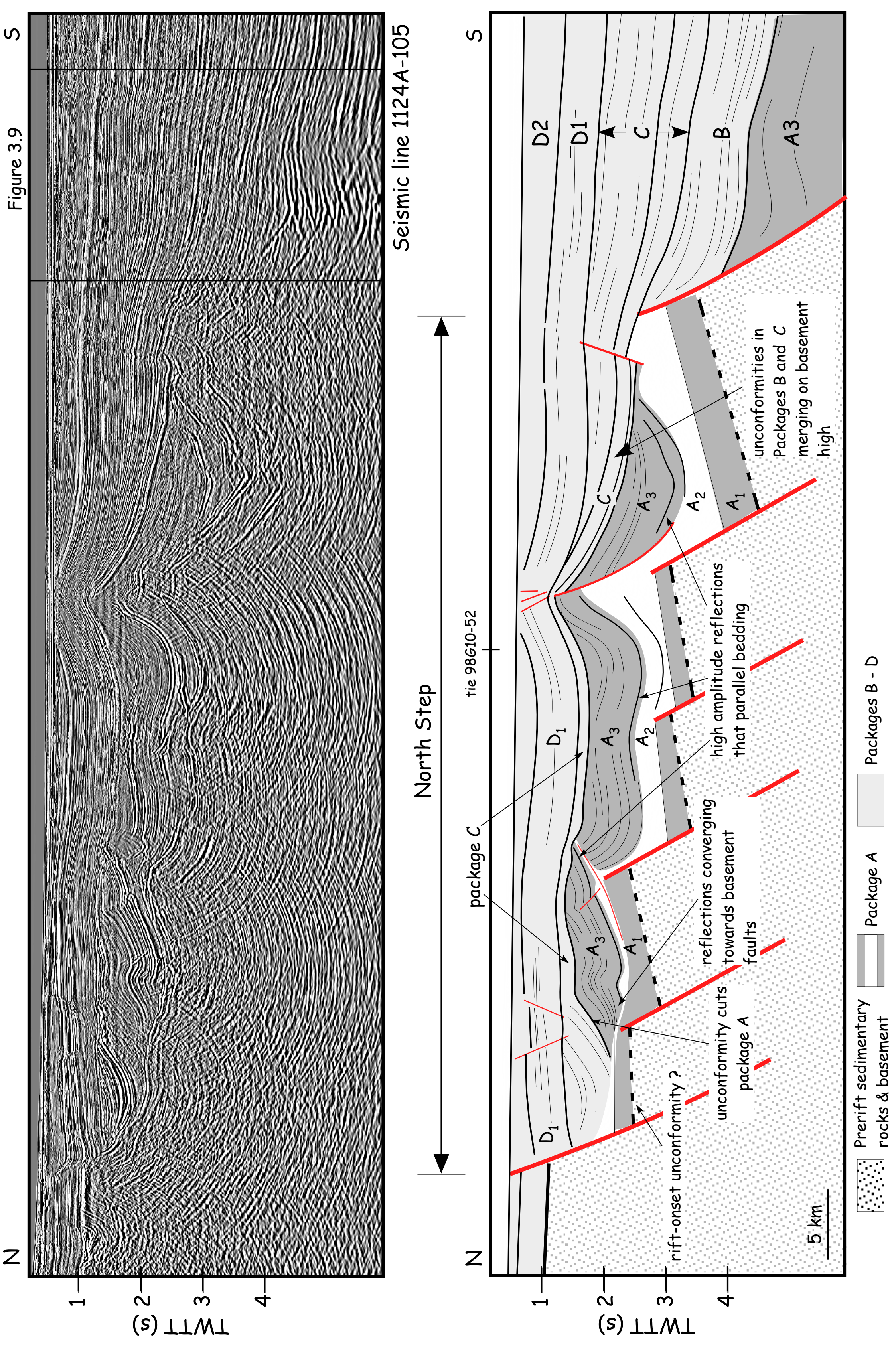

Figure 3.9
Seismic line 1124A-105
N
S
TWTT (s)
1
2
3
4
North Step
tie 98G10-52
package C
D2
D1
C
B
A3
D₁
A₃
A₂
A₁
rift-onset unconformity ?
unconformity cuts package A
reflections converging towards basement faults
high amplitude reflections that parallel bedding
unconformities in Packages B and C merging on basement high
5 km
Prerift sedimentary rocks & basement
Package A
Packages B - D

Figure 3.7. a) Close up of major unconformity on north end of seismic line 1124A-105. Note that unconformity is conformable with Package *C*, but truncates Package *A*. **b)** Seismic line 98G10-52 (left) and corresponding interpretation (right) of unconformity-bounded packages. Thick red lines are major basement-involved faults, and thin red lines are faults that do not involve basement. Thicker black lines are high-amplitude events that are likely igneous intrusions. Vertical axis is in two-way travel time (TWTT). Line drawings of seismic profiles are displayed at approximately 1:1, assuming an average velocity of 3.5 km/s.

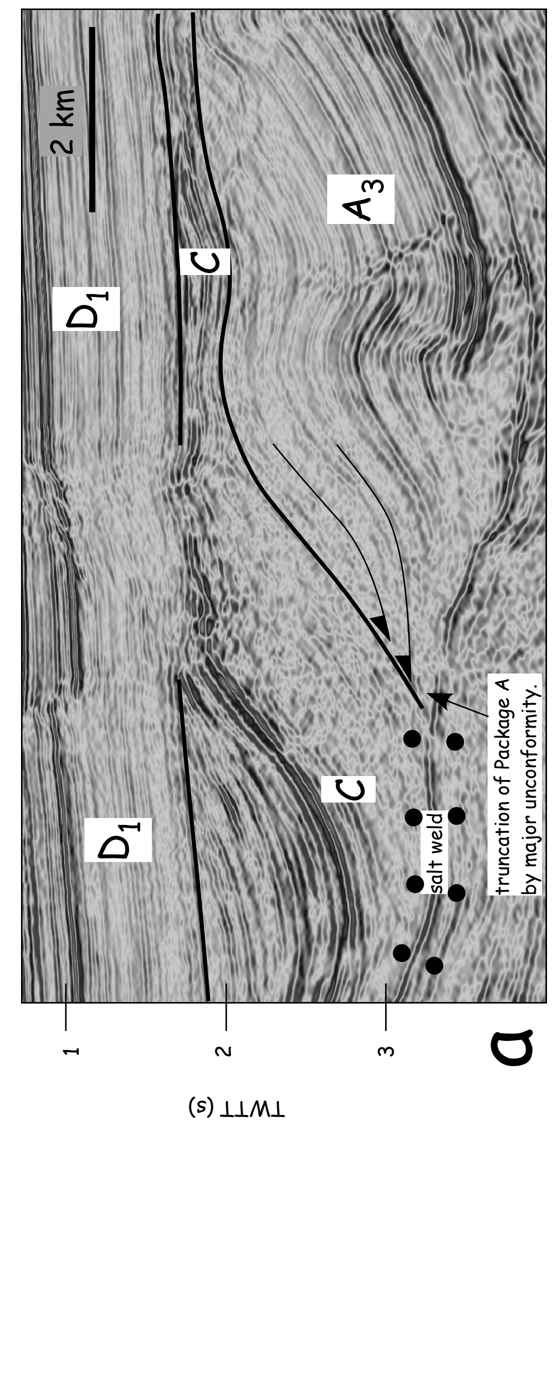

a
TWTT (s)
1
2
3
2 km
D1
C
A3
salt weld
truncation of Package A
by major unconformity.

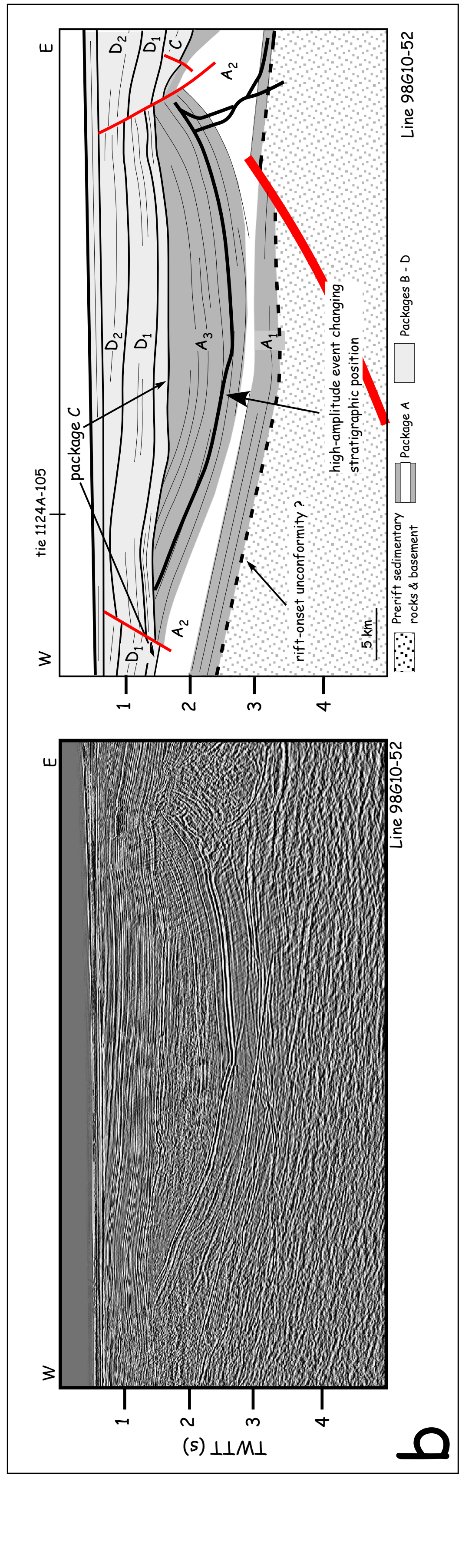

b
TWTT (s)
1
2
3
4
W
E
Line 98G10-52
tie 1124A-105
package C
D2
D1
C
A2
A3
A1
rift-onset unconformity ?
high-amplitude event changing
stratigraphic position
5 km
Prerift sedimentary
rocks & basement
Package A
Packages B - D

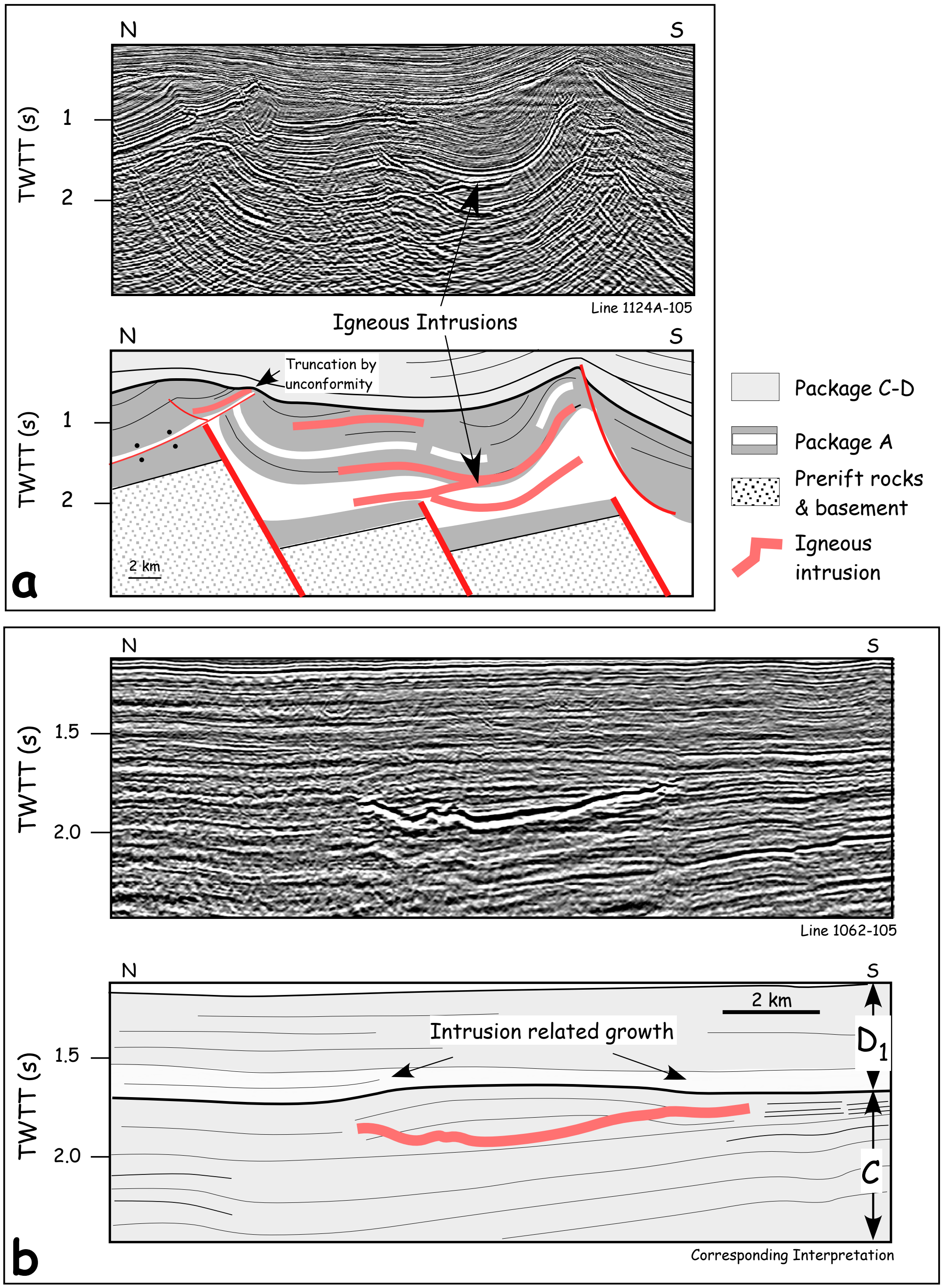

Figure 3.8. Summary figure highlighting evidence of igneous activity during and after rifting. Aptian-aged igneous activity is beyond the scope of this work. (a) Synrift igneous activity in central segment of Orpheus basin (line 1124A-105), (b) Postrift igneous activity in western segment of Orpheus basin (line 1062-105). See Figure 3.4 for line locations.

Figure 3.9. Correlation of interpreted seismic-stratigraphic units (A through D) with regional stratigraphy. Major unconformities: BU = Breakup Unconformity, JmU = Middle Jurassic Unconformity, AU = Avalon unconformity, K/T = Cretaceous-Tertiary unconformity, OU? = Oligocene unconformity. Pink lines in earliest Jurassic and Cretaceous strata indicate igneous rocks. (Modified after Wade and MacLean, 1990; MacLean and Wade, 1992; dates of igneous rocks from Jansa and Pe-Piper, 1985, 1988; Pe-Piper et al, 1992, 1994, 2007; Olsen et al., 1989)

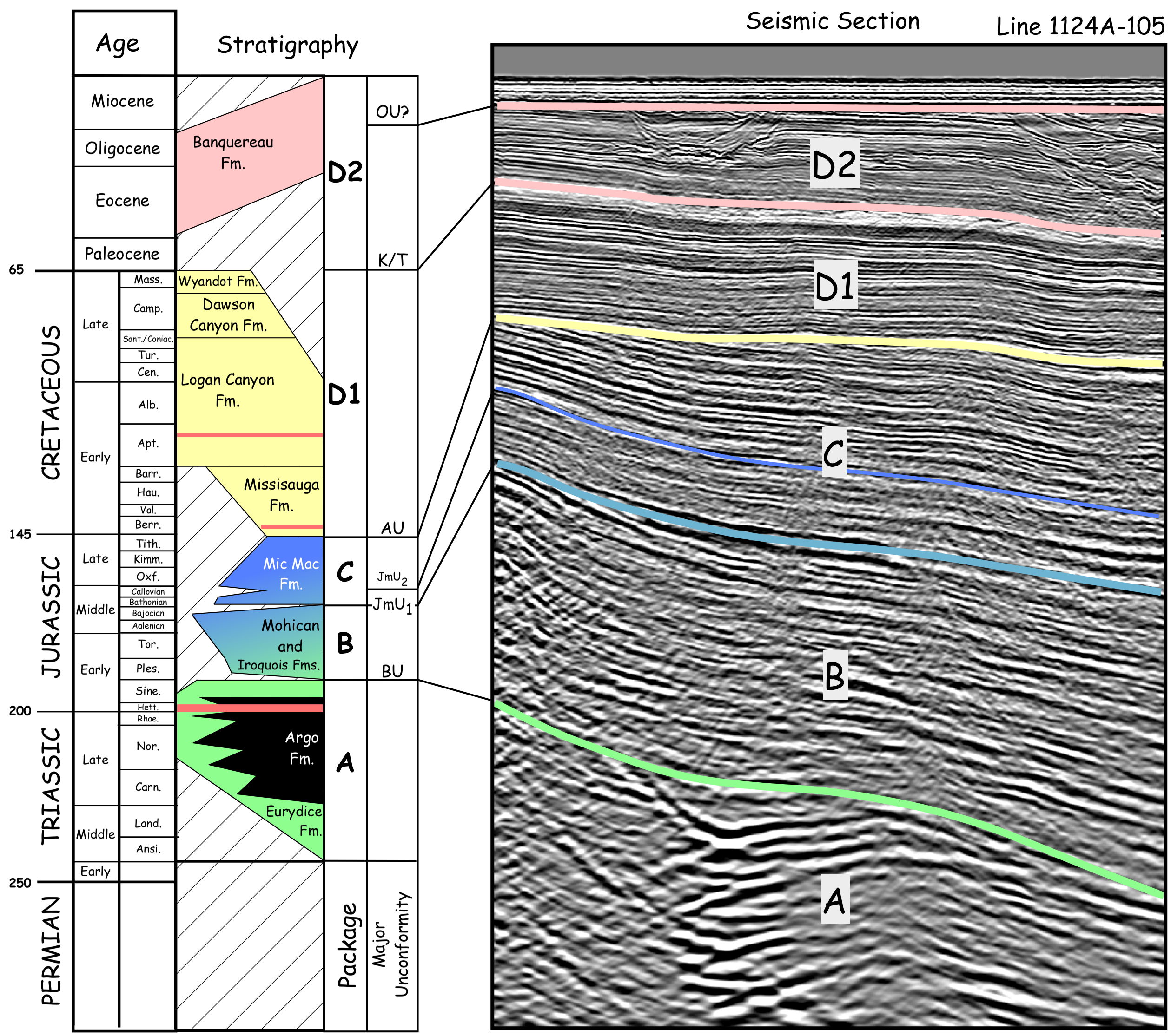

Age
Stratigraphy
Seismic Section
Line 1124A-105
Miocene
Oligocene
Eocene
Paleocene
CRETACEOUS
JURASSIC
TRIASSIC
PERMIAN
65
145
200
250
Late
Early
Middle
Mass.
Camp.
Sant./Coniac.
Tur.
Cen.
Alb.
Apt.
Barr.
Hau.
Val.
Berr.
Tith.
Kimm.
Oxf.
Callovian
Bathonian
Bajocian
Aalenian
Tor.
Ples.
Sine.
Hett.
Rhae.
Nor.
Carn.
Land.
Ansi.
Banquereau Fm.
Wyandot Fm.
Dawson Canyon Fm.
Logan Canyon Fm.
Missisauga Fm.
Mic Mac Fm.
Mohican and Iroquois Fms.
Argo Fm.
Eurydice Fm.
D2
D1
C
B
A
Package
OU?
K/T
AU
JmU2
JmU1
BU
Major Unconformity

Figure 3.10. Seismic line 1124A-105 (top) and corresponding detailed interpretation (bottom); Argo Salt colored black (see Fig. 3.4 for location). Line drawings of seismic profiles are displayed at approximately 1:1, assuming an average velocity of 3.5 km/s.

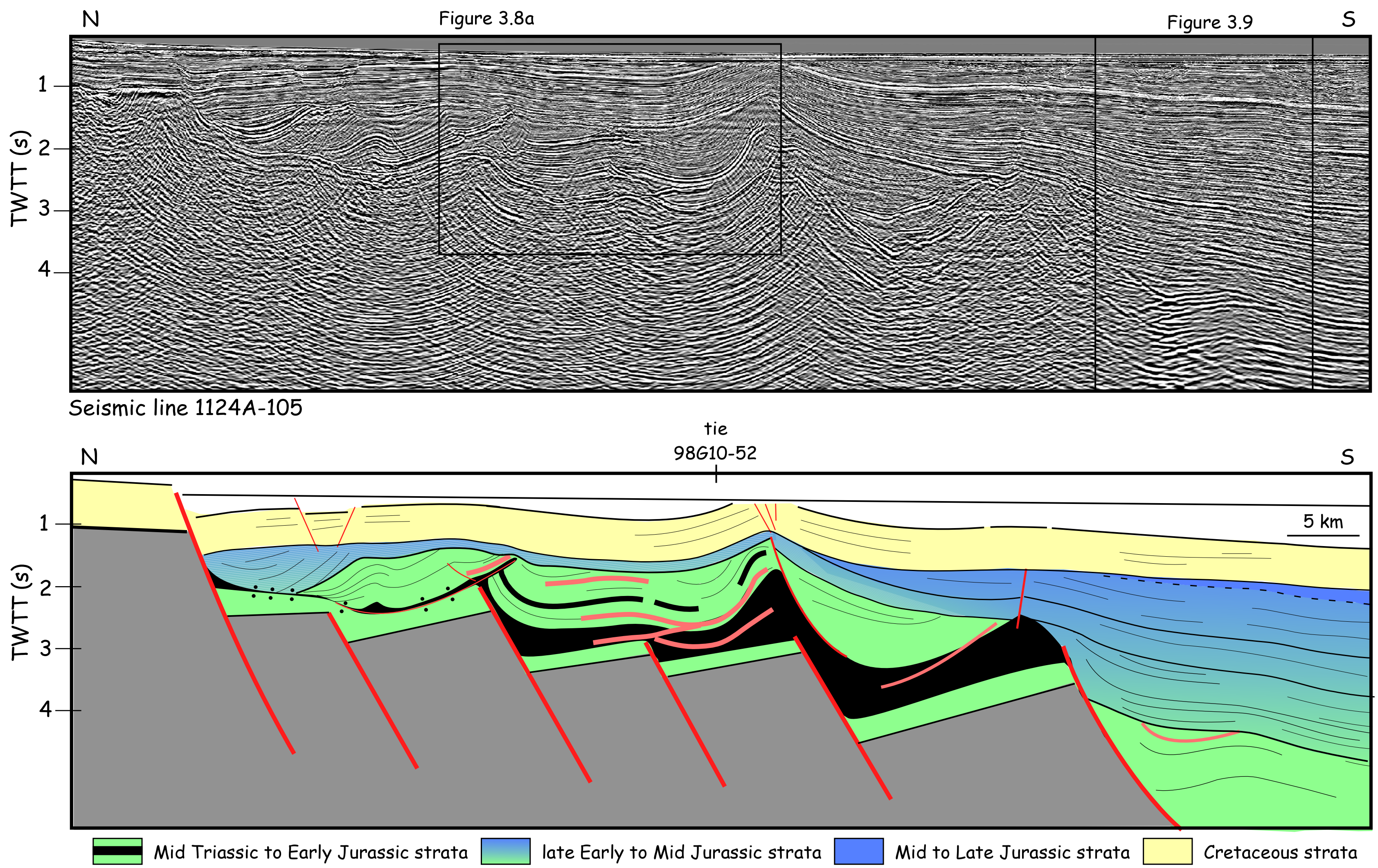
N
Figure 3.8a
Figure 3.9
S
TWTT (s)
1
2
3
4
Seismic line 1124A-105
tie
98G10-52
N
S
5 km
TWTT (s)
1
2
3
4
Mid Triassic to Early Jurassic strata
late Early to Mid Jurassic strata
Mid to Late Jurassic strata
Cretaceous strata

Figure 3.11. Seismic Line 98G10-52 (top) and corresponding detailed interpretation (bottom); Argo Salt colored black (see Fig. 3.4 for location). Line drawings of seismic profiles are displayed at approximately 1:1, assuming an average velocity of 3.5 km/s.

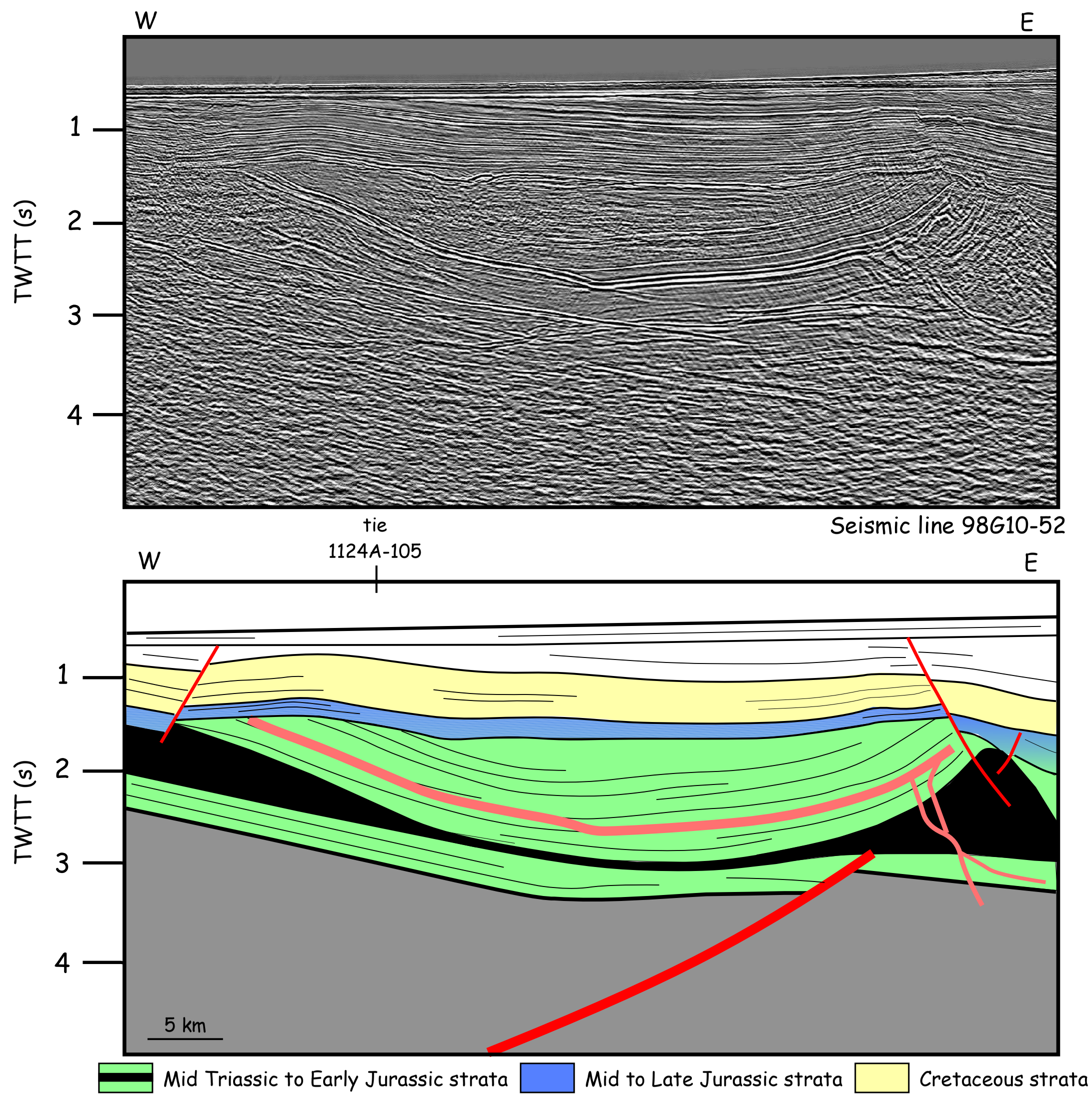
W
E
1
2
3
4
TWTT (s)
Seismic line 98G10-52
tie
1124A-105
W
E
1
2
3
4
TWTT (s)
5 km
Mid Triassic to Early Jurassic strata
Mid to Late Jurassic strata
Cretaceous strata

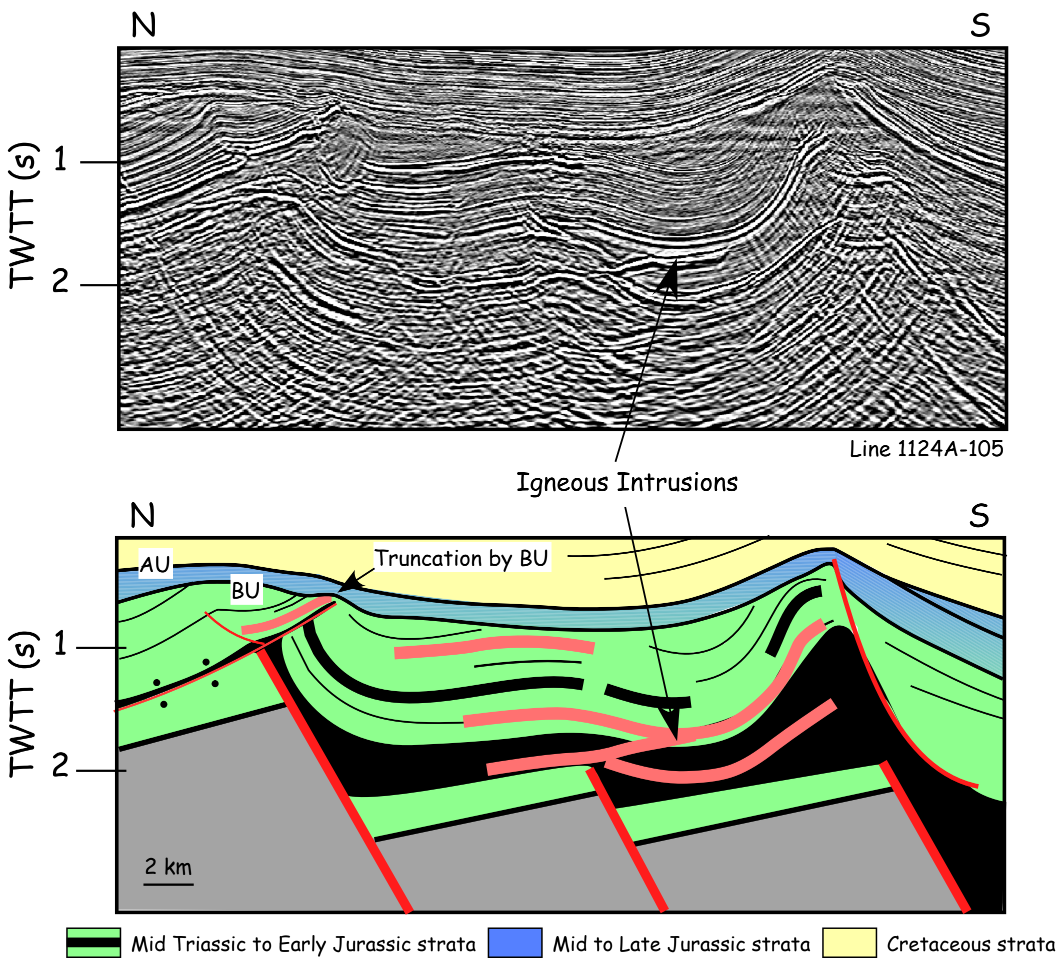

Figure 3.12. Close up of seismic line 1124A-105 (top) and corresponding detailed interpretation highlighting Early Jurassic igneous intrusions (bottom; see Fig. 3.9 for location). Note truncation of intrusions by the BU. Line drawings of seismic profiles are displayed at approximately 1:1, assuming an average velocity of 3.5 km/s.

Figure 3.13. Portion of seismic line 1062-105 (top) and corresponding detailed interpretation (bottom) highlighting Cretaceous igneous intrusion into Late Jurassic strata (Package C). Note darker yellow package (bottom of D1) above AU thins above intrusion. See Fig. 3.4 for location. Line drawings of seismic profiles are displayed at approximately 1:1, assuming an average velocity of 3.5 km/s.

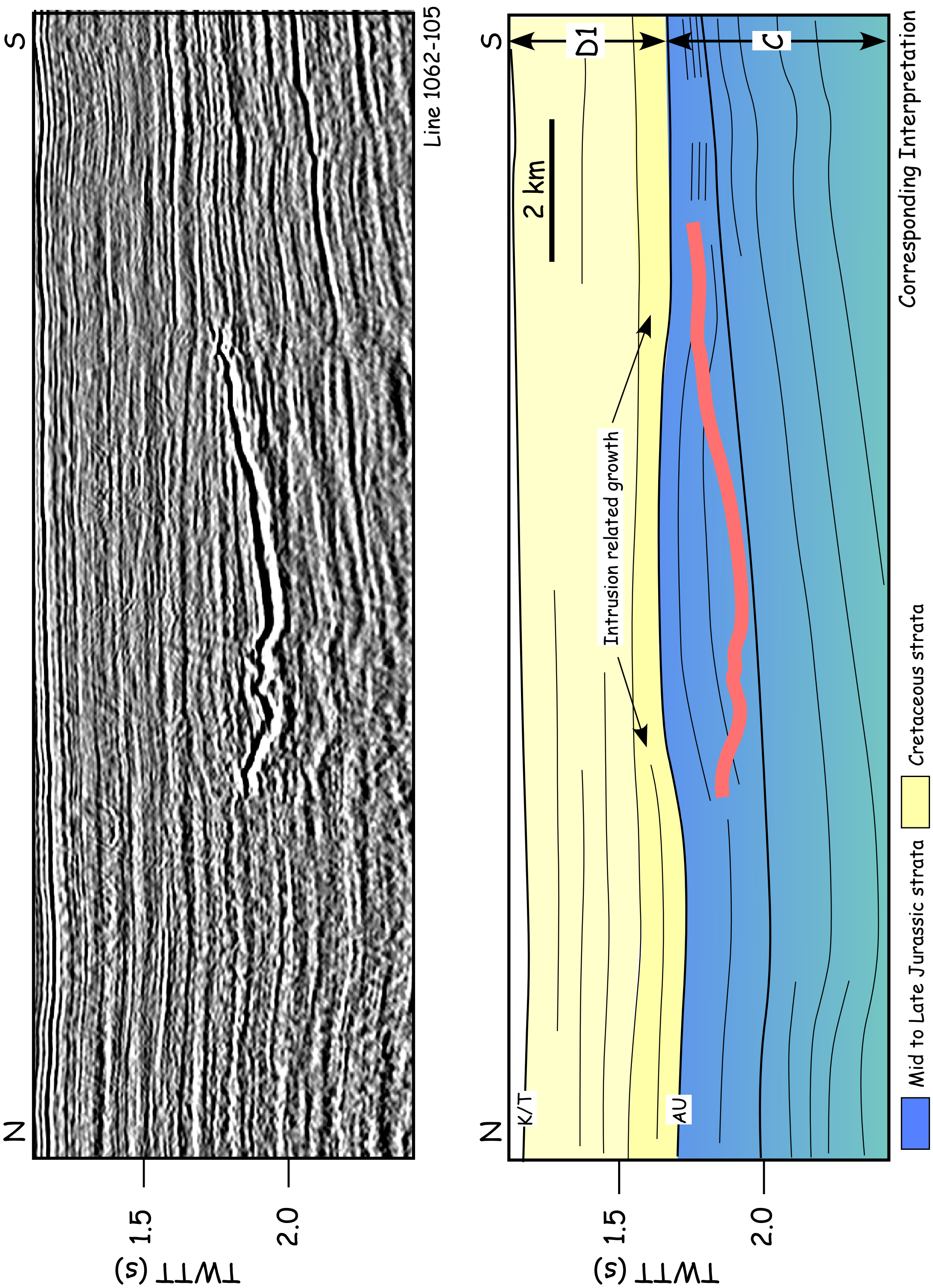
S
N
Line 1062-105
TWTT (s)
1.5
2.0
S
N
D1
C
2 km
Intrusion related growth
K/T
AU
TWTT (s)
1.5
2.0
Corresponding Interpretation
Mid to Late Jurassic strata
Cretaceous strata

Figure 3.14. Schematic restoration of northern portion of seismic line 1124A-105 from early Middle Triassic to present. (A-D) denotes rifting phase, (E-I) denotes "passive-margin" phase. See text for detailed explanation of figure.

Rifting Phase

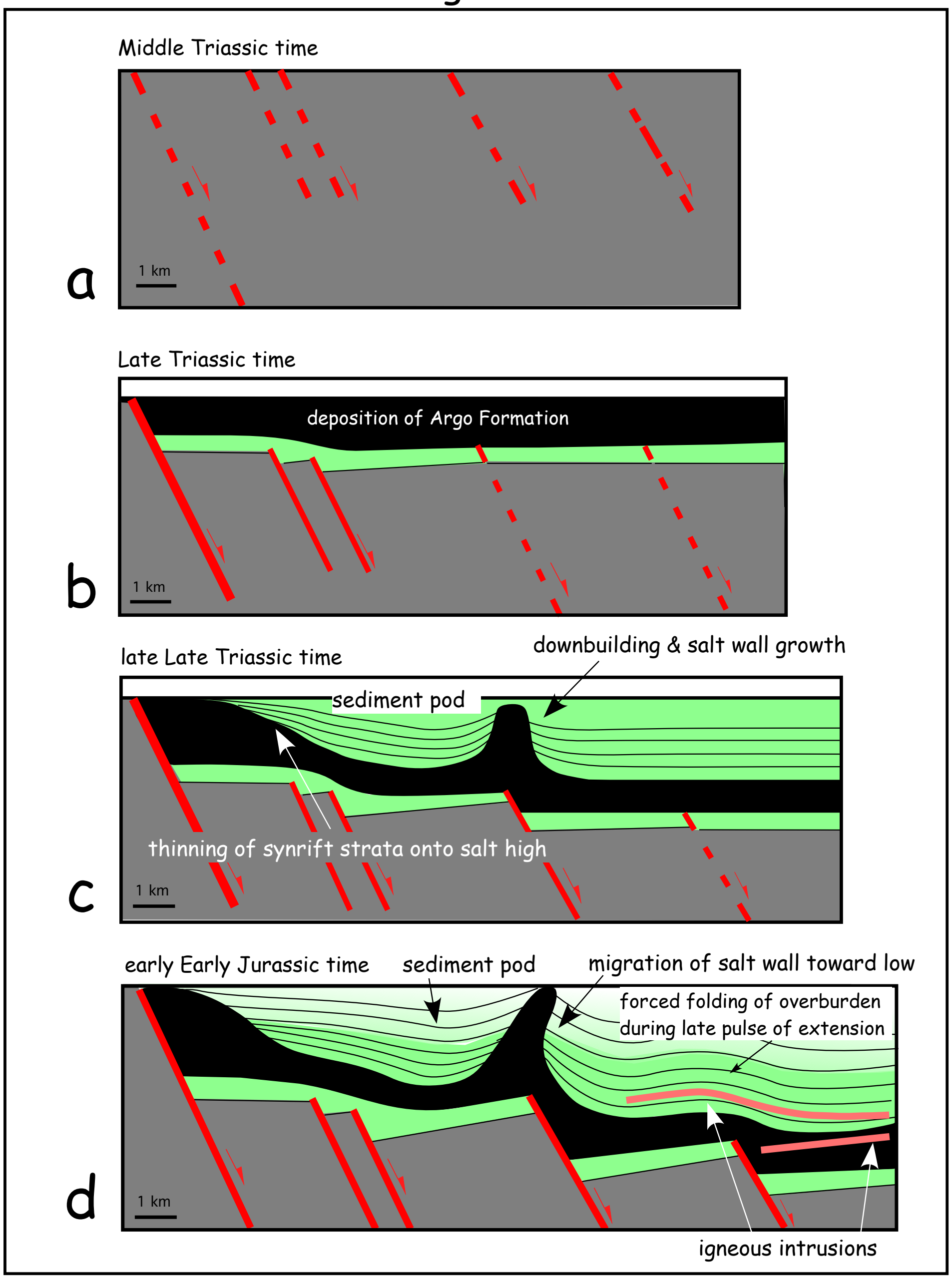

"Passive-Margin" Phase

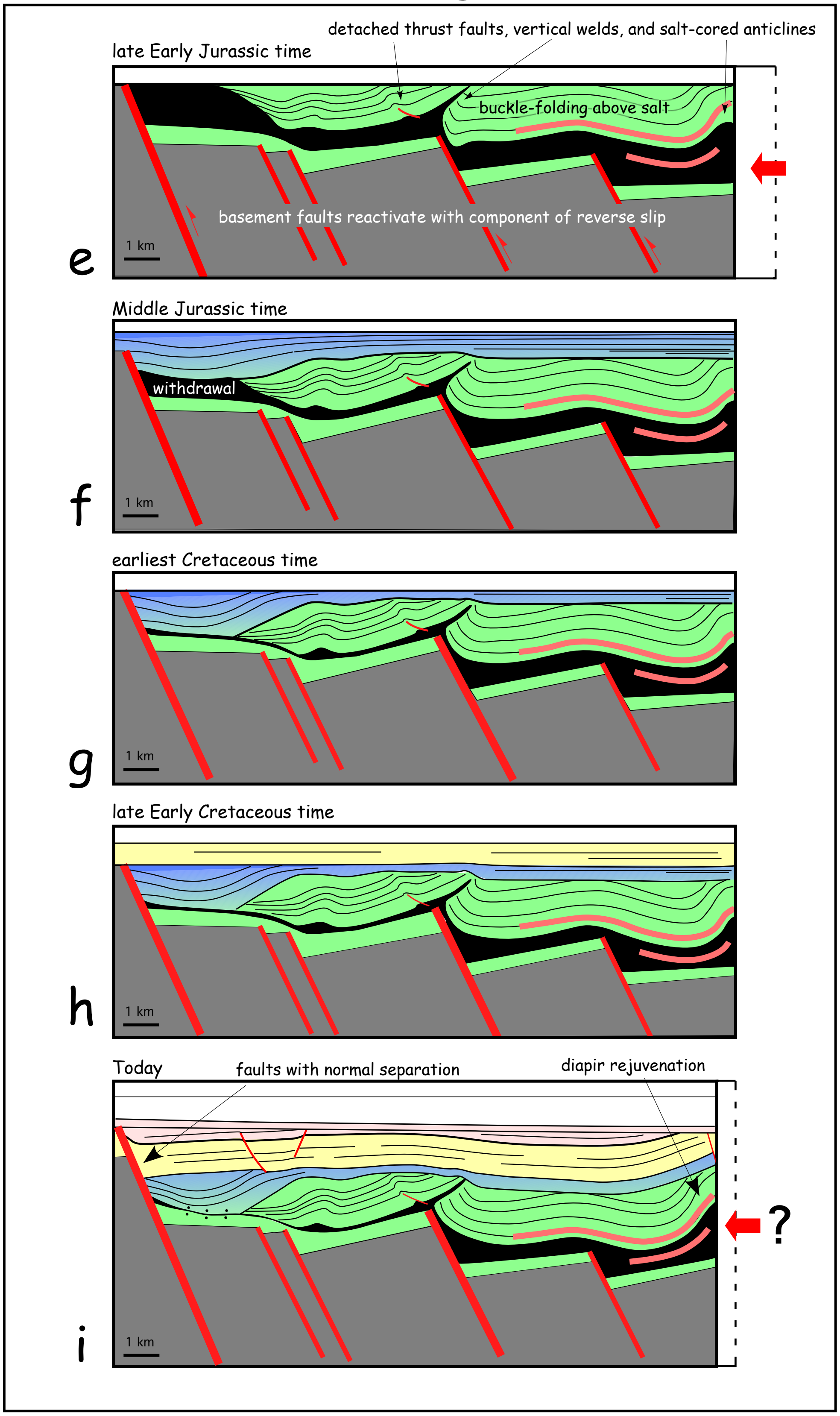

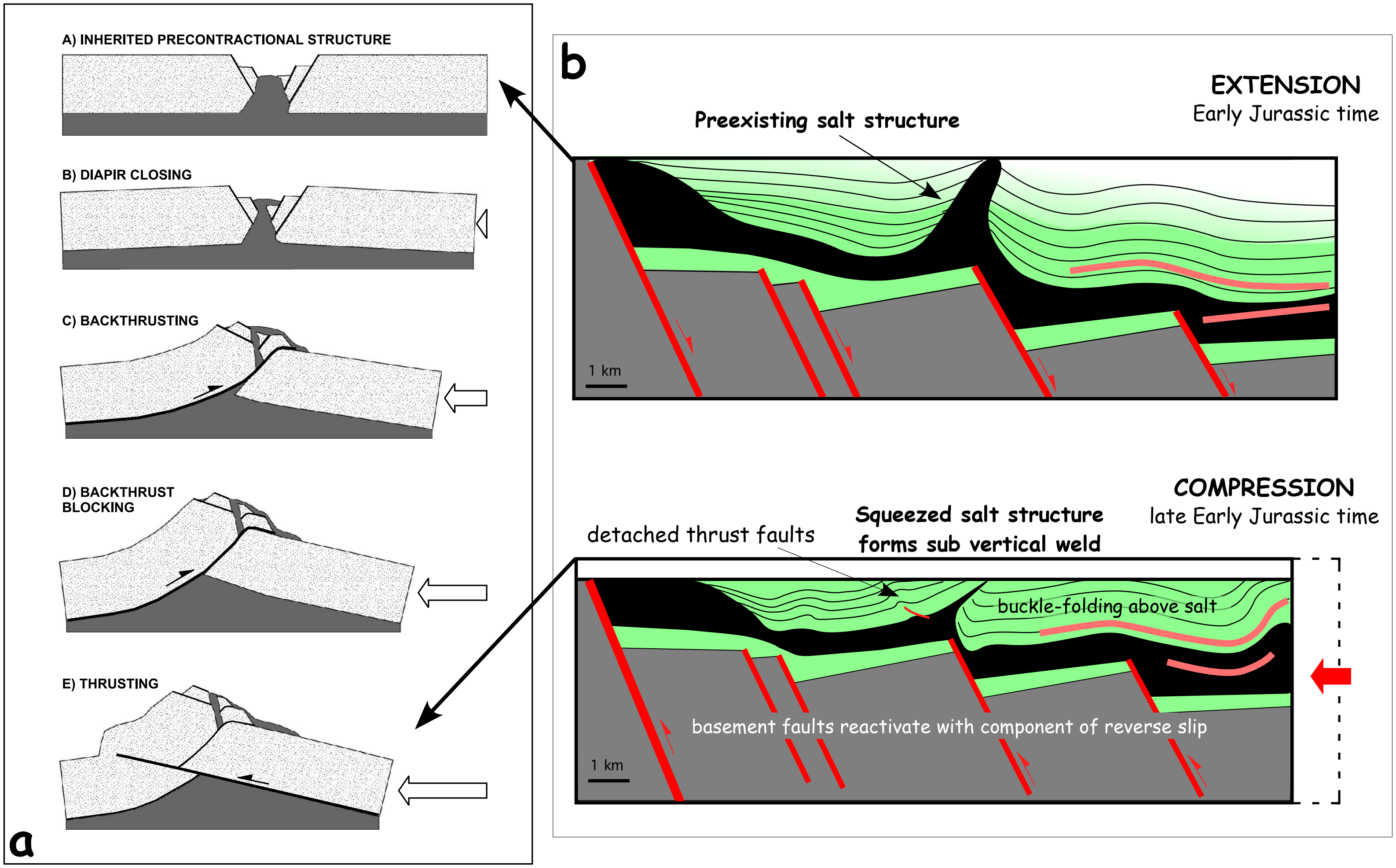

Figure 3.15. a) Schematic cartoon showing evolution of a preexisting salt structure that is subsequently shortened (from Roca et al., 2006). b) Schematic restoration of Line 1124A-105; (above) at the end of rifting, (below) after first shortening phase

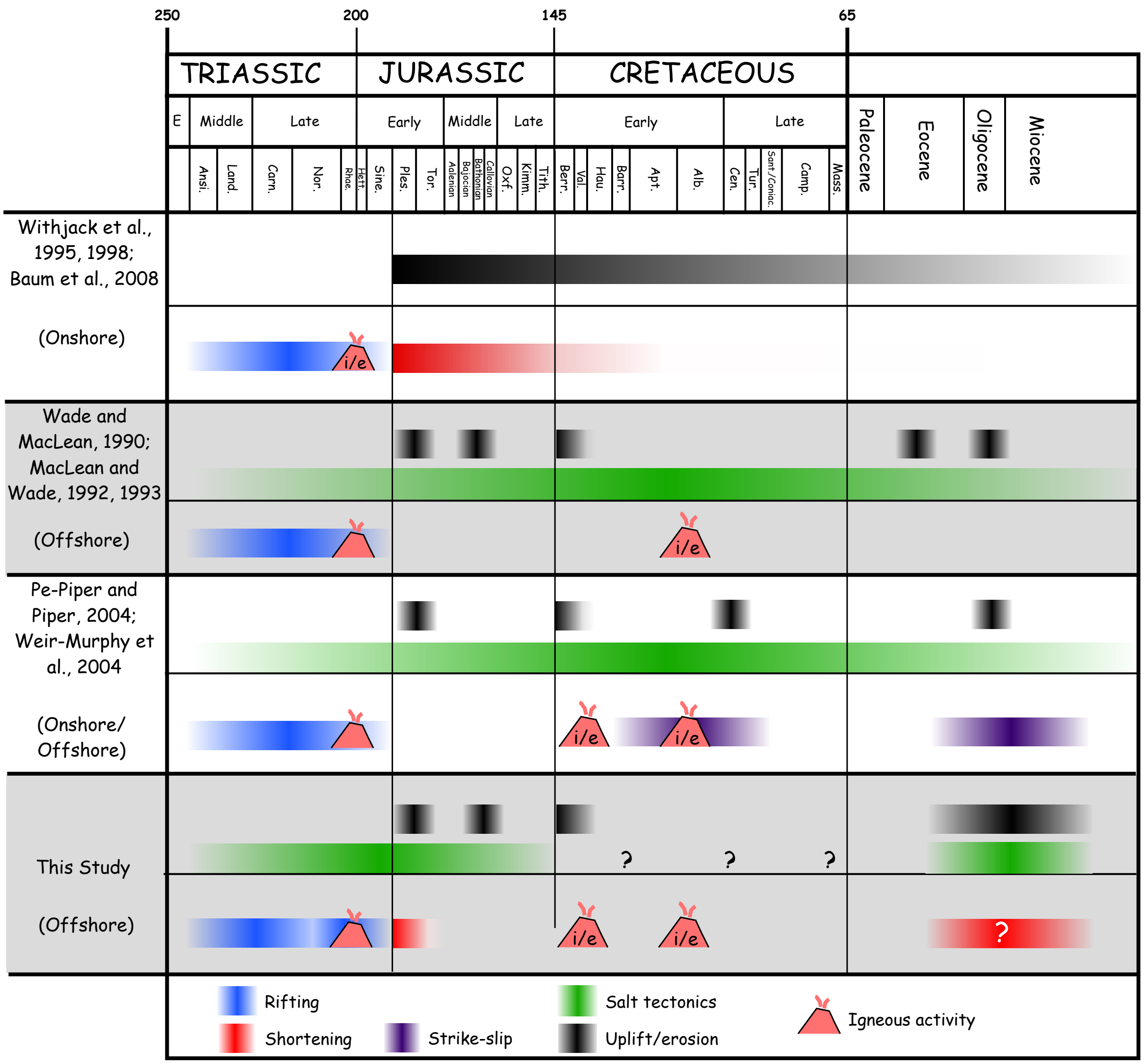

Figure 3.16. Graphical table highlighting differences regarding the development of the Orpheus and northern Scotian basins. On igneous activity symbol, i/e = intrusive/extrusive

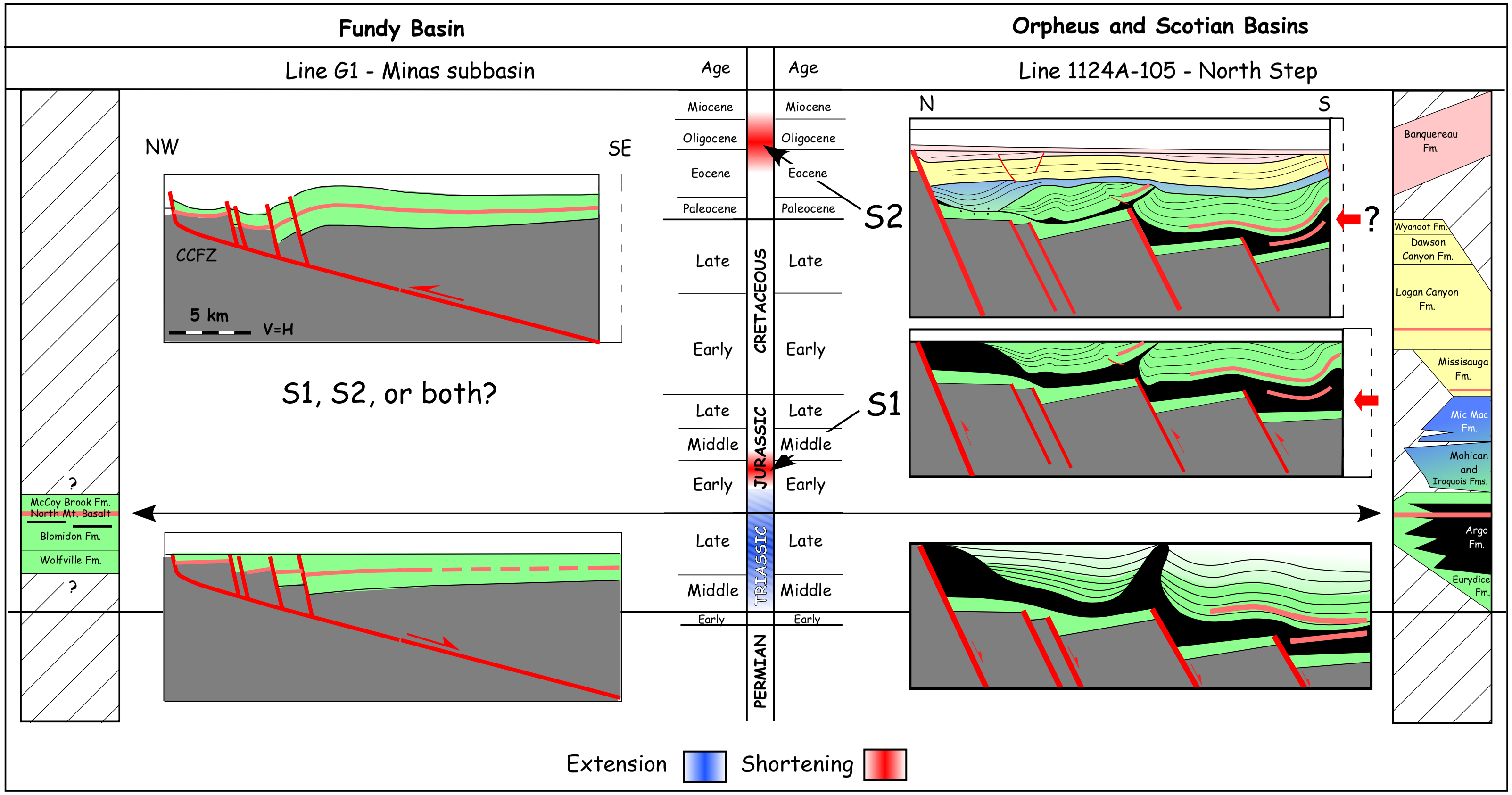

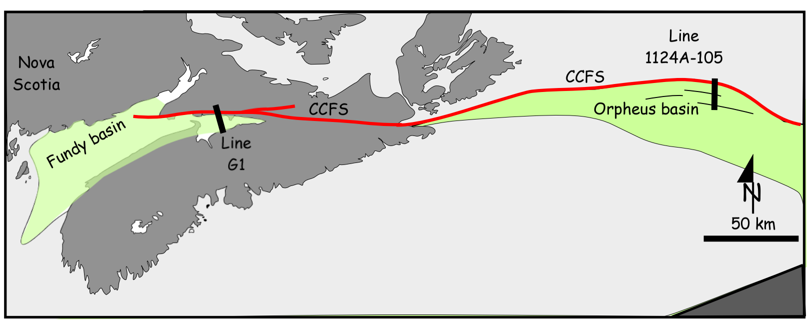

Figure 3.17. top. *Cross sections based on seismic data from the Fundy basin (left) and Orpheus and Scotian basins (right). S1 indicates Early Jurassic shortening, S2 indicates Cenozoic shortening. See text for discussion. Seismic line G1 after Baum et al., 2008.* **bottom.** *Map of onshore and offshore Nova Scotia. Thick black lines indicate locations of seismic lines. Red lines are Cobequid-Chedabucto Fault System (CCFS).*